nature cancer

Article

https://doi.org/10.1038/s43018-023-00513-2

A palmitate-rich metastatic niche enables metastasis growth via p65 acetylation resulting in pro-metastatic NF-κB signaling

Received: 6 February 2022

Accepted: 3 January 2023

Published online: 2 February 2023

Check for updates

A list of authors and their affiliations appears at the end of the paper

Metabolic rewiring is often considered an adaptive pressure limiting metastasis formation; however, some nutrients available at distant organs may inherently promote metastatic growth. We find that the lung and liver are lipid-rich environments. Moreover, we observe that pre-metastatic niche formation increases palmitate availability only in the lung, whereas a high-fat diet increases it in both organs. In line with this, targeting palmitate processing inhibits breast cancer-derived lung metastasis formation. Mechanistically, breast cancer cells use palmitate to synthesize acetyl-CoA in a carnitine palmitoyltransferase 1a-dependent manner. Concomitantly, lysine acetyltransferase 2a expression is promoted by palmitate, linking the available acetyl-CoA to the acetylation of the nuclear factor-kappaB subunit p65. Deletion of lysine acetyltransferase 2a or carnitine palmitoyltransferase 1a reduces metastasis formation in lean and high-fat diet mice, and lung and liver metastases from patients with breast cancer show coexpression of both proteins. In conclusion, palmitate-rich environments foster metastases growth by increasing p65 acetylation, resulting in a pro-metastatic nuclear factor-kappaB signaling.

Nutrient availability is a key aspect of a permissive environment enabling metastasis formation. Certain nutrients such as glucose, fatty acids, pyruvate and glutamine are aiding metastasizing cancer cells when they are seeding and colonizing in a distant organ[1]. While nutrient availability is certainly defined by the functional processes occurring in healthy organs, the question arises whether aberrant disease processes or dietary conditions influence the nutrient concentrations in the organs of metastasis.

A nutrient class highly linked to metastasis formation is fatty acids[2]. In many cancer types, blocking fatty acid uptake is sufficient to impair metastasis formation[3,4], whereas increased dietary fat intake promotes cancer progression[1,2]; however, it remains largely elusive whether these fatty acids are available in future organs of metastasis and whether high-fat diet (HFD) feeding alters their concentration.

Another aberrant disease process linked to cancer progression is pre-metastatic niche formation[5]. There is extensive evidence that the immune cell and extracellular matrix composition of the pre-metastatic niche are modulated by tumor-secreted factors resulting in increased metastasis formation in such primed organs[5,6]. However, to date very little is known about nutrient priming of the pre-metastatic niche with only one report showing increased glucose availability resulting from a general hypometabolism of lung-resident cells[7].

We found that the interstitial fluid of the lungs and livers is palmitate-rich and that a high-fat diet and pre-metastatic niche formation further increase palmitate concentrations in an organ-specific or general manner. We further show that breast cancer cells rely on CPT1a for fatty acid oxidation, which in turn activates nuclear factor kappaB (NF-κB) signaling via KAT2a-dependent p65 acetylation. Accordingly, CPT1a and KAT2a targeting is highly effective in inhibiting metastasis formation.

Results

The lung and liver are lipid-rich environments

Although the lung and liver are frequent metastatic sites, nutrient concentrations in these organs remain largely unknown. We isolated

e-mail: sarah-maria.fendt@kuleuven.be

the lung and liver interstitial fluid, which is a local source of nutrients for metastasized cancer cells, from BALB/c mice and non-cancerous lung tissue of patients (Supplementary Table 1)[8,9] and measured fatty acid availability using mass spectrometry. Mouse and human lung interstitial fluids were very similar regarding fatty acid composition and concentrations (Fig. 1a). Palmitate and oleate were high in both organs, whereas linoleate and stearate were highly available in the lung and liver, respectively (Fig. 1a,b). Most of these fatty acids were present as acyl side chains within lipids (referred as fatty acids) rather than their free form (Extended Data Fig. 1a). Thus, we concluded that the lung and the liver are organs rich in palmitate- and oleate-containing lipids.

High-fat diet increases general fatty acid availability

To date, it is largely unknown whether HFD exposure alters nutrient concentrations in organ interstitial fluids. Thus, we investigated fatty acid concentrations in intestinal fluids and metastasis formation in BALB/c mice fed a HFD or a control diet (CD) for 16 weeks (Extended Data Fig. 1b). We found that HFD feeding increased the levels of palmitate, oleate and stearate in the lung and liver interstitial fluids (Fig. 1c and Extended Data Fig. 1c,d). Next, we asked whether this elevation in fatty acid availability coincided with an increase in metastasis formation. For lung and liver metastasis, we intravenously (i.v.) or intrasplenically (i.sp.) injected 4T1 cells expressing the congenic marker CD90.1 and measured the percentage of cancer cells in the lung after 12 days (d) or metastatic area in the liver after 17 d. We found that HFD feeding increased lung and liver metastatic growth by more than twofold and threefold, respectively (Fig. 1d,e). Then, we asked whether HFD feeding was also sufficient to increase the metastatic growth of 4T07 cells, which are known to disseminate to the lung but do not outgrow[10]. Remarkably, we observed that 4T07 cells were more proficient to colonize the lung environment in mice that received HFD compared to mice on CD (Fig. 1f). Thus, we concluded that HFD exposure increased fatty acid availability in the lung and liver and that highly and low metastatic cancer cells benefit from an organ environment primed by HFD.

Pre-metastatic lungs are enriched in palmitate

Next, we investigated whether pre-metastatic niche formation induced by tumor-secreted factors[6] results in fatty acid priming. We generated tumor-conditioned medium (TCM) by culturing 4T1 primary breast tumors in Dulbecco's modified Eagle medium (DMEM) without fetal bovine serum (FBS)[11–14] and i.v. injected TCM or control medium (CM) for 3 weeks into BALB/c mice[13,14] (Extended Data Fig. 1e). We confirmed that TCM injections induced an experimental pre-metastatic niche in the lung (Extended Data Fig. 1f–h) and boosted lung metastasis formation (Fig. 1g). Likewise, 4T07 cells injected into mice that had received 4T1 tumor-derived TCM resulted in a 6.8-fold increase in metastasis formation (Fig. 1g). Consecutively, we isolated lung and liver interstitial fluid from mice treated with TCM or CM and measured fatty acid concentrations. We discovered that upon experimental pre-metastatic niche formation palmitate, but not oleate or linoleate abundance increased in the lung interstitial fluid. On the contrary, fatty acid abundance in the liver interstitial fluid was not significantly changed (Fig. 1h and Extended Data Fig. 1i). To verify this finding, we injected 4T1 cancer cells into the mammary fat pad of mice and isolated lung and liver interstitial fluid before detectable spontaneous metastases arose (17 d). We found that spontaneous pre-metastatic niche formation also resulted in the same fatty acid changes as TCM injection (Fig. 1i and Extended Data Fig. 1j). Next, we analyzed lung interstitial fluid collected from patients with breast cancer and control patients without cancer (Supplementary Tables 1 and 2). In line with our mouse data, we found that patients with breast cancer but without detected lung metastases showed increased palmitate but not oleate concentration in their lung interstitial fluid compared to control patients without cancer (Fig. 1j). Thus, we concluded that palmitate concentrations increase in the lung during pre-metastatic niche formation.

AT2 cells secrete palmitate lipids to pre-metastatic lungs

Next, we hypothesized that some lung-resident cells respond to tumor-secreted factors by releasing palmitate to the pre-metastatic niche. To identify these cells, we performed single-cell RNA sequencing (scRNA-seq) on lungs of BALB/c mice that were injected with TCM or CM. Cell-type annotation combined with the analysis of lipid-related genes highlighted alveolar type II (AT2) as the potential cell type increasing lipid release in response to TCM (Fig. 2a and Extended Data Fig. 2a). AT2-resident cells are known to naturally release palmitic acyl chain-containing lipids that form 90% of the pulmonary surfactant in healthy lungs[15]. Accordingly, we observed that the expression of lipid production and pulmonary surfactant release genes was upregulated in AT2 cells in mice exposed to TCM (Fig. 2a). The expression of the same genes remained unchanged in alveolar type I (AT1) epithelial cells (Fig. 2a). Similarly, AT2 cells that were freshly isolated from mice undergoing spontaneous pre-metastatic niche formation due to 4T1 primary breast tumors showed significantly elevated expression of the same lipid production and pulmonary surfactant release genes (Fig. 2b). Notably, expression of these genes (except for *Acsl4*) was not significantly altered in the presence of a low metastatic 4T07 primary breast tumor (Fig. 2c).

We next investigated whether AT2 cells directly respond to TCM and potentially elevate palmitate secretion. We isolated AT2 cells from *Sftpc-CreERT2;R26R-YFP* mice, cultured them on a three-dimensional (3D)-scaffold system[16] and treated them with CM or TCM generated from 4T1 primary tumors. We observed that AT2 cells increased the expression of several genes, identified by our in vivo scRNA-seq, after in vitro TCM exposure (Fig. 2d). Moreover, we observed an elevated secretion of palmitate, but not oleate, from AT2 cells treated with TCM (Fig. 2e). Thus, we concluded that lung-resident AT2 cells respond to secreted factors from highly metastatic breast tumors by increasing the expression of lipid production and pulmonary surfactant release genes, which is associated with increased palmitate release.

High-fat diet increases the fraction of AT2 cells

As HFD increased palmitate availability in the lungs, we examined whether AT2 cells were also involved in this effect. Therefore, we performed scRNA-seq of lungs from mice fed a HFD versus CD. In the lungs of HFD mice, we observed a slight to moderate upregulation of lipid release and pulmonary surfactant genes in AT2 cells (Extended Data Fig. 2b). However, the most striking observation was an increase in the total fraction of AT2 cells in HFD compared to CD mice (Extended Data Fig. 2c), which is consistent with a previous report[17]. Thus, we concluded that the mechanisms by which HFD and tumor-secreted factors alter lipid availability in future organs of metastasis differ but that, at least in the lung, AT2 cells may be involved in both processes.

Palmitate increases in metastases and promotes spheroid growth

Next, we asked whether the priming of palmitate in pre-metastatic lungs is reflected in metastases. Spatial mass spectrometry imaging showed that 4T1 lung metastases were enriched in palmitate-containing lipids compared to adjacent non-cancerous tissue (Fig. 3a). Moreover, palmitate, but not oleate or linoleate abundance increased in 4T1 and EMT6.5 lung metastases compared to primary tumor tissues (Fig. 3b). We hypothesized that this enrichment in palmitate was linked to lipid species secreted by AT2 cells. A lipidomics analysis of lung metastases compared to primary tumors showed an enrichment in lpalmitic acyl chains of several phospholipids (PLs) such as phosphatidylcholine (PC), phosphatidylglycerol (PG) and phosphatidylethanolamine (PE), which are species of the pulmonary surfactant[15] (Extended Data Fig. 3a). Thus, these data suggest that breast cancer-derived lung metastases take up palmitate-containing lipids released by AT2 cells.

Using a tumor spheroid assay[18,19] we next found that 3D-cultured breast cancer cells, like metastases, exhibited palmitate, but not oleate

https://doi.org/10.1038/s43018-023-00513-2

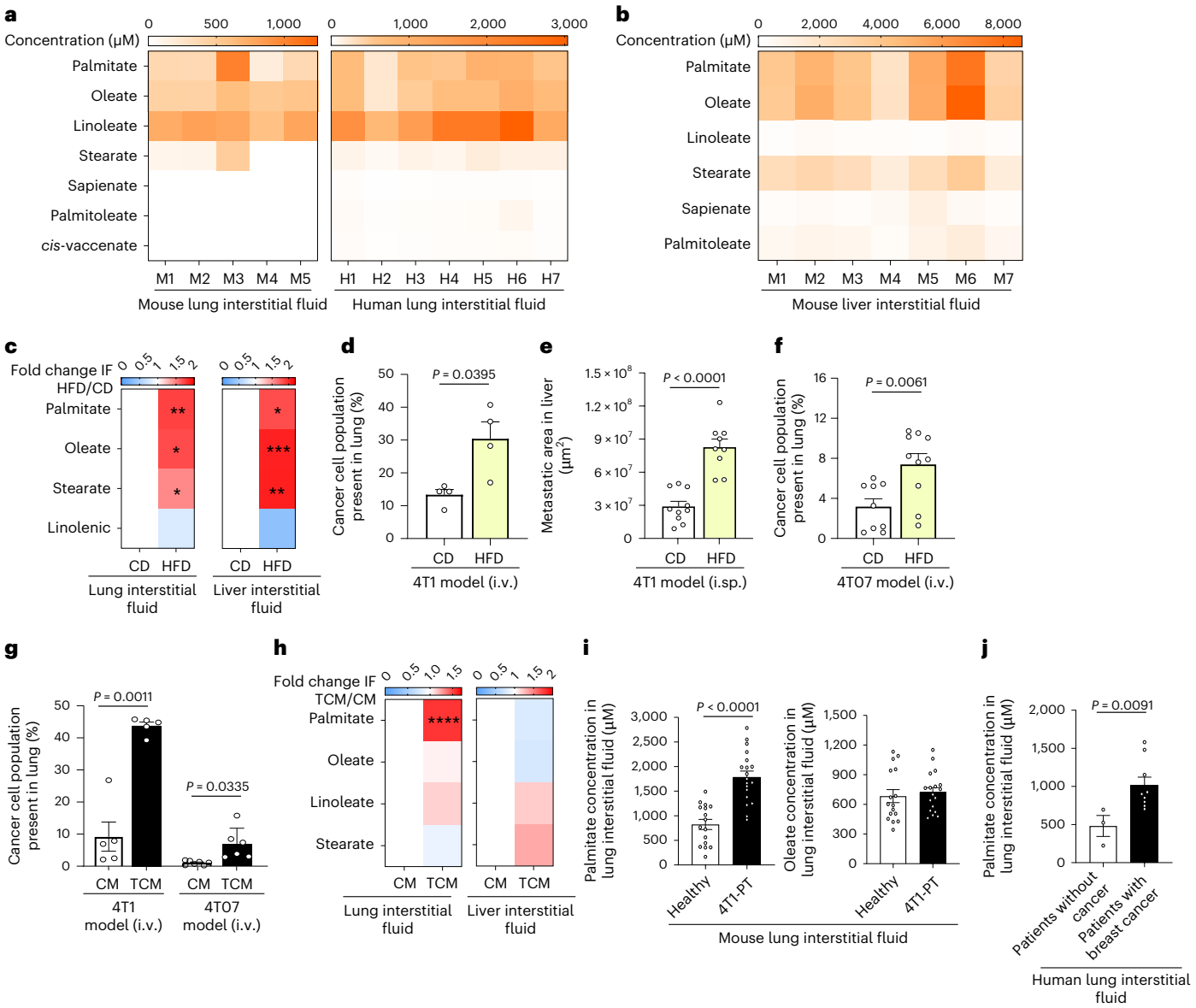

Fig. 1 | High-fat diet enhances overall fatty acid availability in the lung and liver, whereas palmitate availability is specifically increased in the lung during pre-metastatic niche formation. a, Total fatty acid concentrations in the lung interstitial fluid of healthy BALB/c mice ($n = 5$) and human non-cancer patients ($n = 7$) detected by mass spectrometry. **b**, Total fatty acid concentrations present in the liver interstitial fluid of healthy BALB/c mice ($n = 7$ mice) detected by mass spectrometry. **c**, Relatives changes in fatty acid concentrations in the lung and liver interstitial fluid of BALB/c mice after 16 weeks on CD or HFD ($n = 11$ lung, $n = 8$ liver). Unpaired two-tailed *t*-tests with Welch correction. Lung, $^{**}P = 0.01$, $^{*}P = 0.011$, $^{*}P = 0.035$; liver, $^{*}P = 0.0283$, $^{***}P = 0.0003$, $^{**}P = 0.018$. IF, interstitial fluid. **d**, Percentage of cancer cells present in the lung of CD- and HFD-fed mice i.v. injected with CD90.1-expressing 4T1 breast cancer cells. Data are presented as mean + s.e.m. ($n = 4$ mice). Unpaired two-tailed *t*-tests with Welch correction. **e**, Metastatic area in the liver of CD-fed ($n = 10$ mice) and HFD-fed ($n = 9$ mice) mice injected with 4T1 breast cancer cells i.sp. Data are presented as mean + s.e.m. Unpaired two-tailed *t*-tests with Welch correction. **f**, Percentage of cancer cells present in the lung of CD-fed ($n = 9$ mice) and HFD-fed ($n = 10$ mice) mice i.v. injected with CD90.1-expressing 4T07 breast cancer cells. Data are presented as mean + s.e.m. Unpaired two-tailed *t*-tests with Welch correction. **g**, Percentage of cancer cells present in the lung of mice injected with CM ($n = 5$ mice) or 4T1 TCM ($n = 6$ mice) (3 weeks, three times per week) after 16 d of i.v. injections with CD90.1-expressing 4T1 or 4T07 breast cancer cells. Data are presented as mean ± s.e.m. Unpaired two-tailed *t*-tests with Welch correction. **h**, Relative changes in fatty acid concentrations in the lung and liver interstitial fluid of BALB/c mice injected with CM or 4T1-TCM (CM, $n = 11$ and TCM, $n = 12$ in the lung; CM, $n = 9$ and TCM, $n = 10$ in the liver). Unpaired two-tailed *t*-tests with Welch correction. $^{****}P < 0.0001$. **i**, Palmitate (left) and oleate (right) concentration in the lung interstitial fluid of healthy ($n = 16$) or 4T1 tumor-bearing (PT) ($n = 18$) BALB/c mice. Data are presented as mean ± s.e.m. Unpaired two-tailed *t*-tests with Welch correction. **j**, Palmitate concentration in the lung interstitial fluid of patients without cancer (emphysema) ($n = 3$ patients) compared to patients with breast cancer without detected lung metastases ($n = 9$ patients). Data are presented as mean ± s.e.m. Unpaired two-tailed Mann–Whitney *U*-tests.

enrichment compared to the same breast cancer cells cultured in two-dimensions (2D) (Fig. 3c and Extended Data Fig. 3b). In line with this, 3D-cultured breast cancer cells displayed increased fatty acid uptake and reduced de novo synthesis compared to 2D-cultured cells (Extended Data Fig. 3c,d). Subsequently, we supplemented conjugated palmitate (75 μm) and (as a negative control) oleate (116 μm) to 3D-cultured breast cancer cells on top of 10% FBS, resulting in a similar final concentration of 130 μm per fatty acid and in a selective intracellular increase of each fatty acid within cancer cells (Extended Data Fig. 3e). Notably, the addition of extra palmitate, but not oleate,

https://doi.org/10.1038/s43018-023-00513-2

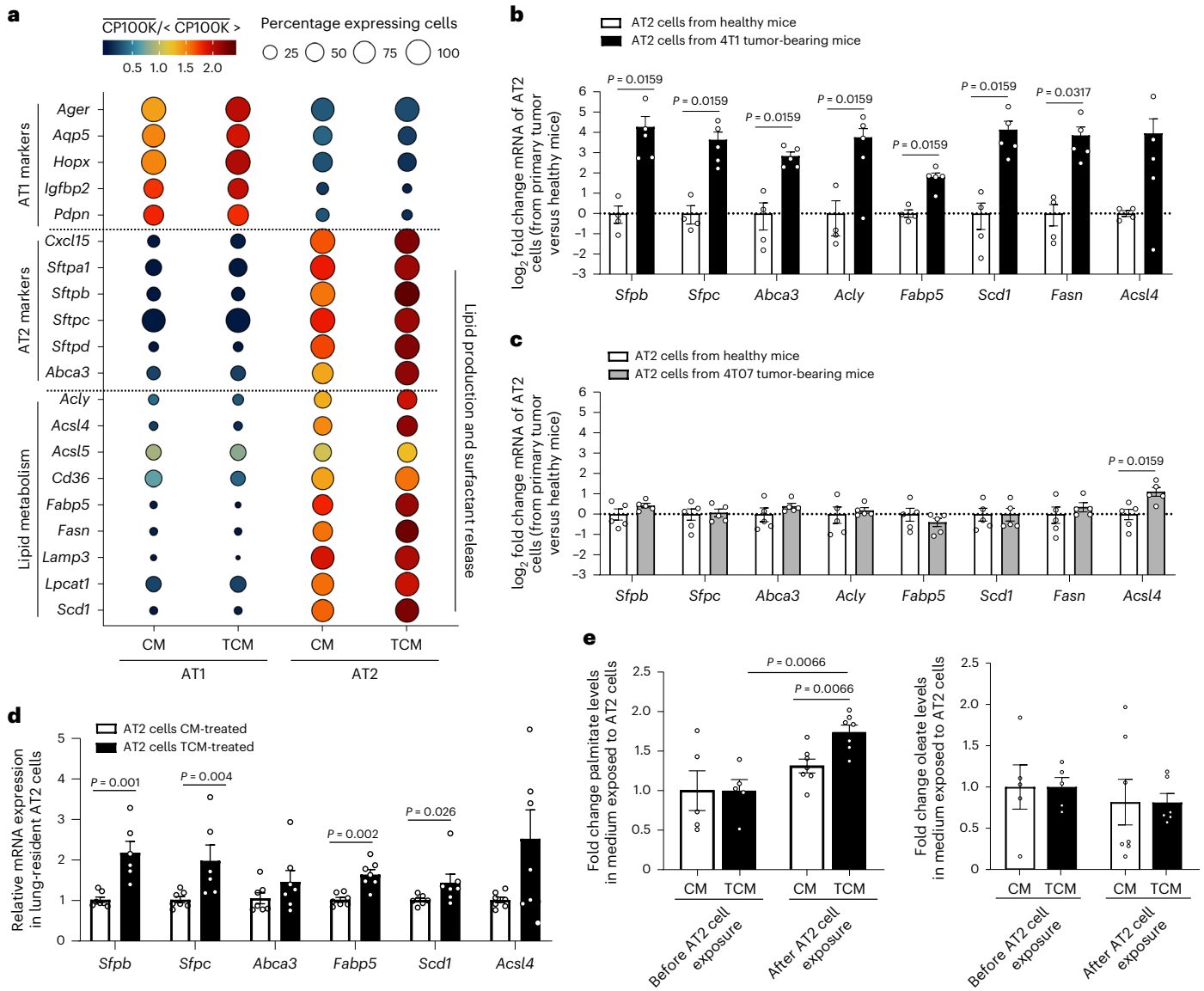

Fig. 2 | Lung-resident alveolar type II cells increase surfactant-related gene expression and palmitate release during pre-metastatic niche formation. **a**, scRNA-seq-based gene expression versus cell type and pre-conditioning medium profiles for known markers for AT1 and AT2 cells and lipid-related genes (left). Scaled expression levels are indicated by the color scale, where $\overline{CP100k}$ denotes the average gene expression level (in counts per 100,000 reads) over all cells of a given type in each condition and $\overline{\overline{CP100k}}$ indicates the average of the latter over all cell types and pre-conditioning medium conditions. The areas of the circles represent the percentage of cells with non-zero expression of each gene among all cells of each type and in each pre-conditioning medium condition. **b**,**c**, Relative expression of genes implicated in lipid and production surfactant release in AT2 cells isolated from healthy or 4T1 (**b**) and 4T07 (**c**) tumor-bearing (PT) BALB/c mice. Bars represent $\log_2$ of average fold change relative to AT2 in healthy mice and single dots represent individual fold changes. Error bars represent mean ± s.e.m. ($n = 5$ mice). Unpaired nonparametric two-tailed Mann–Whitney *U*-tests. **d**, Relative expression of genes involved in pulmonary surfactant production and secretion in AT2 cells exposed to CM or TCM for 72 h. Data are presented as mean ± s.e.m. ($n = 6$ biological replicates). Unpaired nonparametric two-tailed Mann–Whitney *U*-tests. **e**, Relative palmitate and oleate levels present in CM or TCM before and after exposure to lung-resident AT2 cells for 72 h. Data are shown as mean ± s.e.m. of fold changes compared to levels in medium before incubation with AT2 cells ($n = 6$ biological replicates). One-way analysis of variance (ANOVA) with Tukey's multiple comparison test.

stimulated 3D but not 2D growth of 4T1 cells (Fig. 3d and Extended Data Fig. 3f,g). In accordance with our in vivo data, 3D spheroid growth of low metastatic 4T07 cancer cells also increased with extra palmitate (Extended Data Fig. 3h).

As oleate can buffer the effects of palmitate in cancer cells[20–22], we also investigated the combination of both fatty acids. Unexpectedly, the growth increase observed with extra palmitate was also present when palmitate was combined with oleate (Extended Data Fig. 3i), whereas stearate did not phenocopy palmitate (Extended Data Fig. 3j), suggesting that only palmitate promotes spheroid growth of 4T1 breast cancer cells. Taken together, these data show that breast cancer-derived lung metastases are enriched in palmitate and that increasing palmitate availability further promotes spheroid growth.

CPT1a expression is upregulated in breast cancer metastases

Palmitate can have different fates in cells. Therefore, we analyzed lipid-processing pathways using RNA-seq comparing 3D- versus 2D-cultured 4T1 cells with additional palmitate and 3D cultures with and without it. Despite mitochondrial mass being unchanged (Extended Data Fig. 4a), we found that carnitine palmitoyltransferase 1a (CPT1a),

which facilitates the import of long-chain fatty acids into the mitochondria, was within the highest-ranking lipid-processing enzymes whose gene expression increased in 3D compared to 2D cultures and upon additional palmitate availability in 3D cultures (Extended Data Fig. 4b,c). We confirmed this increase at the protein level in 4T1 as well as in human MCF7 and MCF10A H-Ras^{V12} breast cancer cells (Fig. 3e and Extended Data Fig. 4d). Moreover, lung metastases, compared to the corresponding primary 4T1 and EMT6.5 breast tumors, displayed increased CPT1a expression (Fig. 3f). Additionally, we found that CPT1a expression was higher in metastases compared to primary tumor tissues of patients with breast cancer (Fig. 3g; Expression Project for Oncology (expO), Gene Expression Omnibus (GEO) accession no. GSE2109).

Next, we performed RNA-seq on breast primary tumors of 14 patients who had metastases at diagnosis compared to 44 patients who did not have metastases at diagnosis and did not develop any within at least 7 years (CHEMOREL study at UZ Leuven; Supplementary Table 3). We observed that patients with metastatic breast cancer at diagnosis had higher *CPT1A* expression in their primary breast tumors compared to patients who did not develop metastases for at least 7 years (Fig. 3h). We further analyzed gene expression data from patients with breast cancer (The Cancer Genome Atlas (TCGA)[23] and METABRIC[24]) and found that high CPT1a expression (above median) in primary breast tumors of patients was significantly associated with decreased overall survival (Fig. 3i). This association was confirmed after correcting for common clinicopathological variables (age, tumor stage and tumor subtype; Supplementary Table 4, HR_{adj} (95% confidence interval) 1.73 (1.20–2.51) and HR_{adj} 1.22 (1.05-1.43) in TCGA and METABRIC dataset, respectively; Extended Data Fig. 4e). Based on these data, we concluded that CPT1a may be important for breast cancer progression in patients and that breast cancer-derived metastases may rely on CPT1a to process palmitate.

Metastasis requires CPT1a in lean and high-fat diet mice

We then assessed how CPT1a inhibition affects palmitate-promoted spheroid growth. We found that genetic or pharmacologic inhibition of CPT1a decreased spheroid size and number to the level observed without additional palmitate in 4T1, MCF7 and MCF10A H-Ras^{V12} cells (Fig. 4a,b and Extended Data Fig. 4f–h). Based on this in vitro finding, we hypothesized that blocking CPT1a is sufficient to reduce lung metastasis formation. We assessed experimental and spontaneous lung metastasis formation by injecting control and CPT1a knockout/down cells intravenously (4T1, EMT6.5 and EO771-MC3B) or into the mammary fat pad (4T1) of mice, respectively. We observed that metastatic burden was highly reduced in the absence of CPT1a expression compared to control (Fig. 4c,d and Extended Data Fig. 5a), whereas primary tumor growth showed no changes (upon CPT1a knockdown) and a small reduction (upon CPT1a knockout) compared to control (Extended Data Fig. 5b). Similarly, also i.v. injections of CPT1a-silenced 4T1, EMT6.5 and EO771-MC3B breast cancer cells resulted in reduced metastasis formation compared to control (Fig. 4e–h) showing that this effect was not dependent on the dissemination of cancer cells from the primary tumor. In line, we did not observe differences in the invasion and migration capacity of 4T1 cells upon CPT1a inhibition in vitro (Extended Data Fig. 6a,b). Furthermore, inhibiting CPT1a by treating mice after initial metastatic colonization (day 4) with etomoxir (40 mg kg^{-1} intraperitoneally (i.p.) daily) also reduced metastasis formation (Fig. 4g). Thus, we concluded that blocking CPT1a is sufficient to impair the growth of breast cancer cells in the lung environment.

Next, we hypothesized that CPT1a also mediates the increased growth capacity of metastases in HFD-fed mice. We injected i.v. 4T1 and EMT6.5 control and CPT1a-silenced cells expressing the congenic marker CD90.1 into mice on CD or HFD. Assessing metastatic burden after 12 d, we found an increased fraction of CD90.1-positive cells in the lung of HFD compared to CD mice (Fig. 4h). Silencing CPT1a was sufficient to prevent this increase induced by HFD (Fig. 4h). This striking dependence on CPT1a was also observed in spontaneous metastases arising in HFD-fed mice (Fig. 4i and Extended Data Fig. 5). These results show that lung metastasis formation depends on CPT1a in lean and HFD mice.

CPT1a activity sustains acetyl-CoA levels

Next, we investigated the mechanism by which palmitate supports metastasizing cells. CPT1a facilitates the transport of long-chain fatty acyl-CoAs into the mitochondria and one of the main fates for those is the subsequent oxidation to acetyl-CoA in the β-oxidation pathway. Therefore, we measured acetyl-CoA abundance in 3D spheroids and metastases tissue. We found that acetyl-CoA abundance was higher in breast cancer cells supplemented with extra palmitate in 3D compared to 2D culture (Fig. 5a) and in the lung metastases compared to primary 4T1 and EMT6.5 breast tumors (Fig. 5b,c). Accordingly, acetyl-CoA abundance decreased in 3D cultured mouse (4T1 and EMT6.5) and human (MCF7 and MCF10A H-Ras^{V12}) breast cancer cells upon CPT1a silencing (Extended Data Fig. 6c–e) as well as in 4T1 lung metastases when mice were treated with etomoxir (40 mg kg^{-1}, i.p. once a day starting 72 h before euthanasia[25]) (Fig. 5c). Without extra palmitate, CPT1a silencing did not decrease acetyl-CoA abundance in 3D-cultured 4T1 breast cancer cells (Extended Data Fig. 6d). Moreover, the 3D growth defect observed upon CPT1a inhibition was rescued by acetate (5 mM; Fig. 4a,b) and octanoate (130 µm, Extended Data Fig. 6f), which are CPT1a-independent sources of acetyl-CoA. These findings show that breast cancer spheroids in the presence of additional palmitate and breast cancer-derived lung metastases rely on CPT1a for acetyl-CoA production.

Fig. 3 | Intracellular palmitate levels and CPT1a expression are increased in breast cancer spheroids and lung metastases. a, Matrix-assisted laser desorption ionization mass spectrometry imaging (MALDI–MSI) (50-µm pixel) of lipids PC O-18:1/16:0, PC 20:1_16:0 and PC18:1_16:0 within the lung tissue. Metastases are identified by optical image of the lung tissue section following by H&E staining and are denoted by red line based on bisecting *k*-means segmentation map. **b**, Fatty acid (FA) abundance in 4T1 and EMT6.5 primary tumor tissues and the matching lung metastases. Data represent normalized metabolite ion counts ($n = 5$ mice). Unpaired nonparametric two-tailed Mann–Whitney *U*-tests. 4T1 model, $^{**}P = 0.007$; EMT6.5 model, $^{**}P = 0.0079$. AU, arbitrary units; m.f., mammary fat pad; M, mouse. **c**, Intracellular palmitate abundance from mouse (4T1, $n = 3$ and EMT6.5, $n = 4$) and human (MCF10A H-Ras^{V12}, $n = 3$ and MCF7, $n = 4$) breast cancer cells cultured on soft-agar (3D) or attached (2D) conditions. Data are presented as mean ± s.e.m. (*n* indicates biological replicates). Unpaired two-tailed *t*-tests with Welch correction. **d**, 3D spheroid growth upon palmitate ($n = 5$) or oleate ($n = 9$) supplementation compared to control ($n = 6$) represented by the average of spheroids area of >100 spheroids. Data are presented as mean ± s.e.m. (*n* indicates biological replicates). One-way ANOVA with Holm-Sidak's multiple comparison test. **e**, CPT1a expression in breast cancer cells growing in 2D monolayer or 3D spheroid with or without additional palmitate. A representative image of $n = 3$ experiments is shown. **f**, Relative *Cpt1a* gene expression in 4T1 ($n = 4$ mice) and EMT6.5 ($n = 3$ mice) breast-derived lung metastases normalized to *Cpt1a* gene expression of their breast primary tumors. Data are presented as mean ± s.e.m. Unpaired nonparametric two-tailed Mann–Whitney *U*-tests. **g**, *CPT1A* gene expression in breast primary tumors ($n = 39$ patients) compared to metastatic tissues ($n = 7$ patients) (GEO accession no. GSE2109 (HS00002(33)). Data are presented as mean ± s.d. Unpaired two-tailed *t*-tests with Welch correction. **h**, Differently expressed genes in primary tumors of metastatic patients (metastasis already present at diagnosis) compared to non-metastatic patients (no metastasis during at least 7 years of follow-up). *CPT1A* transcript is identified as upregulated (considering a false discovery rate (FDR)-adjusted *P* value threshold of <0.05) and is colored in red. Multiple testing correction with FDR estimation. **i**, Kaplan–Meier survival for patients with breast cancer with high or low levels of *CPT1a* gene expression. Comparison of survival curves was conducted using Mantel–Cox test and Gehan–Breslow–Wilcoxon test ($n = 369$ patients).

https://doi.org/10.1038/s43018-023-00513-2

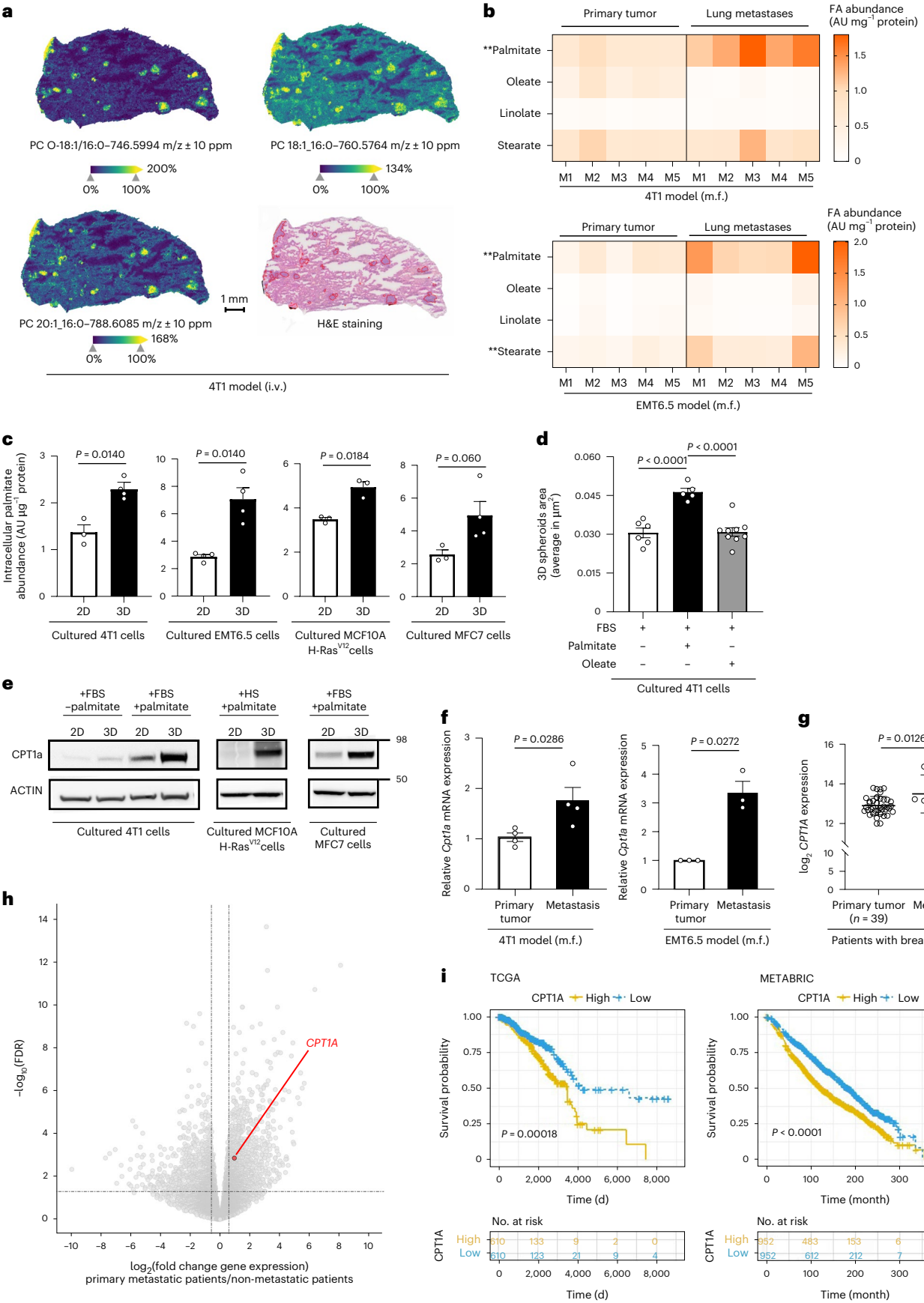

CPT1a-mediated palmitate oxidation increases NF-κB signaling

Next, we addressed how CPT1a-derived acetyl-CoA supports metastasizing cells. If acetyl-CoA is required outside mitochondria, inhibiting ATP citrate lyase (ACLY) is expected to phenocopy CPT1a inhibition (Extended Data Fig. 6g). Indeed, we found that inhibiting ACLY with BMS-303141 (20 µm for 5 d; ACLYi) decreased 3D growth to a similar extent as CPT1a inhibition and that acetate rescued this growth defect (Fig. 5d,e). Moreover, the level of ATP, a product of mitochondrial acetyl-CoA metabolism, was not significantly altered upon CPT1a deletion and acetate supplementation (Extended Data Fig. 6h). Thus, we investigated possible fates of acetyl-CoA beyond mitochondria metabolism. One such possibility is histone acetylation[26]. Yet, we found no prominent changes in histone acetylation in 3D-cultured 4T1 cells upon CPT1a silencing using proteomics (Extended Data Fig. 6i). Therefore, we further investigated non-histone protein acetylation, which may be connected to gene expression regulation[27]. We performed RNA-seq and consecutive gene set enrichment analysis (GSEA) in 4T1 spheroids upon CPT1a deletion and acetate rescue. Among the highest-ranking gene sets (Extended Data Fig. 7a) was a signature for NF-κB signaling that decreased upon CPT1a deletion and was rescued with acetate (Fig. 5f and Extended Data Fig. 7b). These gene expression changes were confirmed in an additional breast cancer cell line (Extended Data Fig. 7c). Conversely, we analyzed all CPT1a-dependent and acetate-rescued gene expression changes to predict upstream regulators using ingenuity pathway analysis[28]. Notably, several upstream regulators of the NF-κB signaling pathway scored within the top 30 predicted regulators (Extended Data Fig. 7d). Thus, this shows that NF-κB signaling is likely induced by palmitate in a CPT1a-dependent manner. NF-κB signaling can induce an epithelial-to-mesenchymal transition (EMT)[1,29]. Accordingly, we found a reduced EMT signature upon CPT1a deletion that was rescued with acetate (Extended Data Fig. 7e). Moreover, we analyzed publicly available data from patients with metastatic breast cancer and found an overrepresentation of NF-κB signaling in the lung, liver and bone metastases, which grow in lipid-rich environments (Fig. 1a,b and elsewhere[30]) compared to brain metastases where cerebrospinal fluid and interstitial fluid are lipid deprived environments[31,32] (Fig. 5g). Thus, these data are consistent with the notion that NF-κB signaling is activated downstream of the CPT1a-mediated palmitate oxidation in 3D spheroids.

CPT1a promotes acetylation of the NF-κB subunit p65

Acetylation of the NF-κB family member p65 is known to dynamically regulate NF-κB activation and transcriptional activity[33]. Thus, we asked whether p65 acetylation is regulated by CPT1a. To address this question, we determined the amount of total p65 binding to the DNA by electrophoretic mobility shift assay (EMSA) and p65 acetylated at K310 in the nucleus upon CPT1a silencing and upon acetate supplementation in 4T1 spheroids using acetylation-specific western blot analysis. Total nuclear p65 and DNA-binding activity were not changed (Fig. 6a and Extended Data Fig. 7f), which may indicate that the genome-wide distribution of p65 is not altered; however, we found that K310 acetylated p65 in the nucleus decreased upon CPT1a silencing and was rescued upon acetate supplementation (Fig. 6a). These findings suggest an importance of p65 acetylation in mediating the transcription of distinct NF-κB targets.

Next, we modulated NF-κB signaling and assessed spheroid growth. Tumor necrosis factor (TNF)-α is an activator of NF-κB, whereas pyrrolidine-dithiocarbamate ammonium (PDTC) at 0.5 µm for 5 d (NF-κBi) blocks the translocation of p65 into the nucleus, reducing its transcriptional activity[34]. Treating 4T1 and MCF10A H-Ras^{V12} cancer cells with TNF-α increased spheroid growth even without extra palmitate, whereas NF-κBi treatment decreased spheroid growth in the presence of extra palmitate (Fig. 6b,c). Accordingly, acetate no longer rescued spheroid growth in the presence of NF-κBi (Fig. 6d). Therefore, we concluded that palmitate-derived acetyl-CoA production is required for p65 acetylation and downstream NF-κB signaling.

KAT2a acetylates p65 in the presence of palmitate

Next, we asked how palmitate, but not other fatty acids, can increase p65 acetylation. One possibility is that a specific acetyltransferase mediates the palmitate-derived acetylation of p65. Thus, we compared the gene expression of several acetyltransferases in 4T1 spheroids with or without extra palmitate. Notably, we discovered that only lysine acetyltransferase 2a (KAT2a or GCN5) was significantly induced in the presence of palmitate (Fig. 7a). Neither oleate nor acetate addition increased KAT2a gene and protein expression (Fig. 7b and Extended Data Fig. 8a), although both increased acetyl-CoA levels (Extended Data Fig. 8b). This observation suggests that the palmitate-specific effect is mediated by KAT2a.

KAT2a has been mainly studied concerning the acetylation of histone H3K9 and some non-histone targets[35,36]. Therefore, we evaluated whether KAT2a could affect p65 indirectly via H3K9 acetylation by chromatin immunoprecipitation (ChIP) sequencing. We found that the loss of either KAT2a or CPT1a only resulted in minor changes in H3K9 acetylation (Extended Data Fig. 8c) that were not rescued by acetate (Extended Data Fig. 8d). Despite that, a decrease in the transcription of NF-κB targets upon CPT1a or KAT2a deletion and rescue with acetate was observed (Extended Data Fig. 8e). Consequently, we deemed it unlikely that KAT2a promotes metastasis via histone acetylation.

Next, we investigated whether KAT2a directly acetylates p65, as a physical interaction was shown during hippocampal memory regulation[37]. We deleted KAT2a in 4T1 cells and assessed the presence of K310 acetylated p65 in the nucleus. As observed with CPT1a

Fig. 4 | Silencing CPT1a counteracts palmitate-induced spheroid growth and inhibits metastasis formation in lean and HFD mice. a,**b**, 3D spheroid growth of 4T1 (n = 9, 15, 9, 8, 9 and 7 biological replicates, respectively) and MCF10A H-Ras^{V12} cells (n = 5 biological replicates) upon palmitate supplementation (75 µm), CPT1a genetic inhibition performed by shRNA (sh*Cpt1a* and sh*CPT1A*) and CRISPR (sg*Cpt1a*) compared to cells infected with non-targeted sh/sgRNA as a control and upon metabolic rescue by acetate (5 mM), represented by the average of spheroids area of >100 spheroids. Data are presented as mean ± s.e.m. One-way ANOVA with Tukey's multiple comparison test. **c**,**d**, Metastatic burden in the lung of mice injected with 4T1 in the m.f. upon genetic knockdown (n = 19 mice) (**c**) or knockout (n = 12 mice) (**d**) of *Cpt1a* compared to cells infected with non-targeted sgRNA or shRNA as a control (n = 12 and 11 mice, respectively), analyzed by H&E staining. Data are presented as mean ± s.e.m. Data for sgControl and *sgCpt1a* are also shown in Fig. 7f. Unpaired two-tailed t-tests with Welch correction. Representative H&E staining images are shown in Extended Data Fig. 5a. **e**,**f**, Total area and number of metastases in the lung of mice after 12–14 d of i.v. injections with EMT6.5 (n = 5 and 8 mice) or EO771-MC3B (n = 8 mice) cancer cells previously transduced with a lentiviral vector with shRNA against *Cpt1a* or scramble sequence as a control and analyzed by H&E staining. Data are presented as mean ± s.e.m. Unpaired two-tailed t-tests with Welch correction. Representative H&E staining images are shown in Extended Data Fig. 5a. **g**, Percentage of breast cancer cells present in the lung of mice after 14 d of i.v. injections with CD90.1-4T1 cells. Mice were treated i.p. with the CPT1a inhibitor etomoxir (40 mg kg^{-1}, n = 7 mice) or vehicle (water, n = 12 mice) daily starting after 4 d of cancer cell injections. Data are presented as mean ± s.e.m. Unpaired two-tailed t-tests with Welch correction. **h**, Percentage of cancer cells (mean ± s.e.m.) present in the lung of mice after 12 d of i.v. injections with CD90.1-labeled 4T1 (n = 4 mice per group) or EMT6.5 (n = 8 mice per group) cancer cells and expressing shRNA against *Cpt1a* or scramble sequence as a control. Before injections, mice were maintained for 16 weeks on CD and HFD. Data for 4T1 shControl in CD and HFD are also shown in Fig. 1d. Two-way ANOVA with Tukey's multiple comparison test. **i**, Metastatic burden in the lung of mice injected with 4T1 in the m.f. upon *Cpt1a* knockout (n = 5 mice, 10 lung sections) compared to cells infected with non-targeted sgRNA as a control (n = 6 mice, 12 lung sections), analyzed by H&E staining. Data are presented as mean ± s.e.m. Before injections, mice were maintained for 16 weeks on CD and HFD. Unpaired two-tailed t-tests with Welch correction. Representative H&E staining images are shown in Extended Data Fig. 5a.

https://doi.org/10.1038/s43018-023-00513-2

deletion, total p65 and general binding to DNA were not notably altered (Fig. 7c and Extended Data Fig. 7f). However, in line with the hypothesis that KAT2a is responsible for acetylating p65 in the presence of palmitate, we observed that its deletion decreased the amount of K310 acetylated p65 in the nucleus (Fig. 7c). Subsequently, we investigated whether blocking KAT2a and thus p65 acetylation, prevents the palmitate-induced spheroid growth. KAT2a inhibition did not decrease proliferation of cancer cells growing in 2D (Extended Data Fig. 8f); however, KAT2a deletion reduced 3D 4T1 spheroid size and number to a similar degree as CPT1a deletion (Fig. 7d and Extended Data Fig. 8g,h). Accordingly, 3D growth of 4T1, MCF7 and MCF10A H-Ras^{V12} was significantly reduced upon treatment with the KAT2a inhibitor cyclopentylidene-[4-(4′-chlorophenyl)thiazol-2-yl]hydrazone (CPTH2) at 2 µm for 5 d[38] (Fig. 7e and Extended Data Fig. 8g). Moreover, breast cancer spheroids showed sensitivity to CPTH2 only in the presence of extra palmitate but not in the absence of extra palmitate (Extended Data Fig. 8i). Based on these data, we concluded that KAT2a acetylates p65 in the presence of palmitate and that this activity is essential for palmitate-promoted spheroid growth.

KAT2a deletion impairs metastasis formation

Next, we assessed whether blocking KAT2a, and hence p65 acetylation, is sufficient to impair lung metastasis formation. We injected 4T1 control and KAT2a knockout cells into the mammary fat pad of mice or i.v. and assessed lung metastases number, area and metastatic index based on hematoxylin and eosin (H&E) staining. We observed that metastatic burden was dramatically reduced in the absence of KAT2a expression compared to control (Fig. 7f and Extended Data

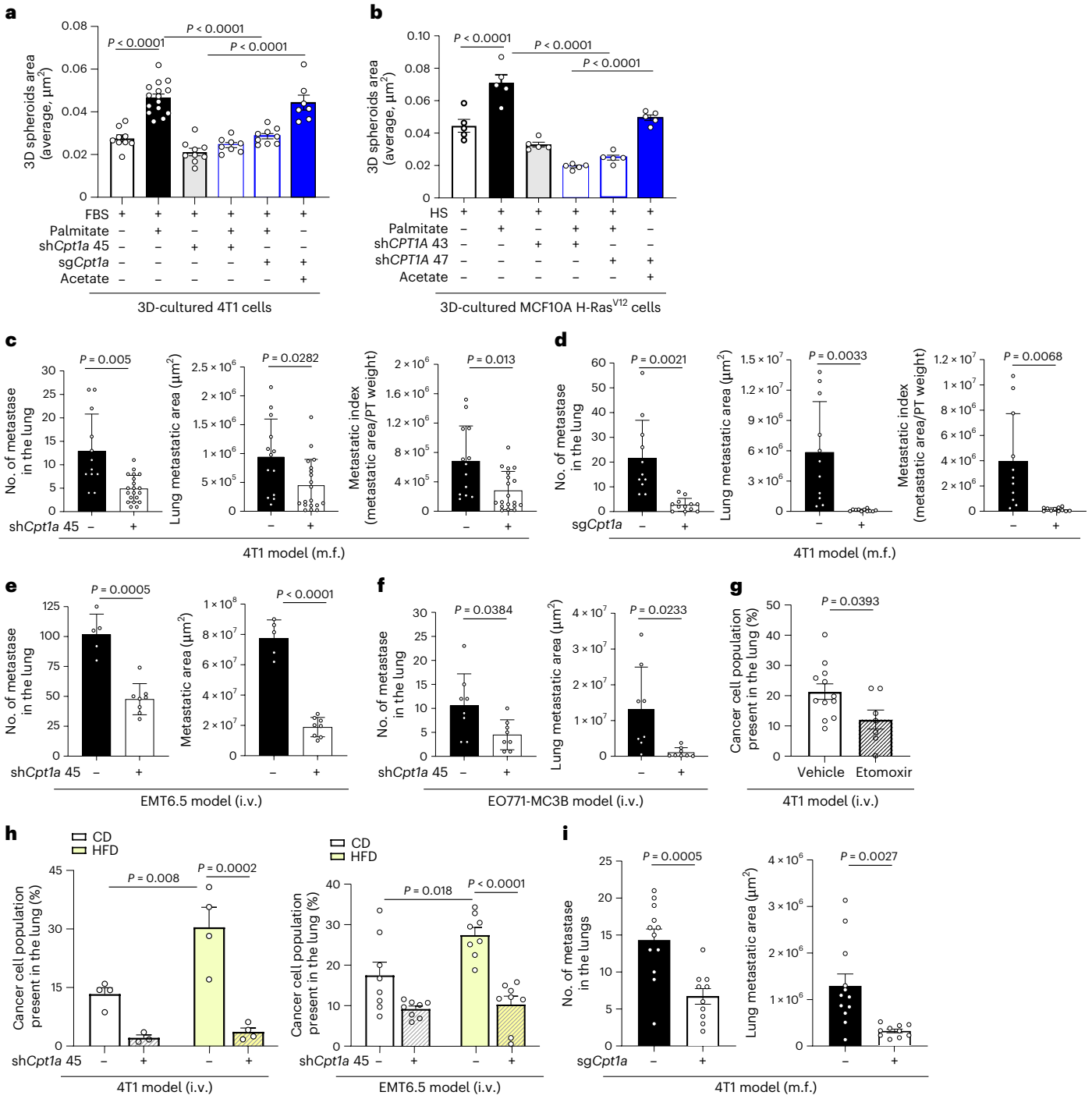

https://doi.org/10.1038/s43018-023-00513-2

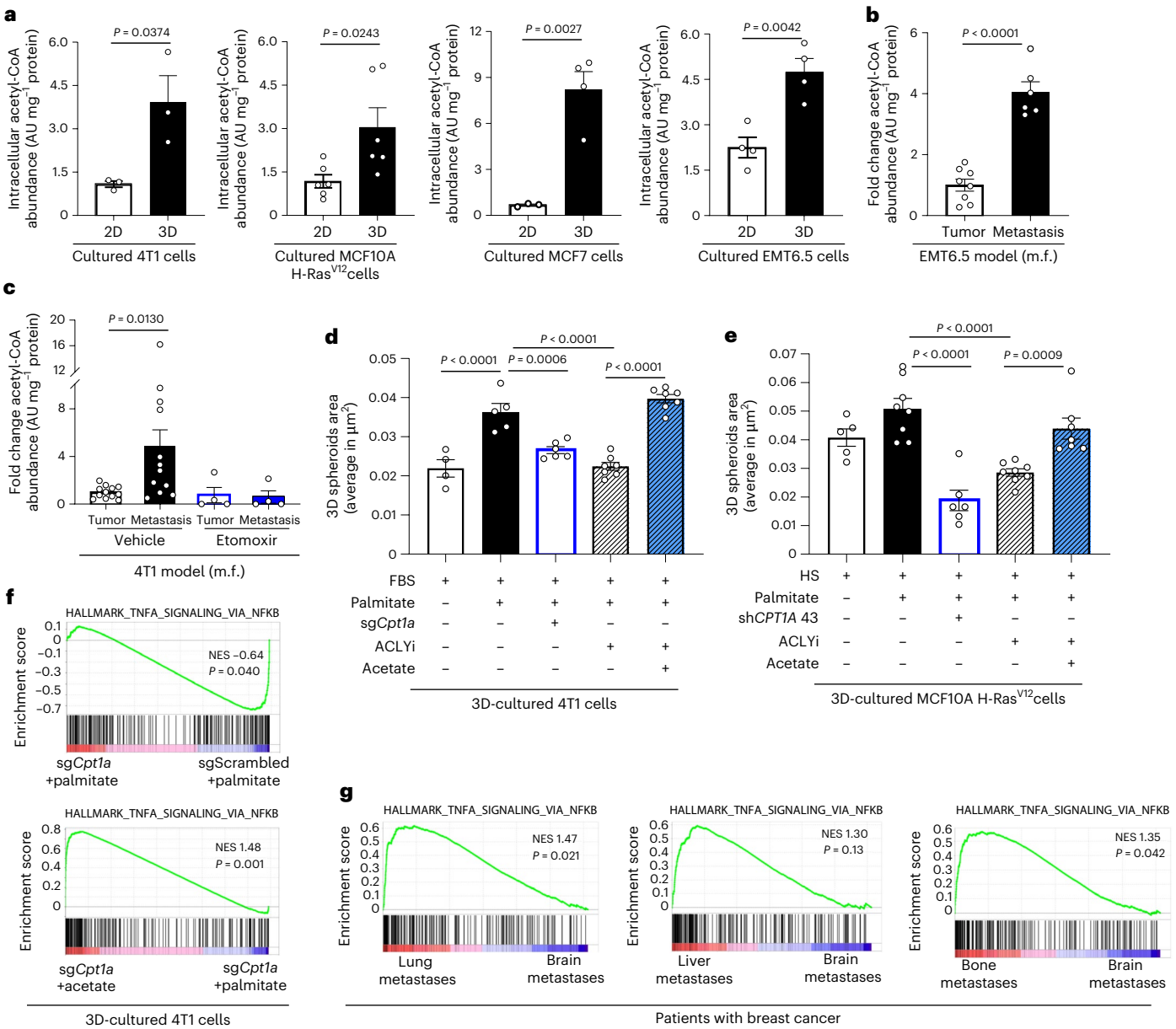

Fig. 5 | CPT1a activity sustains acetyl-CoA levels in spheroids and lung metastases. a, Intracellular levels of acetyl-CoA in breast cancer cells incubated in 2D monolayer and 3D spheroids cultures for 5 d in medium containing extra palmitate. Data are presented as mean ± s.e.m. (4T1, $n = 3$ and 4; MCF10A H-Ras^{V12}, $n = 6$; MCF7, $n = 3$ and 4; EMT6.5, $n = 4$, biological replicates). Unpaired two-tailed *t*-tests with Welch correction. **b**, Relative changes in acetyl-CoA abundance in EMT6.5 (m.f.) breast primary tumors and lung metastases. Data are shown as fold changes compared to acetyl-CoA abundance in primary tumors. Data are presented as mean ± s.e.m. ($n = 4$ mice). Unpaired two-tailed *t*-tests with Welch correction. **c**, Relative changes in acetyl-CoA abundance in 4T1 (m.f.) breast primary tumors and lung metastases upon acute inhibition of CPT1A using the inhibitor etomoxir (40 mg kg^{-1} i.p., $n = 4$ mice) or vehicle (water, $n = 12$ mice). Data are shown as fold changes compared to acetyl-CoA abundance in primary tumors of the group of mice treated with vehicle. Data are presented as mean ± s.e.m. and points represented as zero were below the detection limit. One-way ANOVA with Dunnett's multiple comparison test. **d**,**e**, 3D spheroid growth upon genetic inhibition of either *Cpt1a*/*CPT1A* compared to cells infected with scramble as a control together with pharmacologic ACLY inhibition using BMS-303141 (20 µm, 5 d) in 4T1 ($n = 4$, 5, 6, 7 and 7 biological replicates, respectively) (**d**) and MCF10A H-Ras^{V12} cells ($n = 5$, 6, 8, 8 and 7 biological replicates, respectively) (**e**) with or without extra palmitate and in the presence of acetate as metabolic rescue (5 mM, 5 d). 3D spheroid growth is represented by the average spheroids area of >100 spheroids. Data are presented as mean ± s.e.m. One-way ANOVA with Tukey's multiple comparison test. HS, horse serum. **f**, GSEA enrichment plots comparing gene expression profiles in 4T1 3D spheroids transduced with a lentiviral vector containing sg*Cpt1a* or sgControl (top) and sg*Cpt1a* 4T1 3D spheroids cultured with or without acetate (bottom). NES, normalized enrichment score. *P* value indicates the significance of the enrichment score (permutation test). **g**, GSEA enrichment plots comparing gene expression profiles of HALLMARK_TNFA_SIGNALING_VIA_NFKB signature from the Molecular Signature Database (MsigDB) in breast cancer metastases at different organ sites from patients (GSE14018). *P* value indicates the significance of the enrichment score (unpaired one-tailed *t*-tests).

Fig. 5a), whereas primary tumor growth showed only a small reduction compared to control (Extended Data Fig. 5b). A similar reduction in metastases area was observed upon i.v. injection of cancer cells (Extended Data Fig. 8j). Thus, we concluded that blocking KAT2a phenocopies CPT1a inhibition and is sufficient to impair metastatic growth in mice.

Finally, we investigated whether this CPT1a-KAT2a-driven mechanism may occur in patients with metastatic breast cancer. We argued

https://doi.org/10.1038/s43018-023-00513-2

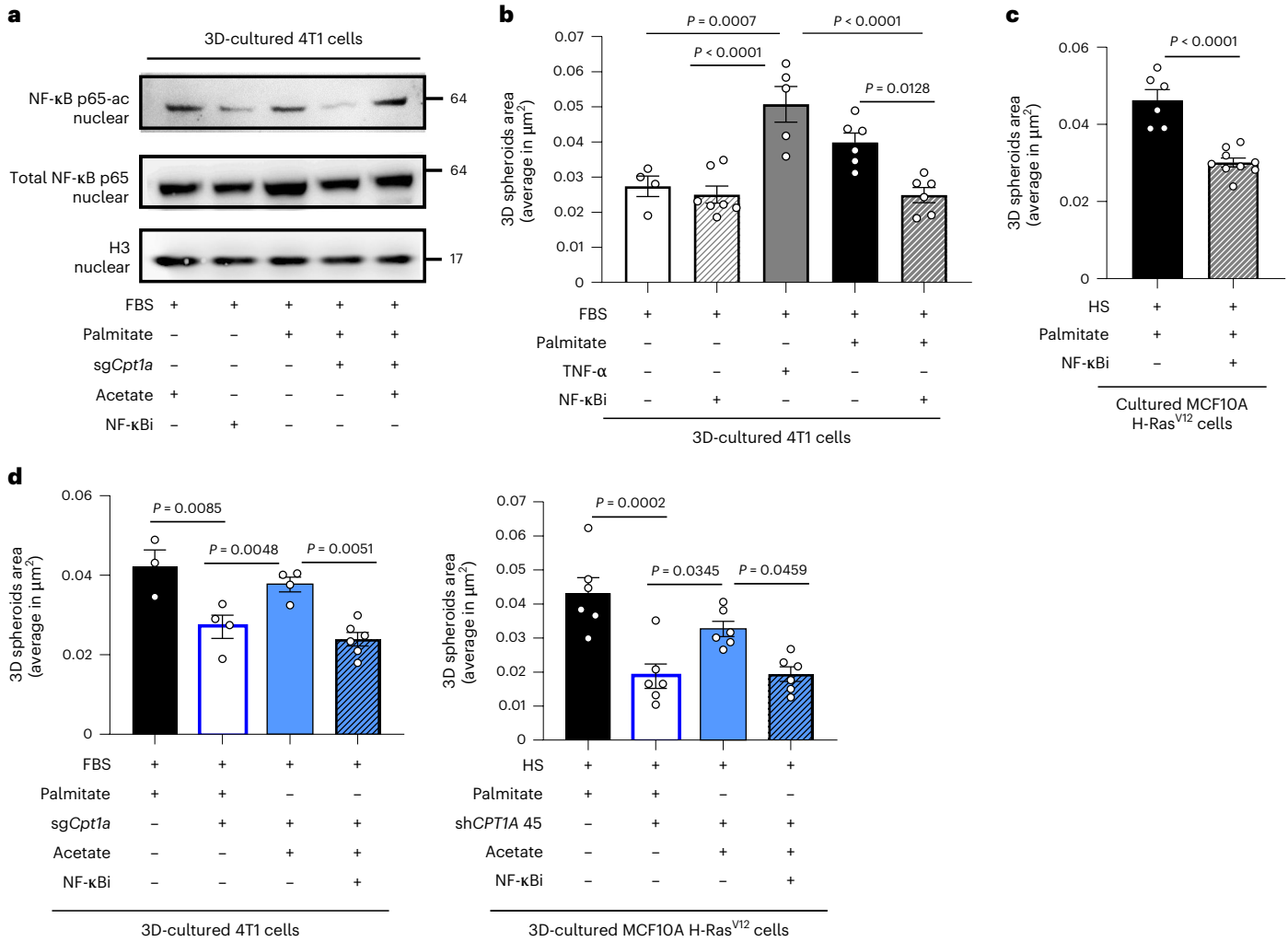

Fig. 6 | CPT1a is required for p65 acetylation and NF-κB signaling. **a**, Acetylated p65 (NF-κB p65ac) in nuclear extracts of 3D spheroids transduced with a lentiviral vector containing sg*Cpt1a* or sgControl and cultured for 3 d in the presence of extra palmitate (75 µm), acetate (5 mM) or the NF-κB inhibitor PDTC (0.5 µm). Histone H3 is shown as a loading control of NF-κB p65ac. A representative of $n = 3$ experiments is shown. **b**,**c**, 3D growth (5 d) of 4T1 ($n = 4$, 7, 5, 6 and 6 biological replicates, respectively) (**b**) and MCF10A H-Ras^{V12} cells ($n = 6$ and 9 biological replicates) (**c**) upon treatment with the NF-κB inhibitor (PDTC, 0.5 µm) in the presence of extra palmitate and 4T1 3D spheroid growth upon activation of the pathway via either supplementation of TNF-α (10 ng µl^{-1}) or extra palmitate (75 µm) is shown. 3D spheroid growth is represented by the average spheroids area of >100 spheroids. One-way ANOVA with Tukey's multiple comparison test (4T1) and Unpaired two-tailed *t*-tests with Welch correction (MCF10A H-Ras^{V12}). Data are presented as mean ± s.e.m. **d**, 3D growth (5 d) of 4T1 ($n = 3$, 4, 4 and 6 biological replicates, respectively) and MCF10A H-Ras^{V12} ($n = 6$ biological replicates) cells upon treatment with the NF-κB inhibitor to the inhibitory impact of CPT1a inhibition (sg*Cpt1a*) compared to non-targeting shRNA as a control, in the presence of the extra palmitate (75 µm) or acetate as metabolic rescue (5 mM). 3D spheroid growth is represented by the average spheroids area of >100 spheroids. Data are presented as mean ± s.e.m. One-way ANOVA with Tukey's multiple comparison test.

that metastases growing in palmitate-enriched organs require coexpression of CPT1a and KAT2a. We therefore collected metastases tissues from different organs of two patients with breast cancer within the UPTIDER rapid autopsy program (Supplementary Table 2) and determined CPT1a and KAT2a protein expression. Consistent with the determined mechanism, we observed that CPT1a and KAT2a proteins were coexpressed within lung and liver metastases compared to cranial bone and lymph node metastases (Fig. 7g,h), with the latter being an oleate-enriched organ[39]. We therefore concluded that CPT1a and KAT2a may act in concert in patients with breast cancer to promote metastatic growth in organs whose interstitial nutrient composition is palmitate enriched.

In conclusion, we identify palmitate priming of the lung by AT2 resident cells during pre-metastatic niche formation and upon HFD exposure. Metastasizing cancer cells rely on CPT1a-dependent palmitate oxidation to acetyl-CoA, which in turn serves as a substrate for the acetylation of p65 by KAT2a. Subsequently the pro-metastatic NF-κB transcriptional program is activated supporting metastatic growth in palmitate-rich environments (Fig. 7h).

Discussion

Here, we provide an analysis of lipid availability in the interstitial fluid of the lungs and livers in healthy and pathological conditions. Furthermore, we functionally link palmitate-rich environments to protein acetylation upstream of a pro-metastatic NF-κB signaling. Palmitate can induce a pro-metastatic memory in primary tumors via histone H3 lysine 4 trimethylation, stimulating intratumor Schwann cells and innervation[40]. Adding to this known mechanism we discovered an epigenetically independent role of palmitate in promoting metastasis formation in the distant organ.

https://doi.org/10.1038/s43018-023-00513-2

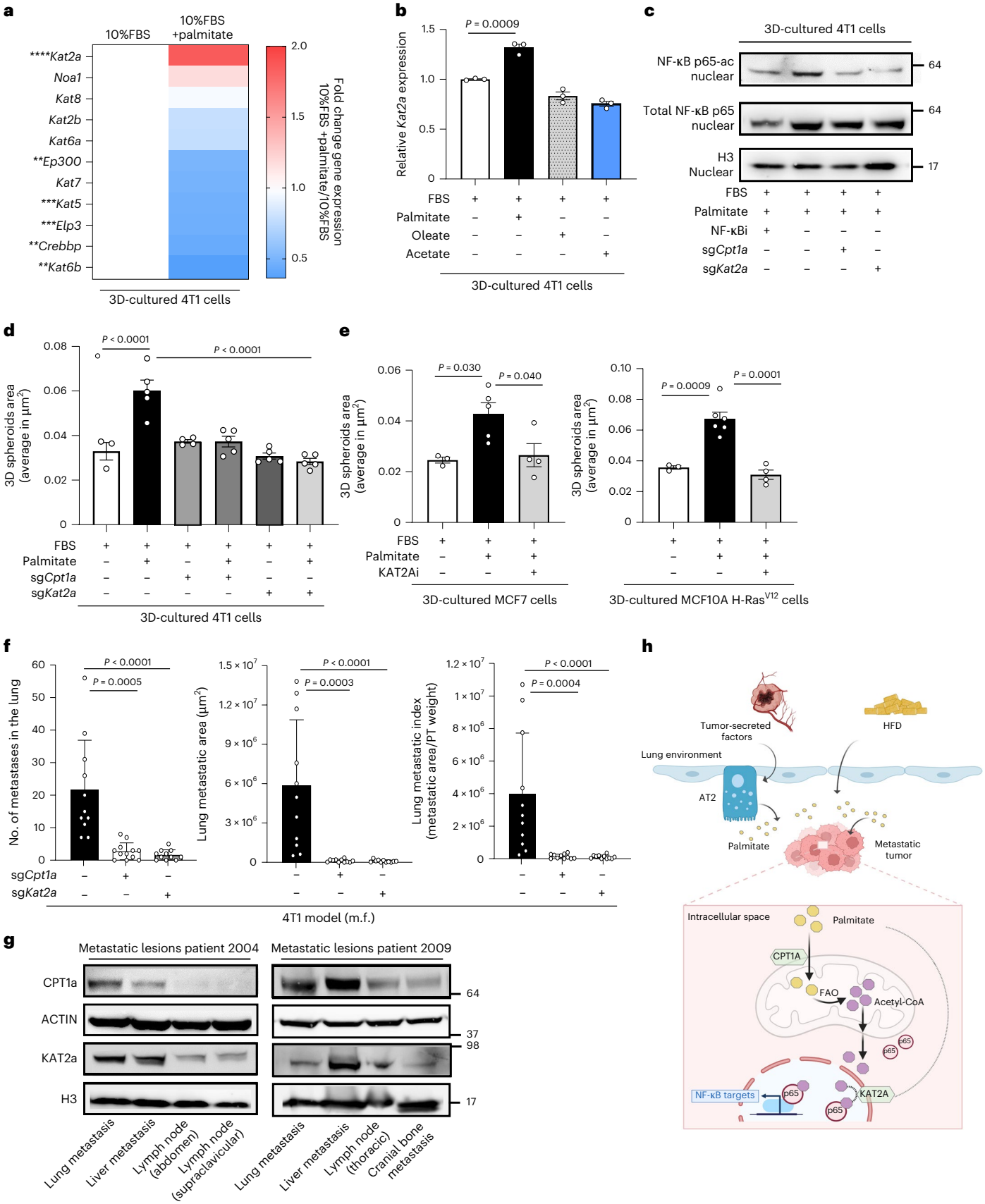

Palmitate and obesity are associated with inflammatory NF-κB signaling in stromal cells[41–45] and, in cancer cells, it was suggested that etomoxir reduces phosphorylation of IκBα[46]. Here, we discovered a mechanism by which CPT1a-dependent palmitate oxidation regulates NF-κB signaling via acetylation of p65. Moreover, we find that the acetyltransferase KAT2a is only important for p65 acetylation in

Fig. 7 | CPT1a and KAT2a are coexpressed in palmitate-enriched environments and their silencing impairs metastasis formation. a, Differential expression of acetyltransferases in 4T1 3D spheroids with or without palmitate supplementation after 5 d of incubation. Data represent the fold changes compared to the non-supplemented condition ($n = 4$ biological replicates). Unpaired two-tailed *t*-tests with Welch correction. *Kat2a*, ****$P < 0.0001$; *Ep300*, $P = 0.002$; *Kat5*, ***$P = 0.001$; *Elp3*, ***$P = 0.001$; *Creppb*, **$P = 0.006$; *Kat6a*, **$P = 0.002$. **b**, Relative *Kat2a* expression in 4T1 3D spheroids (5 d) with or without additional palmitate (75 µm), oleate (116 µm) or acetate (5 mM) ($n = 6$ biological replicates). One-way ANOVA with Tukey's multiple comparison test. **c**, Acetylated p65 (NF-κB p65ac) in nuclear extracts of 3D spheroids transduced with a lentiviral vector containing sg*Cpt1a*, sg*Kat2a* or sgControl and cultured for 3 d in the presence of extra palmitate (75 µm) or the NF-κB inhibitor PDTC (0.5 µm). Histone H3 is shown as a loading control of NF-κB p65ac. A representative of $n = 3$ experiments is shown. **d**, 3D spheroid growth of 4T1 cells silenced for *Cpt1a* or *Kat2a* compared to non-targeting sgRNA as a control, with or without extra palmitate (5 d). Data are presented as mean ± s.e.m. ($n = 4, 5, 4, 5, 5$ and 5 biological replicates, respectively). One-way ANOVA with Tukey's multiple comparison test. **e**, 3D spheroid growth represented by the average spheroids area of >100 spheroids in MCF7 ($n = 3, 4$ and 5 biological replicates) and MCF10A H-Ras^{V12} cells ($n = 3, 6$ and 4 biological replicates) upon pharmacologic inhibition of KAT2a using the inhibitor CPTH2 (5 µm) cultured for 5 d with or without palmitate supplementation. Data are presented as mean ± s.e.m. One-way ANOVA with Tukey's multiple comparison test. **f**, Metastatic burden in the lungs of mice injected with 4T1 into the m.f. upon genetic knockout of *Cpt1a* ($n = 12$ mice) and *Kat2a* ($n = 11$ mice) compared to non-targeting sgRNA ($n = 12$ mice) as a control. Data are presented as mean ± s.e.m. Data for control and *sgCpt1a* are also shown in Fig. 4c. One-way ANOVA with Dunnett's multiple comparison test. **g**, CPT1a and KAT2a protein expression in different metastasis sites of patients with breast cancer in 2004 and 2009 from the UPTIDER program. A representative of $n = 2$ experiments is shown. **h**, Tumor-secreted factors and HFD are two independent factors increasing palmitate levels in the lung environment. Metastasizing cancer cells use the available palmitate to drive p65 acetylation in a CPT1a-dependent manner resulting in pro-metastatic NF-κB signaling.

the presence of extra palmitate. This provides strong evidence of a nutrient environment-dependent regulation of protein acetylation in organs of metastasis.

Acetyl-CoA levels are linked to Smad2[47] and histone[48–50] acetylation with subsequent breast cancer metastasis[47,48]. In the liver, HFD exposure elevates acetyl-CoA levels, which increases p65 acetylation and its transcriptional activity modulates inflammatory responses[51]. We add to this knowledge by defining p65 as a KAT2a-acetylation target. Contrary to a previous study showing that KAT2a participates in p65/RelA degradation independently of its acetyltransferase activity[52,53], and in line with the previously reported interaction of KAT2a and p65 acetylation[37], we find that KAT2a activity is needed to activate NF-κB signaling in palmitate-rich environments.

Several roles of fatty acid oxidation have been described in metastasizing cancer cells[1,2]. CPT1a deletion inhibits mammosphere formation of luminal cells[54] and a splice variant of CPT1a promotes histone deacetylase activity through a protein–protein interaction[55]. Moreover, ATP levels sustained by CPT1a activity activate Src through autophosphorylation[56]. Beyond breast cancer, matrix-detached colorectal and ovarian cancer cells accumulate reactive oxygen species upon CPT1a silencing[57] and oxidize oleate to sustain mitochondrial respiration[58], respectively. Similarly, oleate-enriched lymph node metastases from melanoma rely on fatty acid oxidation[59]. We complement these various functions of fatty acid oxidation by showing that palmitate oxidation is important for p65 acetylation. Moreover, we show that CPT1a silencing is sufficient to target metastasis formation in lean and HFD-fed mice, with the latter not previously shown in vivo. This may suggest that the use of the CPT1a inhibitor etomoxir should be revisited in obese patients with breast cancer.

To date, very little is known about the nutrient priming of the pre-metastatic niche by the primary tumor's secretome with only one report highlighting spared glucose consumption through the induction of a hypometabolism of resident cells[7]. We discover that palmitate availability is selectively increased in pre-metastatic lungs because palmitate is actively secreted by lung-resident AT2 cells in response to tumor-secreted factors, while HFD alters the lung and liver environment by increasing the availability of several fatty acids in the interstitial fluid, which may be reflective of the systemic increase that was observed in circulation[22]. Obesity is known to promote breast cancer progression through leptin and insulin signaling[60]. Adding to this, we show that HFD increases lung interstitial fatty acid availability even though lungs are not considered steatotic organs. Therefore, this suggests a much broader impact of diet on nutrient availability than previously considered and highlights an underappreciated role of nutrient priming of distant organs during metastasis formation.

Methods

Cell culture

MCF10A (ER$^-$/PR$^-$/HER2$^-$), MCF7 (ER$^+$/PR$^+$/HER2$^-$) and 4T1 (ER$^-$/PR$^-$/HER2$^-$) cell lines were purchased from American Type Culture Collection. The EMT6.5 (ER$^-$/PR$^-$/HER2$^-$) cell line was provided by R. Anderson, EO771-Met clone (ER$^{-/+}$/PR$^-$/HER2$^-$) by Prof. Mazzone and 4T07 (ER$^-$/PR$^-$/HER2$^-$) cell line by Prof. Gomes. MCF10A cells expressing the oncogenic driver H-Ras^{V12} (MCF10A H-Ras^{V12}) were generated as previously described[18] as a relevant in vitro model for breast cancer[61] and metastasis biology[18,19,62,63]. The 4T1, 4T07 and EMT6.5 cells were grown in Roswell Park Memorial Institute (RPMI) 1640 medium and MCF7 in DMEM, both supplemented with 10% FBS, 1% penicillin (50 U ml^{-1}) and 1% streptomycin (50 µg ml^{-1}). MCF10A H-RAS^{V12} cells were cultured in DMEM/F12 supplemented with 5% horse serum, 1% penicillin (50 U ml^{-1}), 1% streptomycin (50 µg ml^{-1}), 0.5 µg ml^{-1} hydrocortisone, 100 ng ml^{-1} cholera toxin, 10 µg ml^{-1} insulin and 20 ng ml^{-1} recombinant human EGF. All cells were maintained at 37 °C, 5% CO_2 and 95% relative humidity and regularly tested negative for *Mycoplasma* infection using a Mycoalert detection kit (Lonza). For 3D growth conditions, plates were covered with soft agar mixed 1:1 with culture medium as described[18]. Cells were plated on top of the base agar and incubated for 3–5 d. The following compounds were used: etomoxir (50 µm, Cayman); KAT2a specific inhibitor CPTH2 (ref. [38]) (2 µm, Cayman); ACLY inhibitor BMS-303141 (20 µm, MedChemExpress); TNF-α (10 ng µl^{-1}, Sigma-Aldrich); NF-κB inhibitor and ammonium PDTC (0.5 µm Merck); sodium acetate (5 mM, Sigma-Aldrich); free fatty acids sodium palmitate, stearic acid, oleic acid and octanoic acid (Sigma-Aldrich), coupled to BSA as described previously[64] and supplemented in addition to FBS to provide a final concentration of 130 µm.

Cell proliferation assays

Growth was assessed based on cell number and cell confluency (2D) or spheroid size (3D). Specifically, growth rates were calculated by measuring confluency every 4 h using an Incucyte live-cell imager (Essen Biosciences) over 96 h in 2D cultures. To measure 3D growth, spheroids were cultured in six-well plates upon specified conditions for 5 d and representative pictures of each well were taken using Motic Images Plus 2.0 software (Motic). Spheroid area was analyzed using Image Studio Lite 5.2 with at least five representative pictures per experimental condition.

Generation of shRNA knockdown/CRISPR knockout cell lines

CPT1a knockdown cell lines were generated using the short hairpin RNA (shRNA)-expressing lentiviral pLKO-shRNA2 vector (no. PT4052-5; Clontech), with a puromycin selection cassette, kindly provided by P. Carmeliet. Two non-overlapping oligonucleotide sequences

per species (human and mouse) and a nonsense scrambled shRNA sequence as a negative control were used (oligonucleotide sequences are available upon request). Lentiviral particles were produced in HEK293 cells. Transduction of cells was performed overnight and the medium was replaced the next day. Polyclonal cells were selected for 1 week with puromycin, 1 µg ml^{-1} for MCF10A H-Ras^{V12}, MCF7 and EMT6.5 and 2 µg ml^{-1} for 4T1 cells. shRNA-based silencing was confirmed by qPCR (Extended Data Fig. 9a). Murine *Cpt1a* and *Kat2a* knockout cell lines were generated by first establishing parental cell lines with doxycycline-inducible Cas9 expression using the Dharmacon Edit-R Inducible Lentiviral Cas9 vector (Horizon Discovery). Complementary single-guide RNA (sgRNA) oligonucleotides targeting two different exons of either *Cpt1a* (sgRNA1 (CACATTGTCGTGTACCACAG) and *Cpt1a* sgRNA2 (ACGTTGGACGAATCGGAACA)), *Kat2a* (sgRNA1 (GCTTCGGC-CAAACACGTGGG) and *Kat2a* sgRNA2 (GCTCGCCTGGAAGAACGGCG)) and and non-targeting sgRNA against EGFP (GAGCTGGACGGCGACG-TAAA) were designed and cloned into the LentiGuide Puro sgRNA expression vector (Addgene plasmid 52963) and delivered to cells via lentiviral infection. Cas9 expression was induced using doxycycline (2 µg ml^{-1}) for 7 d after which gene knockout was verified by western blot (Extended Data Fig. 9b).

Gene expression analysis by quantitative PCR

Total RNA from frozen tissues or cell lines was isolated using TRIzol Reagent (Thermo Scientific) and complementary DNA synthesis was performed using qScript cDNA Synthesis kit (Quanta) according to the manufacturer's protocols. Then, 50 ng of cDNA per reaction was amplified at 95 °C for 10 min, followed by 40 cycles of 15 s at 95 °C and 1 min at 60 °C using SYBER Green PCR Master Mix (Life Technologies) in the 7500HT system (Applied Biosystems). The mRNA expression was normalized to an endogenous housekeeping gene and relative expression was analyzed using the $2^{-\Delta\Delta Ct}$ method. Gene-specific primers were designed using Primer3 or obtained from Origene (Supplementary Table 5).

Protein extraction and western blot analysis

Spheroids were collected by centrifugation and lysed in RIPA buffer (Thermo Scientific) supplemented with protease (Roche) and phosphatase (PhosSTOP, Sigma) inhibitors. Tissues were ground before RIPA incubation. For nuclear protein isolation, samples were prepared as described previously[65]. Protein levels were measured using a Pierce BCA protein assay kit or Bradford Assay (Thermo Scientific). Then, 30–40 µg of protein was loaded on a NuPAGE 4–12% denaturing Bis-Tris gel and transferred to a nitrocellulose membrane (Thermo Scientific). After blocking in 5% milk in Tris Buffer Saline 0.05% Tween for 1 h, membranes were incubated overnight at 4 °C with primary antibodies: CPT1a (Abcam, ab234111; 1:1,000 dilution), GCN5L2/KAT2A (C26A10) (Cell Signaling, 3305T; 1:1,000 dilution), NF-κB p65 (acetyl K310) (Abcam, ab19870; 1:1,000 dilution), NF-κB p65 (D14E12) (Cell Signaling, 8242S; 1:1,000 dilution), β-actin (Sigma, A5441; 1:10,000 dilution) or histone H3 (Abcam, ab1791; 1:2,000 dilution). For NF-κB p65ac analysis, total levels of NF-κB were assessed in parallel samples run in the same gel prepared from the same master mix. After, membranes were incubated with mouse (Cell Signaling Technology, 7076; 1:4,000 dilution) or rabbit (Cell Signaling Technology, 7074; 1:4,000 dilution) HRP-linked secondary antibodies and visualized using Pierce ECL reagent (Thermo Scientific). Images were acquired using an ImageQuant LAS 4000 (GE Healthcare).

Electrophoretic mobility shift assays

Whole extracts from 3D spheroids were prepared and analyzed for DNA-binding activity using the HIV-LTR tandem κB oligonucleotide as a κB probe as described previously[66]. Whole-cell extracts were used to analyze NF-κB DNA-binding status by EMSA as previously validated[67].

Mitochondrial mass

3D spheroids were collected and dissociated using trypsin. Single cells were washed once with PBS and stained with MitoTracker Deep Red (M22426, Invitrogen) for 30 min at 37 °C. Cells were washed in PBS and analyzed by flow cytometry. Data analysis was performed using FlowJo software.

Mass spectrometry analysis

In 3D spheroids, quenching and metabolites extraction procedures were applied as described previously[68]. To analyze 2D-cultured cells, cells in six-well plates were washed with blood bank saline and quenched by flash-freezing the plates in liquid nitrogen. Metabolites from quenched samples were extracted as described previously[69,70].

Metabolite abundances were analyzed by either gas chromatography (GC) or liquid chromatography (LC) tandem mass spectrometry (MS/MS). For FA measurements, the lipid fraction (chloroform phase) was esterified as described previously[71] and separated with GC (8860 or 7890A GC system, Agilent Technologies) combined with MS (5977B or 5975C Inert MS system, Agilent Technologies). Then, 1 µl was injected in splitless mode with a split ratio of 1–3 or 1–9 with an inlet temperature of 270 °C on a DB-FASTFAME column (30 m × 0.250 mm). Helium was used as a carrier gas with a flow rate of 1 ml min^{-1}. The initial gradient temperature was set at 50 °C for 1 min and increased at the ramping rate of 12 °C min^{-1} to 180 °C, followed by a ramping rate of 1 °C min^{-1} to reach 200 °C for 1 min. The final gradient temperature was set at 230 °C with a ramping rate of 5 °C min^{-1} for 2 min and the temperatures of the quadrupole and the source at 150 °C and 230 °C, respectively. The MS system was operated under electron impact ionization at 70 eV (100–600 AMU mass range). For acetyl-CoA and polar metabolites measurements, methanol phase was resuspended in 50 µl water and analyzed in a Dionex UltiMate 3000 LC System with a thermal autosampler set at 4 °C, coupled to a Q-Exactive Orbitrap MS (Thermo Scientific). Then, 10 µl of sample were injected on a C18 column (Acquity UPLC HSS T3, 1.8 µm, 2.1 × 100 mm). The separation of metabolites was achieved at 40 °C with a flow rate of 0.25 ml min^{-1}. A gradient was applied for 40 min (A, 10 mM tributyl-amine and 15 mM acetic acid; B, methanol) to separate the targeted metabolites (0 min at 0% B, 2 min at 0% B, 7 min at 37% B, 14 min at 41% B, 26 min at 100% B, 30 min at 100% B, 31 min at 0% B; and 40 min at 0% B. The MS operated in negative full-scan mode (m/z range 70–500 and 190–300 from 5–25 min) using a spray voltage of 4.9 kV, capillary temperature of 320 °C, sheath gas at 50.0 and auxiliary gas at 10.0. Data were collected using the Xcalibur software (Thermo Scientific). For the detection of metabolites by LC–MS/MS, a 1290 Infinity II with a thermal autosampler set at 4 °C, coupled to a 6470 triple quadrupole (Agilent Technologies) was used. Samples were resuspended in 80% methanol:water and a volume of 4 µl was injected on a SeQuant ZIC/pHILIC Polymeric column (Merck Millipore). The separation of metabolites was achieved at 25 °C with a flow rate of 0.20 ml min^{-1}. A gradient was applied for 22 min (A, 10 mM ammonium acetate (pH 9.3); B, acetonitrile) to separate the targeted metabolites (0 min at 10% A, 2 min at 10% A, 13 min at 30% A, 13.1 min at 70% A, 17 min at 75% A, 18 min at 10% A and 22 min at 10% A). The temperature of the gas and the sheath gas were set at 270 °C (flow of 10 l min^{-1}) and 300 °C (flow of 12 l min^{-1}), respectively. Metabolite abundances were calculated from the raw chromatograms. For relative abundance, total ion counts were normalized to an internal standard (and the protein content for cell extracts. To calculate FA concentration, a standard curve for each metabolite was extracted and analyzed in parallel.

^{13}C-metabolite labeling

Cells were cultured using 11 mM $^{13}C_6$-glucose (Cambridge Isotope Laboratories) dissolved in RPMI (11879-020, Thermo Fisher) + 10% dialyzed FBS. After 5 d, quenching and metabolite extraction were performed as described above. Metabolite abundances and ^{13}C-labeling patterns were analyzed by GC–MS. Mass distribution vectors were

extracted from the raw ion chromatograms using MATLAB, corrected for naturally occurring isotopes using the method of Fernandez et al.[72] and fractional contribution of carbon was calculated as described by Buescher et al.[73]. Palmitate uptake was calculated using the labeled substrate $^{13}C_{16}$-palmitic acid (Sigma-Aldrich) and measuring the difference in labeled palmitate in medium after 5 d corrected by total protein content of each analyzed well. Fractional de novo synthesis of FAs was calculated using isotopomer spectral analysis during the exposure to the labeled substrate $^{13}C_6$-glucose for 5 d.

Histone extraction and SILAC analysis

3D spheroids were collected after 5 d and core histone proteins were isolated by the acid extraction procedure previously described[74]. The 4T1 cells cultured in SILAC DMEM (Silantes) supplemented with 84 mg l^{-1} 13C615N4 L-arginine and 175 mg l^{-1} 13C615N2 L-lysine (Cambridge Isotope Laboratories) were used as a histone internal standard (2:1 ratio). Histones were digested in 50 mM ammonium bicarbonate using Arg-C (Promega) and the resulting peptides desalted by C18 StageTip[75],resuspended in 1% TFA, 0.2% formic acid buffer and injected on an EASY-nLC (Thermo Scientific) coupled online to an MS. Peptides were separated on a 20-cm fused silica emitter (New Objective) packed in-house with reverse-phase Reprosil Pur Basic 1.9 µm (Dr. Maisch), eluted with a flow of 300 nl min^{-1} from 5% to 30% of buffer B (80% acetonitrile and 0.1% formic acid) in a 60-min linear gradient and injected into an Orbitrap Fusion Lumos (Thermo Scientific) via electrospray ionization. MS data were acquired using Xcalibur software (Thermo Scientific) and processed with MaxQuant software (v.1.6.6.3). Multiplicity was set to 2 and FDRs at the protein and peptide level to 1%. Perseus (v.1.6.2.2) was used for downstream analysis. To ensure unambiguous identification, only proteins identified with at least one unique peptide were considered. Each acetylation site was normalized by total histone abundance.

ChIP-seq analysis

Changes in genome-wide DNA-binding sites were analyzed using a ChIPmentation protocol followed by sequencing as described previously[76]). Chromatin was fragmented to 100–300 bp using 25 cycles (30 s on, 30 s off and 20% amplitude) using Qsonica Q800R. ChIP was performed overnight using H3K9ac antibody (Cell Signaling, 9649S, 1:50 dilution) conjugated to magnetic protein A/G beads (Millipore). *Drosophila melanogaster* chromatin was spiked-in (50 ng, Active Motif, 53083). Next, tagmentation (Nextera DNA Sample Preparation kit, Illumina) and library preparation was performed. Purified DNA (Agencourt AMPure Beads, Beckman) was sequenced on an Illumina Hiseq 4000 platform. Raw sequencing reads were cleaned with fastq-mcf and a quality control was performed with FastQC. Cleaned reads were then aligned to the mm10 genome using BWA and duplicates were removed with Picard (v.1.130). deepTools (v.1.6) was used to plot heat maps of signals centered around transcription start sites as well as to plot Spearman correlation of ChIP-seq signal per gene between conditions.

In vitro invasion assay

A total of 50,000 cells were embedded in a 50:50 mix of growth factor-reduced Matrigel (BD Biosciences) and collagen I (Life Technologies) and seeded onto 35-mm glass-bottom culture dishes (MatTek). Cells were allowed to invade for 72 h and then stained with calcein green (Life Technologies) for 1 h, washed with PBS and immediately imaged. Imaging was performed on a Leica TCS SP8 X confocal microscope and quantification of invasive area on the maximum projection images using FIJI v.2.3.1 distribution of ImageJ v.2.3.0.

In vivo mouse experiments

All animal experiments complied with ethical regulations and were approved by the Institutional Animal Care and Research Advisory Committee of KU Leuven (ECD nos. P007/2020, P048/2020 and ECD P025/2020). All mice were housed under a regimen of 12 h light–12 h dark in non-SPF (conventional) conditions with a constant supply of food and water. Sample size was determined using power calculations with $B = 0.8$ and $P < 0.05$ based on preliminary data and in compliance with the 3R system. For lung metastasis experiments, 6–8-week-old female Balb/cAnNCrlCrlj and BALB/cOlaHsd mice were inoculated with 4T1 or EMT6.5 cells either in the m.f. (1×10^6 cells) or i.v. (1×10^5 cells). For EO771 cells, 6–8-week-old female C57BL/6JAX mice were used to i.v. inject 1×10^5 cells. Mice were killed after 21 d (m.f.) or 13 d (i.v.) using ketamine–xylene or Dolethal. For injections performed after lung pre-conditioning with TCM, 4T1 and 4T07 cells were injected i.v. (2.5×10^4 cells) and mice were killed after 16 d. For etomoxir treatment after cancer cell seeding in the lung, 1×10^5 cells were injected i.v. and after 4 d, i.p. injections of etomoxir (40 mg kg^{-1} per day) or vehicle (water) were performed daily and mice were killed after 10 d. For acute etomoxir treatment, 1×10^6 4T1 cells were injected into the m.f. and when tumors were about 13 mm, mice were randomized into two groups for daily i.p. injections for 3 d. For metabolomics, mice were killed using Dolethal and tumor tissues were immediately frozen using a liquid-nitrogen-cooled Biosqueezer (Biospec Products). Tumor volumes were measured during every experiment using a caliper and weighed at the end of the experiment. Mice were monitored for detection of humane end points, which were determined using a scoring sheet as follows: tumor size of 1.8 cm^3, loss of ability to ambulate, labored respiration, surgical infection or weight loss over 10% of initial body weight. For all experiments, the maximum permitted tumor volume was 1.8 cm^3 and this limit was not exceeded in any experiment.

For HFD experiments, 4-week-old female BALB/c mice were randomized into two groups: CD (E15742-33 ssniff Spezialdiäten) or long-chain HFD (S8655-E220 sniff Spezialdiäten). The energy balance between fat (from lard):protein:carbohydrates was 13:27:60% and 60:20:20% for CD and HFD, respectively. Mice were maintained on these diets for 16 weeks before the experiments were performed. Body weight was monitored biweekly and mice were inspected weekly for welfare assessment. For lung metastasis experiments, 1×10^5 cells were injected i.v. and mice were killed 11 d after. For liver metastasis experiments, 1×10^5 cells were delivered via the splenic vein and mice were killed 17 d after.

The lung and liver interstitial fluid extraction

The interstitial fluid extraction method was adapted and performed as described previously[8,9]. For human samples, healthy lung tissue was collected from patients who underwent lung surgery for emphysematous lung volume reduction or tumorectomy (taken as far away as possible from the tumor front). For mice samples, 6–8 BALB/c female mice were killed with 50 µl of 60 mg ml^{-1} of Dolethal and subsequently, the liver and lung were collected by surgical resection. Tissues were washed with a blood bank saline solution, dried from liquid excess and placed in a homemade filtered centrifuge tube with a nylon mesh filter with 20-µm opening pores (Repligen). The interstitial fluid (between 1–5 µl for each organ) was collected by centrifugation (400*g*, 4 °C for 10 min) and stored on dry ice immediately after extraction. The volume of interstitial fluid was used to determine the concentration of the different metabolites measured by MS.

Tumor condition medium generation and in vivo pre-metastatic niche formation

The procedure to induce pre-metastatic niche formation in the lung was adapted from elsewhere[12]. In brief, primary tumors generated from 4T1 cells were cut into small pieces and cultured at 37 °C in 15 ml g^{-1} of tumor of DMEM (no FBS) + 1% penicillin and 1% streptomycin. The same medium without tumor was incubated in parallel to generate CM. After 72 h, medium was transferred to a 70-µm cell strainer and spun down for 10 min at 1,000*g*. Supernatants from three different tumors were pooled together to cover the variability between tumors. HEPES

(20 mM) was added to the medium and this was filtered and stored at 4 °C no more than 2 weeks after collection. At 7–8 weeks old BALB/c mice were injected i.v. with 200 µl of either CM or TCM three times per week for 3 weeks.

Hematoxylin and eosin staining of tumor sections

H&E staining of pulmonary metastases was performed as previously described[19]. Scanned slides were analyzed for metastatic area and the number of metastases using ZEN blue software. Metastatic burden was determined by analyzing the number of metastases, metastatic area and metastatic index (metastatic area divided by the primary tumor weight). All samples were analyzed blinded.

MALDI–MSI molecular imaging

The 4T1 cells were injected i.v. into healthy 6–8-week-old female BALB/c mice. After 13 d, lung tissue was embedded in 3% carboxymethylcellulose (CMC), snap frozen in a cryomold dipped in liquid-nitrogen-cooled isopentane (Sigma-Aldrich) and stored at −80 °C. Tissue was sectioned (10 µm) using a Microm HM525 NX cryostat (Thermo Scientific), thaw-mounted onto conductive IntelliSlides (Bruker) and dried in a vacuum desiccator at room temperature for 30 min. For matrix coating, 7 mg ml^{-1} norharmane in 2:1 chloroform and methanol (v/v) was applied onto slides using an HTX M5-SprayerTM (HTX technologies) at a flow rate of 0.125 ml min^{-1}, spray nozzle temperature of 30 °C and spray nozzle velocity of 1,350 mm min^{-1}. MALDI–MSI was performed on a timsTOF fleX MALDI-2 MS (Bruker) in positive mode (m/z range 250–1,800), using a 50 × 50-µm raster size with 300 laser shots per pixel at a laser frequency of 10 kHz. Images were acquired using FlexImaging 7.0 software (Bruker). For m/z of interest, on-tissue MS/MS fragmentation spectra were acquired in positive ion mode using a precursor ion isolation width of 1 Da and collision energy of 35 eV. Data were analyzed using SCiLS Lab 2023a (Bruker) with a mass accuracy of ±10 ppm, without denoising and applying root mean square normalization. Spectral data and regions of interest were exported to MetaboScape 2021a (Bruker). The bucket table was annotated with the Metaboscape build-in lipid annotation tool and a list of lipids obtained from MS-DIAL's LipidBlast database was used for this purpose. MS/MS spectra are shown in Extended Data Fig. 10. After MSI analysis, the matrix was removed by submerging the slide in 100% methanol for 30 s and the tissue was stained with H&E. For the metastatic cluster, annotations for m/z of interest were manually verified against the LipidMaps database based on mass accuracy (<10 ppm) and characteristic ions observed in the fragmentation spectra (Bruker Compass DataAnalysis v.6.0).

Lung dissociation and flow cytometry analysis of cancer cell populations

Before injections, cancer cells were transfected with the mammalian expression lentiviral vector pLKO.3 Thy1.1 (Addgene plasmid 14749) containing the surface protein Thy1.1 as a reporter protein. FACS-sorted CD90.1-expressing 4T1 and EMT6.5 cells were injected i.v. into 6–8-week-old BALB/c mice. After 11 d, mice were anesthetized with ketamine (100 mg kg^{-1}) and xylazine (10 mg kg^{-1}) and lungs were perfused through the right ventricle[77]. Once lungs were extracted, the tissue was washed in blood bank saline, dried and minced using blades. Tissues were incubated with liberase (Roche) (0.3 mg ml^{-1}) and DNase1 (1 µg ml^{-1}) during 45 min at 37 °C with occasional vortexing, then quenched with 3% FBS:PBS + 2 mM EDTA and filtered through a 70-µm cell strainer. The cell pellet was washed, incubated with Red Blood Lysis buffer (Merck) and transferred through a 40-µm cell strainer. The single-cell suspension was counted and 30×10^6 cells per ml were preincubated with anti-mouse CD16/CD32 (Fc block, BD Biosciences) and stained for 20 min at 4 °C for flow cytometry analysis. Antibodies against CD45 (BD Bioscience, 550994, 1:250 dilution), PDPN (BioLegend, 127409, 1:250 dilution) and CD90.1 (BioLegend, 202505, 1:400 dilution) were used for selecting cancer cells from the single-cell suspensions of murine lung. To exclude dead cells, Viability efluor450 (Thermo Fisher, 65-0863-14, 1:500 dilution) was used. Single cells were analyzed using a BD FACSCanto II with FACSDiva (BD Biosciences). Metastatic burden was determined by assessing the fraction of CD90.1-positive cells in the lung.

Primary alveolar type II cell isolation by flow cytometry and 3D culture

For in vivo analysis, primary AT2 cells were isolated from control (healthy) or 4T1 and 4T07 tumor-bearing (primary tumor, day 17 after m.f. injection) BALB/c mice by flow cytometry sorting following the gating strategy previously reported[71]. Briefly, mice were anesthetized with ketamine (100 mg kg^{-1}) and xylazine (10 mg kg^{-1}) and lungs were perfused and dissociated as described above. Antibodies against CD45 (BD Bioscience, 550994, 1:200 dilution), CD31 (BD Bioscience, 562939, 1:200 dilution), CD49f (Thermo Scientific, 25-0495-82, 1:100 dilution), EpCAM (Thermo Scientific, 17-5791-82, 1:200 dilution), MHC-II (BioLegend, 107643, 1:100 dilution) and Viability efluor780 (Thermo Fisher, 65-0865-14, 1:800 dilution) were used. A minimum of 1.2×10^5 AT2 cells (purity ≥92%) were sorted using FACSAria Fusion (BD Biosciences) and placed directly in TRIzol Reagent (Thermo Scientific). RNA extraction, cDNA synthesis and gene expression analysis by qPCR were performed as described above.

For in vitro experiments, primary AT2 cells were isolated from CreER-induced lineage-tracing mice[78] performed at the Francis Crick Institute, in accordance with UK Home Office regulations under project license PPL80/2531. *Sftpc-CreERT2* mice were a gift from the J.-H. Lee laboratory. For type II cell lineage labeling, three doses of tamoxifen dissolved in Mazola corn oil were given to *Sftpc-CreERT2;R26R-YFP* female C57BL/6J mice (8–10 weeks old) via oral gavage over consecutive days (0.2 mg g^{-1} body weight). Lungs were collected 2 weeks after the final dose and dissociated as described above. Single-cell suspensions were incubated with mouse FcR Blocking Reagent (10 min at 4 °C) followed by incubation with CD45-BV421 (BioLegend 103133, clone 30-F11, 1:200 dilution) and Ter119-BV421 (BioLegend 116233, TER119, 1:200 dilution) for 30 min at 4 °C. Cells were washed twice with MACS buffer (0.5% BSA and 250 mM EDTA in PBS) and incubated with 4′,6-diamidino-2-phenylindole to discriminate dead cells. AT2 cells ($CD45^-Ter119^-YFP^+$) were sorted on a BD Influx cell sorter (BD Biosciences). Isolated AT2 cells were seeded at a density of 150,000 cells per well in a collagen-coated Alvetex Scaffold 12-well plate insert (ReproCELL). Collagen solution was made by 30 µg ml^{-1} PureCol collagen (Advanced Biomatrix), 0.1% BSA and 20 mM HEPES in HBSS. Then, 2 ml of control or tumor-conditioned MEM medium (DMEM/F12) with 0.5% FBS, 100 U ml^{-1} penicillin–streptomycin, 20 ng ml^{-1} EGF and 10 µg ml^{-1} insulin was added below the insert. After 72 h, medium was collected, centrifuged and filtered to remove any cellular debris and stored at −80 °C until further metabolomics analysis. For RNA extraction, scaffolds were washed and placed directly into QIAzol lysis reagent and incubated on a shaker at 100 r.p.m. for 15 min at room temperature. RNA was isolated using the RNeasy Mini kit (QIAGEN) and cDNA was synthesized using the SuperScript III First Strand Synthesis kit (Thermo Fisher Scientific) according to the manufacturer's protocol.

Single-cell RNA-seq, data pre-processing and cell-type assignment

Single-cell suspensions from the lungs of female BALB/c mice injected with CM or TCM for 3 weeks or of mice fed with CD or HFD for 16 weeks, were prepared as described above for lung dissociation. cDNA libraries were performed using the Chromium Single Cell 5′ V1.1 Library (10x Genomics) kit, following the manufacturer's guidelines (10,000 cells per library) and sequenced on a NovaSeq 6000 System (Illumina). The sequenced reads were mapped to the mouse genome (mm10

build GRCm38.p6) using the CellRanger software (10x Genomics) and analyzed within the R/Bioconductor framework. Specifically, the raw unique molecular identifier (UMI) count matrices were first imported and merged using Seurat[79] and then converted for further processing with Monocle[80]. Low-quality cells were filtered based on standard quality control metrics: mitochondrial RNA content (allowing for a maximum of 10% in CM/TCM or 20% in CD/HFD), library size (removing cells with total UMI counts <500) and number of detected genes (removing cells expressing <200 genes in CM/TCM or <250 in CD/HFD). Genes expressed in fewer than five cells were additionally ignored in all subsequent analyses. Size-factor and variance-stabilizing were applied to the filtered datasets and highly variable genes were identified based on their departure from the average normalized dispersion versus expression trend observed among all genes. The top 1,000 highly variable genes with size-factor-normalized expression levels >0.01 were selected. Principal-component analysis was performed on the size-factor-normalized and variance-stabilized count matrix restricted to these genes only, followed by 2D Uniform Manifold Approximation and Projection (UMAP) dimensional reduction[80] based on the resulting top 50 principal components. Cells were then clustered in the UMAP plane by applying the Louvain[80,81] graph-based algorithm at high resolution (resolution of 0.001 with $k_{NN} = 10$ for the CM/TCM and $k_{NN} = 15$ for CD/HFD), to attain a fine-grained cluster structure for each dataset (158 clusters for CM/TCM and 51 for CD/HFD). The resulting fine-grained clusters were manually annotated to specific cell types. For marker score analysis, cell-type marker scores were calculated using the GSVA (gene set variation analysis) package[82]. In brief, count matrices for the filtered datasets were first subject to size-factor and variance-stabilizing normalization. GSVA-based z scores were then determined, for every cell, for a manually assembled list of marker gene sets and further scaled to the range 0–1, by means of the following mapping:

$$X_{M,C} = \frac{Z_{M,C} - Z_{M,min}}{Z_{M,max} - Z_{M,min}}$$

where $X_{M,C}$ is the scaled (0–1) score for a given marker set, M and cell C, while $Z_{M,C}$ is the z score for that cell and marker set and $Z_{M,max}$ and $Z_{M,min}$ are, respectively, the highest and lowest values of $Z_{M,C}$ among all cells (for each marker set M).

Lipidomics analysis

The 7–8-week-old female BALB/c mice were inoculated with 4T1 cells in the m.f. (1×10^6 cells). After 23 d, primary tumors and lung metastases were collected, snap frozen and pulverized (Cryomill, Retsch) under liquid-nitrogen conditions. Lipids were extracted by mixing 700 µl in water, homogenizing (Precellys, Bertin) with 800 µl 1 N HCl:CH_3OH 1:8 (v/v), 900 µl $CHCl_3$, 200 mg ml^{-1} of the antioxidant 2,6-di-tert-butyl 4-methylphenol (Sigma-Aldrich) and SPLASH LIPIDOMIX Mass Spec Standard (330707, Avanti Polar Lipids). After vortexing and centrifugation, the lower organic fraction was collected and evaporated in a speedvac. Lipid species were analyzed by LC–ESI/MS/MS as previously described[22] on a Nexera X2 UHPLC system (Shimadzu) coupled with hybrid triple quadrupole/linear ion trap MS (6500þ QTRAP system; AB SCIEX). Peak integration was performed with the MultiQuant software (v.3.0.3). Lipid species signals were corrected for isotopic contributions calculated using Python Molmass v.2019.1.1 and quantified based on internal standard signals and adhering to the guidelines of the Lipidomics Standards Initiative (level 2 type quantification).

Patient selection and sample collection

An informed consent was obtained from all participants included in this study. For collection of human samples for interstitial fluid measurements, the study was approved by the local ethics committee (Medical Ethics Committee UZ/KU Leuven, protocol S57123) as described previously[15]. Briefly, human healthy lung tissue was collected from patients who underwent lung surgery for emphysematous lung volume reduction or tumorectomy (resection specimen was taken as far away as possible from the tumor front) (Supplementary Table 1).

UPTIDER program. Snap-frozen and/or fresh tissue samples from metastases as well as healthy tissues were obtained through the ethically approved UPTIDER program (UZ/KU Leuven Program for Postmortem Tissue Donation to Enhance Research; NCT04531696, S64410); patients with metastatic breast cancer who consent to participate undergo a rapid research autopsy in the first 12 h after death. For the experiments described in this paper, fresh samples were collected. Some were used for freshly isolated interstitial fluid as described above and others were snap frozen in liquid nitrogen. Proteins were extracted from snap-frozen tissues following the cell-fractionation and nuclear isolation protocol described above. CPT1a and KAT2a expression was assessed in the cytosolic and nuclear fraction, respectively. Clinicopathological information for every patient in the UPTIDER dataset is shown in Supplementary Table 2.

CHEMOREL program. Patients for the retrospective translational CHEMOREL study were selected from a clinicopathological database in which all patients with breast cancer, who were diagnosed and treated at the UZ Leuven Multidisciplinary Breast Center (Belgium), are documented (patient and tumor characteristics, therapy and follow-up information, including relapse and survival). From this database, a homogeneous cohort of newly diagnosed patients with primary luminal B-type breast cancer with grade 2/3, ER^+, $PR^{+/-}$ or $HER2^-$ tumors was selected, including (1) patients who remained disease-free for at least 6–10 years after initial therapy ($n = 43$); (2) patients developing distant metastasis within 5 years after initial therapy ($n = 44$); and (3) primary metastasized patients ($n = 14$). Groups were matched for patient age, tumor size and node status. Clinicopathological information for patients in the CHEMOREL dataset is shown in Supplementary Table 3.

RNA-seq analysis

Patient tumors. RNA was extracted from formalin-fixed, paraffin-embedded unstained tissue slides prepared from the leftovers of surgical resection specimens after standard pathological diagnostic procedures. RNA extraction was performed by using the HighPure FFPET RNA extraction kit (Roche). The RNA-seq workflow and subsequent bioinformatics were accomplished at the Laboratory of Translational Genetics (VIB-KU Leuven by D. Lambrechts). RNA libraries were created using the KAPA Stranded mRNA-seq Library preparation kit according to the manufacturer's instructions. The resulting libraries were sequenced on a HiSeq2500 or HiSEq 4000 (Illumina) using a V3 flowcell generating 1 × 50-bp reads, yielding reliable results for 43 and 14 patients from groups 1 and 2, respectively. Optical duplicates and adaptor sequences were removed from the raw sequencing reads before aligning to the transcriptome and the reference genome using TopHat v.2.0 (ref. [83]) and Bowtie v.2.0 (ref. [84]). Counts were assigned to genes using the HTSeq software package. Raw sequencing reads were mapped to the transcriptome; >25,000 different transcripts were identified that could be detected in at least 50% of the samples. For the purpose of this study, the groups of primary metastasized patients ($n = 14$) (group 3) and patients who remained disease-free for at least 6–10 years after the initial therapy ($n = 43$) (group 1) were used for differential gene expression analysis.

2D and 3D spheroid cultured cells. RNA integrity and concentrations were measured on an Agilent Bioanalyze system and libraries were prepared using a KAPA Stranded mRNA Sequencing kit (Roche) according to the manufacturer's instructions. The resulting libraries were sequenced on a HiSeq 4000 (Illumina) using a flowcell generating 1 × 50-bp single-end reads. Reads were cleaned with the fastq-mcf software, after a quality control was performed

with FastQC (v.0.11.9). High-quality reads were then mapped to the *Mus musculus* reference genome (GRCm38/mm10) with HISAT2 (v.2.1.0) and the abundance of reads per gene was determined with HTSeq-count. Differential gene expression analysis was performed with the R package DESeq2 (v.1.22.0). Genes were ranked according to the score-sign($\log_2$FC) × log(*P*adj) and used as input for GSEA (Broad Institute). All pathways with a GSEA FDR < 0.05 were considered as significant. Pathway comparison and upstream regulator analysis were conducted in ingenuity pathway analysis (QIAGEN). The threshold criteria of $P \leq 0.05$ and a fold change of ≥0.5 in gene expression among the different pairwise comparisons were used.

In silico gene expression analysis and pathway analysis

Transcript mRNA expression data were collected from patients with primary breast cancer from The Cancer Genome Atlas (TCGA) ($n = 1{,}221$) and METABRIC ($n = 1{,}904$). Publicly available datasets were downloaded from TCGA portal (http://tumorsurvival.org/download.html) and cBioportal (https://www.cbioportal.org/datasets). All patients with mRNA-seq and clinical data were included. Clinical parameters, including survival information, tumor stage and tumor subtype, were acquired from TCGA's Clinical Data Resource dataset (https://gdc.cancer.gov/about-data/publications/PanCan-Clinical-2018) and are shown in Supplementary Table 4. We used TNM staging according to the AJCC Cancer Staging Manual, 7th edition, to maintain consistency for all patients from TCGA and METABRIC datasets. For statistical analysis, the Kaplan–Meier method was used to analyze the relationship between gene expression (CPT1A-low and CPT1A-high, median as cutoff) and survival prognosis. Univariate and multivariate Cox regressions were used to analyze the associations between patient clinical information (age, TNM stage and tumor subtype (classified by PAM50)) and overall survival. R software (v.4.0.5) was used to perform Kaplan–Meier survival analysis, univariate and multivariate Cox regressions by using a *P* value <0.05 as the filter value.

The expression levels of *CPT1A* in human tissues were analyzed in the Genevestigator database, using the HS00002-(33) public microarray and RNA-seq study results[85]. Expression values are shown as fold change of normalized expression values calculated by Genevestigator using standard normalization methods for different microarray platforms.

To compare gene expression profiles from breast cancer metastases at different organ sites, the dataset GSE14018 was downloaded from GEO[86]. GSEA was performed using the NF-κB-related transcriptional signature HALLMARK_TNFA_SIGNALING_VIA_NFKB from the MsigDB[87].

Statistics and reproducibility

Statistical data analysis was performed using GraphPad Prism v.8 (GraphPad Software) on $n \geq 3$ biological replicates. Data are presented as mean ± s.e.m. Details of statistical tests and post-tests are presented in figure legends. *P* values $<10^{-15}$ are indicated as $P < 0.0001$. Determination of mathematical outliers was performed using the ROUT method of regression (GraphPad) with coefficient $Q = 1\%$. Animals were excluded only if they died or had to be killed according to ethical protocols. For in vitro experiments, no data were excluded. For in vivo experiments, sample size was determined using power calculations with $\beta = 0.8$ and $P < 0.05$, based on preliminary data. Sample size for all in vitro experiments was chosen empirically or based on previous similar studies that have given statistically significant results. For in vivo experiments, mice were randomized before diet feeding, TCM/CM injections or injection with the different cell lines. In addition, mice were given a unique number before data collection for blinding analysis. For in vitro studies, samples were randomized, when possible, before data acquisition.

Resource availability

This study did not generate new reagents, except for genetically manipulated cell lines based on commercially available constructs. Reagents generated in this study will be made available on request through the lead author or the collaboration partner that generated the resource, but we may require payment and/or a completed Materials Transfer Agreement if there is potential for commercial application. Further requests for resources should be directed to the corresponding author S.-M.F.

Reporting summary

Further information on research design is available in the Nature Portfolio Reporting Summary linked to this article.

Data availability

Mouse scRNA-seq, RNA-seq and ChIP-seq data generated in this study have been deposited in the GEO under accession code GSE196993. The human expression data from patients with primary breast cancer from the publicly available TCGA Research Network and METABRIC are available in TCGA (http://tumorsurvival.org/download.html) and cBioportal (https://www.cbioportal.org/datasets). The dataset for gene expression from breast cancer metastases at different organ sites was downloaded from GEO under accession code GSE14018. Source data and gel source images are provided with this paper. All other data supporting the findings of this study are available within the Article and the Supplementary Information and from the corresponding author on reasonable request. Source data are provided with this paper.

References

1. Bergers, G. & Fendt, S. M. The metabolism of cancer cells during metastasis. *Nat. Rev. Cancer* **21**, 162–180 (2021).
2. Martin-Perez, M., Urdiroz-Urricelqui, U., Bigas, C. & Benitah, S. A. The role of lipids in cancer progression and metastasis. *Cell Metab.* **34**, 1675–1699 (2022).
3. Broadfield, L. A., Pane, A. A., Talebi, A., Swinnen, J. V. & Fendt, S. M. Lipid metabolism in cancer: new perspectives and emerging mechanisms. *Dev. Cell* **56**, 1363–1393 (2021).
4. Altea-Manzano, P., Cuadros, A. M., Broadfield, L. A. & Fendt, S. M. Nutrient metabolism and cancer in the in vivo context: a metabolic game of give and take. *EMBO Rep.* **21**, e50635 (2020).
5. Peinado, H. et al. Pre-metastatic niches: organ-specific homes for metastases. *Nat. Rev. Cancer* **17**, 302–317 (2017).
6. Doglioni, G., Parik, S. & Fendt, S. M. Interactions in the (pre) metastatic niche support metastasis formation. *Front. Oncol.* **9**, 219 (2019).
7. Fong, M. Y. et al. Breast-cancer-secreted miR-122 reprograms glucose metabolism in premetastatic niche to promote metastasis. *Nat. Cell Biol.* **17**, 183–194 (2015).
8. Christen, S. et al. Breast cancer-derived lung metastasis show increased pyruvate carboxylase-dependent anaplerosis. *Cell Rep.* **17**, 837–848 (2016).
9. Rinaldi, G. et al. In vivo evidence for serine biosynthesis-defined sensitivity of lung metastasis, but not of primary breast tumors, to mTORC1 inhibition. *Mol. Cell* **81**, 386–397 (2021).
10. Heppner, G., Miller, F. & Malathy Shekhar, P. V. Nontransgenic models of breast cancer. *Breast Cancer Res.* **2**, 331–334 (2000).
11. Lee, E., Pandey, N. B. & Popel, A. S. Pre-treatment of mice with tumor-conditioned media accelerates metastasis to lymph nodes and lungs: a new spontaneous breast cancer metastasis model. *Clin. Exp. Metastasis* **31**, 67–79 (2014).
12. Erler, J. T. et al. Hypoxia-Induced lysyl oxidase is a critical mediator of bone marrow cell recruitment to form the premetastatic niche. *Cancer Cell* **15**, 35–44 (2009).
13. Sceneay, J. et al. Primary tumor hypoxia recruits CD11b+/Ly6Cmed/Ly6G+ immune suppressor cells and compromises NK cell cytotoxicity in the premetastatic niche. *Cancer Res.* **72**, 3906 (2012).

14. Peinado, H. et al. Melanoma exosomes educate bone marrow progenitor cells toward a pro-metastatic phenotype through MET. *Nat. Med.* **18**, 883–891 (2012).
15. Agudelo, C. W., Samaha, G. & Garcia-Arcos, I. Alveolar lipids in pulmonary disease: a review. *Lipids Health Dis.* **19**, 122 (2020).
16. Ombrato, L. et al. Metastatic-niche labelling reveals parenchymal cells with stem features. *Nature* **572**, 603–608 (2019).
17. Hegab, A. E. et al. High-fat diet activates adult mouse lung stem cells and accelerates several aging-induced effects. *Stem Cell Res.* **33**, 25–35 (2018).
18. Elia, I. et al. Proline metabolism supports metastasis formation and could be inhibited to selectively target metastasizing cancer cells. *Nat. Commun.* **8**, 15267 (2017).
19. Elia, I. et al. Breast cancer cells rely on environmental pyruvate to shape the metastatic niche. *Nature* **568**, 117–121 (2019).
20. Lien, E. C. et al. Low glycaemic diets alter lipid metabolism to influence tumour growth. *Nature* **599**, 302–307 (2021).
21. Vivas-García, Y. et al. Lineage-restricted regulation of SCD and fatty acid saturation by MITF controls melanoma phenotypic plasticity. *Mol. Cell* **77**, 120–137 (2020).
22. Broadfield, L. A. et al. Fat induces glucose metabolism in nontransformed liver cells and promotes liver tumorigenesis. *Cancer Res.* **81**, 1988–2001 (2021).
23. Ciriello, G. et al. Comprehensive molecular portraits of invasive lobular breast cancer. *Cell* **163**, 506–519 (2015).
24. Curtis, C. et al. The genomic and transcriptomic architecture of 2,000 breast tumours reveals novel subgroups. *Nature* **486**, 346–352 (2012).
25. Kalucka, J. et al. Quiescent endothelial cells upregulate fatty acid β-oxidation for vasculoprotection via redox homeostasis. *Cell Metab.* **28**, 881–894 (2018).
26. Campbell, S. L. & Wellen, K. E. Metabolic signaling to the nucleus in cancer. *Mol. Cell* **71**, 398–408 (2018).
27. Choudhary, C., Weinert, B. T., Nishida, Y., Verdin, E. & Mann, M. The growing landscape of lysine acetylation links metabolism and cell signalling. *Nat. Rev. Mol. Cell Biol.* **15**, 536–550 (2014).
28. Krämer, A., Green, J., Pollard, J. Jr. & Tugendreich, S. Causal analysis approaches in ingenuity pathway analysis. *Bioinformatics* **30**, 523–530 (2014).
29. Huber, M. A. et al. NF-κB is essential for epithelial-mesenchymal transition and metastasis in a model of breast cancer progression. *J. Clin. Invest.* **114**, 569–581 (2004).
30. Pino, A. M. & Rodríguez, J. P. Is fatty acid composition of human bone marrow significant to bone health. *Bone* **118**, 53–61 (2019).
31. Ferraro, G. B. et al. Fatty acid synthesis is required for breast cancer brain metastasis. *Nat. Cancer* **2**, 414–428 (2021).
32. Parik, S. et al. GBM tumors are heterogeneous in their fatty acid metabolism and modulating fatty acid metabolism sensitizes cancer cells derived from recurring GBM tumors to temozolomide. *Front. Oncol.* https://doi.org/10.3389/fonc.2022.988872 (2022).
33. Calao, M., Burny, A., Quivy, V., Dekoninck, A. & Van Lint, C. A pervasive role of histone acetyltransferases and deacetylases in an NF-kB-signaling code. *Trends Biochem. Sci.* **33**, 339–349 (2008).
34. Qin, J. D. et al. Effect of ammonium pyrrolidine dithiocarbamate (PDTC) on NF-κB activation and CYP2E1 content of rats with immunological liver injury. *Pharm. Biol.* **52**, 1460–1466 (2014).
35. Haque, M. E. et al. The GCN5: its biological functions and therapeutic potentials. *Clin. Sci.* **135**, 231–257 (2021).
36. Bondy-Chorney, E., Denoncourt, A., Sai, Y. & Downey, M. Nonhistone targets of KAT2A and KAT2B implicated in cancer biology (1). *Biochem. Cell Biol.* **97**, 30–45 (2019).
37. Stilling, R. M. et al. K-lysine acetyltransferase 2a regulates a hippocampal gene expression network linked to memory formation. *EMBO J.* **33**, 1912–1927 (2014).
38. Chimenti, F. et al. A novel histone acetyltransferase inhibitor modulating Gcn5 network: cyclopentylidene-[4-(4′-chlorophenyl) thiazol-2-yl)hydrazone. J. Med. Chem. 52, 530–536 (2009).
39. Ubellacker, J.M. et al. Lymph protects metastasizing melanoma cells from ferroptosis. *Nature* **585**, 113–118 (2020).
40. Pascual, G. et al. Dietary palmitic acid promotes a prometastatic memory via Schwann cells. *Nature* **599**, 485–490 (2021).
41. Cacicedo, J. M., Yagihashi, N., Keaney, J. F. Jr., Ruderman, N. B. & Ido, Y. AMPK inhibits fatty acid-induced increases in NF-κB transactivation in cultured human umbilical vein endothelial cells. *Biochem. Biophys. Res. Commun.* **324**, 1204–1209 (2004).
42. Ajuwon, K. M. & Spurlock, M. E. Palmitate activates the NF-κB transcription factor and induces IL-6 and TNFα expression in 3T3-L1 adipocytes. *J. Nutr.* **135**, 1841–1846 (2005).
43. Laine, P. S. et al. Palmitic acid induces IP-10 expression in human macrophages via NF-κB activation. *Biochem. Biophys. Res. Commun.* **358**, 150–155 (2007).
44. Maloney, E. et al. Activation of NF-κB by palmitate in endothelial cells: a key role for NADPH oxidase-derived superoxide in response to TLR4 activation. *Arterioscler. Thromb. Vasc. Biol.* **29**, 1370–1375 (2009).
45. Khandekar, M. J., Cohen, P. & Spiegelman, B. M. Molecular mechanisms of cancer development in obesity. *Nat. Rev. Cancer* **11**, 886–895 (2011).
46. Wang, X. et al. Epigenetic silencing of miR-33b promotes peritoneal metastases of ovarian cancer by modulating the TAK1/FASN/CPT1A/NF-κB axis. *Cancers* **13**, 4795 (2021).
47. Rios Garcia, M. et al. Acetyl-CoA carboxylase 1-dependent protein acetylation controls breast cancer metastasis and recurrence. *Cell Metab.* **26**, 842–855 (2017).
48. Loo, S. Y. et al. Fatty acid oxidation is a druggable gateway regulating cellular plasticity for driving metastasis in breast cancer. *Sci. Adv.* **7**, eabh2443 (2021).
49. McDonnell, E. et al. Lipids reprogram metabolism to become a major carbon source for histone acetylation. *Cell Rep.* **17**, 1463–1472 (2016).
50. Lu, M. et al. ACOT12-dependent alteration of acetyl-CoA drives hepatocellular carcinoma metastasis by epigenetic induction of epithelial-mesenchymal transition. *Cell Metab.* **29**, 886–900 (2019).
51. Chen, Q. et al. Acetyl-CoA derived from hepatic mitochondrial fatty acid β-oxidation aggravates inflammation by enhancing p65 acetylation. *iScience* **24**, 103244 (2021).
52. Mao, X. et al. GCN5 is a required cofactor for a ubiquitin ligase that targets NF-κB/RelA. *Genes Dev.* **23**, 849–861 (2009).
53. Xiong, Y. et al. CPT1A regulates breast cancer-associated lymphangiogenesis via VEGF signaling. *Biomed. Pharmacother.* **106**, 1–7 (2018).
54. Jariwala, N. et al. CPT1A and fatty acid β-oxidation are essential for tumor cell growth and survival in hormone receptor-positive breast cancer. *NAR Cancer* **3**, zcab035 (2021).
55. Pucci, S. et al. Carnitine palmitoyl transferase-1A (CPT1A): a new tumor specific target in human breast cancer. *Oncotarget* **7**, 19982–19996 (2016).
56. Park, JunH. et al. Fatty acid oxidation-driven Src links mitochondrial energy reprogramming and oncogenic properties in triple-negative breast cancer. *Cell Rep.* **14**, 2154–2165 (2016).
57. Wang, Y. N. et al. CPT1A-mediated fatty acid oxidation promotes colorectal cancer cell metastasis by inhibiting anoikis. *Oncogene* **37**, 6025–6040 (2018).
58. Sawyer, B. T. et al. Targeting fatty acid oxidation to promote anoikis and inhibit ovarian cancer progression. *Mol. Cancer Res.* **18**, 1088 (2020).

59. Lee, C.-k et al. Tumor metastasis to lymph nodes requires YAP-dependent metabolic adaptation. *Science* **363**, 644 (2019).
60. Barone, I., Giordano, C., Bonofiglio, D., Andò, S. & Catalano, S. The weight of obesity in breast cancer progression and metastasis: clinical and molecular perspectives. *Semin. Cancer Biol.* **60**, 274–284 (2020).
61. von Lintig, F. C. et al. Ras activation in human breast cancer. *Breast Cancer Res. Treat.* **62**, 51–62 (2000).
62. Hoenerhoff, M. J. et al. BMI1 cooperates with H-RAS to induce an aggressive breast cancer phenotype with brain metastases. *Oncogene* **28**, 3022–3032 (2009).
63. Lock, R., Kenific, C. M., Leidal, A. M., Salas, E. & Debnath, J. Autophagy-dependent production of secreted factors facilitates oncogenic RAS-driven invasion. *Cancer Discov.* **4**, 466–479 (2014).
64. Leamy, A. K. et al. Enhanced synthesis of saturated phospholipids is associated with ER stress and lipotoxicity in palmitate-treated hepatic cells. *J. Lipid Res.* **55**, 1478–1488 (2014).
65. Czerkies, M. et al. Cell fate in antiviral response arises in the crosstalk of IRF, NF-κB and JAK/STAT pathways. *Nat. Commun.* **9**, 493 (2018).
66. Jacque, E., Tchenio, T., Piton, G., Romeo, P.-H. & Baud, V. RelA repression of RelB activity induces selective gene activation downstream of TNF receptors. *Proc. Natl Acad. Sci.* **102**, 14635–14640 (2005).
67. Eluard, B. et al. The alternative RelB NF-κB subunit is a novel critical player in diffuse large B-cell lymphoma. *Blood* **139**, 384–398 (2022).
68. van Gorsel, M., Elia, I. & Fendt, S.-M. 13C tracer analysis and metabolomics in 3D cultured cancer cells. *Methods Mol. Biol.* https://doi.org/10.1007/978-1-4939-8769-6_4 (2019).
69. Lorendeau, D. et al. Dual loss of succinate dehydrogenase (SDH) and complex I activity is necessary to recapitulate the metabolic phenotype of SDH mutant tumors. *Metab. Eng.* **43**, 187–197 (2017).
70. Vriens, K. et al. Evidence for an alternative fatty acid desaturation pathway increasing cancer plasticity. *Nature* **566**, 403–406 (2019).
71. Major, J. et al. Type I and III interferons disrupt lung epithelial repair during recovery from viral infection. *Science* **369**, 712–717 (2020).
72. Fernandez, C. A., Des Rosiers, C., Previs, S. F., David, F. & Brunengraber, H. Correction of 13C mass isotopomer distributions for natural stable isotope abundance. *J. Mass Spectrom.* **31**, 255–262 (1996).
73. Buescher, J. M. et al. A roadmap for interpreting 13C metabolite labeling patterns from cells. *Curr. Opin. Biotechnol.* **34**, 189–201 (2015).
74. Karch, K. R., Sidoli, S. & Garcia, B. A. Identification and quantification of histone PTMs using high-resolution mass spectrometry. *Methods Enzymol.* **574**, 3–29 (2016).
75. Rappsilber, J., Ishihama, Y. & Mann, M. Stop and go extraction tips for matrix-assisted laser desorption/ionization, nanoelectrospray, and LC/MS sample pretreatment in proteomics. *Anal. Chem.* **75**, 663–670 (2003).
76. Broux, M. et al. Suz12 inactivation cooperates with JAK3 mutant signaling in the development of T-cell acute lymphoblastic leukemia. *Blood* **134**, 1323–1336 (2019).
77. Sinha, M. & Lowell, C. A. Isolation of highly pure primary mouse alveolar epithelial type II cells by flow cytometric cell sorting. *Bio. Protoc.* **6**, e2013 (2016).
78. Barkauskas, C. E. et al. Type 2 alveolar cells are stem cells in adult lung. *J. Clin. Invest.* **123**, 3025–3036 (2013).
79. Butler, A., Hoffman, P., Smibert, P., Papalexi, E. & Satija, R. Integrating single-cell transcriptomic data across different conditions, technologies, and species. *Nat. Biotechnol.* **36**, 411–420 (2018).
80. Cao, J. et al. The single-cell transcriptional landscape of mammalian organogenesis. *Nature* **566**, 496–502 (2019).
81. Blondel, V. D., Guillaume, J.-L., Lambiotte, R. & Lefebvre, E. Fast unfolding of communities in large networks. *J. Stat. Mech.* **2008**, P10008 (2008).
82. Hänzelmann, S., Castelo, R. & Guinney, J. GSVA: gene set variation analysis for microarray and RNA-seq data. *BMC Bioinform.* **14**, 7 (2013).
83. Kim, D. et al. TopHat2: accurate alignment of transcriptomes in the presence of insertions, deletions and gene fusions. *Genome Biol.* **14**, R36 (2013).
84. Langmead, B. & Salzberg, S. L. Fast gapped-read alignment with Bowtie 2. *Nat. Methods* **9**, 357–359 (2012).
85. Hruz, T. et al. Genevestigator v3: a reference expression database for the meta-analysis of transcriptomes. *Adv. Bioinform.* https://doi.org/10.1155/2008/420747 (2008).
86. Xu, J. et al. 14-3-3ζ turns TGF-β's function from tumor suppressor to metastasis promoter in breast cancer by contextual changes of Smad partners from p53 to Gli2. *Cancer Cell* **27**, 177–192 (2015).
87. Liberzon, A. et al. The Molecular Signatures Database hallmark gene set collection. *Cell Syst.* **1**, 417–425 (2015).
88. Gui, J. et al. Activation of p38α stress-activated protein kinase drives the formation of the pre-metastatic niche in the lungs. *Nat. Cancer* **1**, 603–619 (2020).
89. Liu, Y. et al. Tumor exosomal RNAs promote lung pre-metastatic niche formation by activating alveolar epithelial tLR3 to recruit neutrophils. *Cancer Cell* **30**, 243–256 (2016).
90. Hiratsuka, S. et al. The S100A8–serum amyloid A3–TLR4 paracrine cascade establishes a pre-metastatic phase. *Nat. Cell Biol.* **10**, 1349–1355 (2008).
91. Morrissey, S. M. et al. Tumor-derived exosomes drive immunosuppressive macrophages in a pre-metastatic niche through glycolytic dominant metabolic reprogramming. *Cell Metab.* **33**, 2040–2058 (2021).
92. Hoshino, A. et al. Tumour exosome integrins determine organotropic metastasis. *Nature* **527**, 329–335 (2015).
93. Geiger, T. et al. Use of stable isotope labeling by amino acids in cell culture as a spike-in standard in quantitative proteomics. *Nat. Protoc.* **6**, 147–157 (2011).

Acknowledgements

We thank P. Carmeliet (VIB-KU Leuven) for providing shRNA against *Cpt1a*, D. Nittner (VIB Histology and Imaging Core) for histology services and J. Lamote (VIB FACS Core) for providing advice and expertise for flow cytometry experiments. We thank T. Killian and V. van Hoef (VIB Bioinformatics Core) for their help with the RNA-seq analysis and L. Tora for advice on ChIP-seq analysis. In addition, we thank S. El Kharraz and A. Farag for performing blinded analyses of several H&E staining experiments shown in this manuscript. We acknowledge all physicians from the Multidisciplinary Breast Center Leuven (especially P. Neven, A. Smeets, I. Nevelsteen and K. Punie) for their clinical contribution to the UPTIDER and/or CHEMOREL cohorts. The authors also acknowledge the patients who accepted to donate tissues postmortem in the context of the UPTIDER program, as well as the entire multidisciplinary UPTIDER team. Figure 7h was created with BioRender.com. In terms of funding, P.A.M. is supported by a Marie Sklodowska-Curie Actions individual fellowship and has received Beug Foundation funding. Y.L. has received a Chinese Scholarship Council fellowship. A.C. is a Boehringer Ingelheim PhD fellow. G.D., J.F.G., T.G. and F.R. are Research Foundation – Flanders (FWO) PhD and senior postdoctoral fellows. G.D. has previously received a Kom op tegen Kanker and J.F.G. a FWO junior fellowship. X.-Z.L. is an EMBO

fellow and has received funding from the Gilead Foundation. H.F.A. has received funding from Stiching Tegen Kanker and King Baudouin funds. V.B. received funding from Fondation Nelia et Amadeo Barletta, Switzerland, 12 Rounds contre le Cancer and Université de Paris. A.M. received doctoral funding from Fondation Nelia et Amadeo Barletta, Switzerland. E.N. and I.M. received Francis Crick Institute core funding from Cancer Research UK (CRUK) (FC001112), Medical Research Council (FC001112) and the Wellcome Trust (FC001112) and the European Research Council (ERC) CoG-2020-725492. X.L. is an EMBO postdoctoral fellow. O.M.-B. is supported by a 12T1217N project by FWO at the program under the Marie Sklodowska-Curie grant agreement no. 665501. G.F. is a recipient of a postdoctoral mandate of the University Hospitals Leuven (KOOR). M.M. was supported by an ERC Consolidator grant (ImmunoFit; no. 773208). S.Z. acknowledges funding from CRUK (A17196), Stand Up to Cancer campaign for CRUK (A29800) and Breast Cancer Now (2019AugPR1307). The laboratory of T.G.P.G. is supported by the Barbara and Wilfried Mohr Foundation. V.P. acknowledges funding from a Wallenberg Academy Fellowship (KAW 2016.0123), the Swedish Research Council (VR 2020-01480), the Ragnar Söderberg Foundation) and Karolinska Institutet (SciLifeLab and KI funds). Research of the laboratory of C.D. is supported by an ERC Consolidator grant (FATLAS, 101003153), by the Fondation Cancer Luxembourg (FC/2018/07), the Belgian Foundation Against Cancer (C/2020/1441, PhD grant to S.L.) and the Funds Nadine de Beauffort (PhD grants to K.V.B. and M.D.S.). The UPTIDER program is supported by a grant from the University Hospitals from Leuven (KOOR 2021), as well as a C1 grant (14/21/114) from KU Leuven. S.M.F. acknowledges funding from the ERC under Consolidator grant agreement no. 771486–MetaRegulation, FWO Projects (G0B4122N), Beug Foundation, Fonds Baillet Latour, KU Leuven FTBO/Internal Funding/CELSA, and Stichting tegen Kanker.

Author contributions

Conception and design was carried out by P.A.M., G.D. and S.-M.F. Development of methodology was carried out by P.A.M., G.D., A.C., M.P. and C.R.D. Acquisition of data (including providing animals, acquiring and managing patient samples and providing facilities) was conducted by P.A.M., G.D., Y.L., A.C., E.N., A.M., M.P., J.V.E., I.V., D.B., X.L., H.F.A., M.D., N.R., X.S., T.G., M.D.S., S.L., F.R., S.H., Y.L., Q.W., E.K., C.C.A., V.G., G.F., J.-C.M., D.L., M.M., V.P., S.R.Z., J.C., J.S., H.W., U.B.-D., V.B., C.D., T.G.P.G. and I.M. Analysis and interpretation of data (for example, statistical analysis, biostatistics and computational analysis) was conducted by P.A.M., J.F.G., F.C.A., M.P., O.M.-B., Q.W., K.J.L., F.R., B.B., S.D., A.A., V.P. and S.-M.F. Writing, review and/or revision of the manuscript was carried out by P.A.M. and S.-M.F. Administrative, technical or material support (reporting or organizing data and constructing databases) was the responsibility of P.A.M., D.B., M.P. and J.V.E. Study supervision was carried out by S.-M.F.

Competing interests

S.-M.F. has received funding from Bayer, Merck, Gilead, Black Belt Therapeutics and Alesta Therapeutics, has consulted for Fund+ and is on the advisory board of Alesta Therapeutics. T.G.P.G. has consulted for Boehringer Ingelheim. All other authors declare no competing interests.

Additional information

Extended data is available for this paper at https://doi.org/10.1038/s43018-023-00513-2.

Supplementary information The online version contains supplementary material available at https://doi.org/10.1038/s43018-023-00513-2.

Correspondence and requests for materials should be addressed to Sarah-Maria Fendt.

Peer review information *Nature Cancer* thanks Andrew Hoy and the other, anonymous, reviewer(s) for their contribution to the peer review of this work.

Reprints and permissions information is available at www.nature.com/reprints.

Publisher's note Springer Nature remains neutral with regard to jurisdictional claims in published maps and institutional affiliations.

Patricia Altea-Manzano[1,2], Ginevra Doglioni[1,2,27], Yawen Liu[1,2,3,27], Alejandro M. Cuadros[1,2], Emma Nolan[4], Juan Fernández-García[1,2], Qi Wu[1,2,5], Mélanie Planque[1,2], Kathrin Julia Laue[6], Florencia Cidre-Aranaz[7,8], Xiao-Zheng Liu[1,2], Oskar Marin-Bejar[9,10], Joke Van Elsen[1,2], Ines Vermeire[1,2], Dorien Broekaert[1,2], Sofie Demeyer[11], Xander Spotbeen[12], Jakub Idkowiak[12,13], Aurélie Montagne[14], Margherita Demicco[1,2], H. Furkan Alkan[1,2], Nick Rabas[4], Carla Riera-Domingo[15,16], François Richard[17], Tatjana Geukens[17], Maxim De Schepper[17], Sophia Leduc[17], Sigrid Hatse[5], Yentl Lambrechts[5], Emily Jane Kay[18], Sergio Lilla[18], Alisa Alekseenko[19], Vincent Geldhof[20], Bram Boeckx[21,22], Celia de la Calle Arregui[1,2], Giuseppe Floris[23,24], Johannes V. Swinnen[12], Jean-Christophe Marine[9,10], Diether Lambrechts[21,22], Vicent Pelechano[19], Massimiliano Mazzone[15,16], Sara Zanivan[18,25], Jan Cools[11], Hans Wildiers[5], Véronique Baud[14], Thomas G. P. Grünewald[7,8,26], Uri Ben-David[6], Christine Desmedt[17], Ilaria Malanchi[4] & Sarah-Maria Fendt[1,2] ✉

[1]Laboratory of Cellular Metabolism and Metabolic Regulation, VIB-KU Leuven Center for Cancer Biology, Leuven, Belgium. [2]Laboratory of Cellular Metabolism and Metabolic Regulation, Department of Oncology, KU Leuven and Leuven Cancer Institute (LKI), Leuven, Belgium. [3]Department of Gastroenterology, Affiliated Hospital of Jiangsu University, Jiangsu University, Zhenjiang, China. [4]The Francis Crick Institute, London, UK. [5]Laboratory of Experimental Oncology, Department of Oncology, KU Leuven, Leuven, Belgium. [6]Department of Human Molecular Genetics & Biochemistry, Faculty of Medicine, Tel Aviv University, Tel Aviv, Israel. [7]Hopp-Children's Cancer Center (KiTZ), Heidelberg, Germany. [8]Division of Translational Pediatric Sarcoma Research, German Cancer Research Center (DKFZ), German Cancer Consortium (DKTK), Heidelberg, Germany. [9]Laboratory for Molecular Cancer Biology, VIB Center for Cancer Biology, Leuven, Belgium. [10] Department of Oncology, KU Leuven, Leuven, Belgium. [11]Laboratory for Molecular Biology

of Leukemia, VIB-KU Leuven, Leuven, Belgium. [12]Laboratory of Lipid Metabolism and Cancer, Department of Oncology, KU Leuven, Leuven, Belgium. [13]Department of Analytical Chemistry, Faculty of Chemical Technology, University of Pardubice, Pardubice, Czech Republic. [14]Université Paris Cité, NF-kappaB, Différenciation et Cancer, Paris, France. [15]Laboratory of Tumor Inflammation and Angiogenesis, VIB Center for Cancer Biology, Leuven, Belgium. [16] Laboratory of Tumor Inflammation and Angiogenesis, Center for Cancer Biology, Department of Oncology, KU Leuven, Leuven, Belgium. [17]Laboratory for Translational Breast Cancer Research, Department of Oncology, KU Leuven, Leuven, Belgium. [18]Cancer Research UK Beatson Institute, Glasgow, UK. [19]SciLifeLab, Department of Microbiology, Tumor and Cell Biology, Karolinska Institute, Solna, Sweden. [20]Laboratory for Angiogenesis and Vascular Metabolism, VIB-KU Leuven, Leuven, Belgium. [21]Laboratory of Translational Genetics, VIB Center for Cancer Biology, Leuven, Belgium. [22]Laboratory of Translational Genetics, Department of Human Genetics, KU Leuven, Leuven, Belgium. [23]Department of Imaging and Pathology, Laboratory of Translational Cell & Tissue Research, KU Leuven, Leuven, Belgium. [24]Department of Pathology, University Hospitals Leuven, KU Leuven, Leuven, Belgium. [25]School of Cancer Sciences, University of Glasgow, Glasgow, UK. [26]Institute of Pathology, Heidelberg University Hospital, Heidelberg, Germany. [27]These authors contributed equally: Ginevra Doglioni, Yawen Liu. ✉e-mail: sarah-maria.fendt@kuleuven.be

https://doi.org/10.1038/s43018-023-00513-2

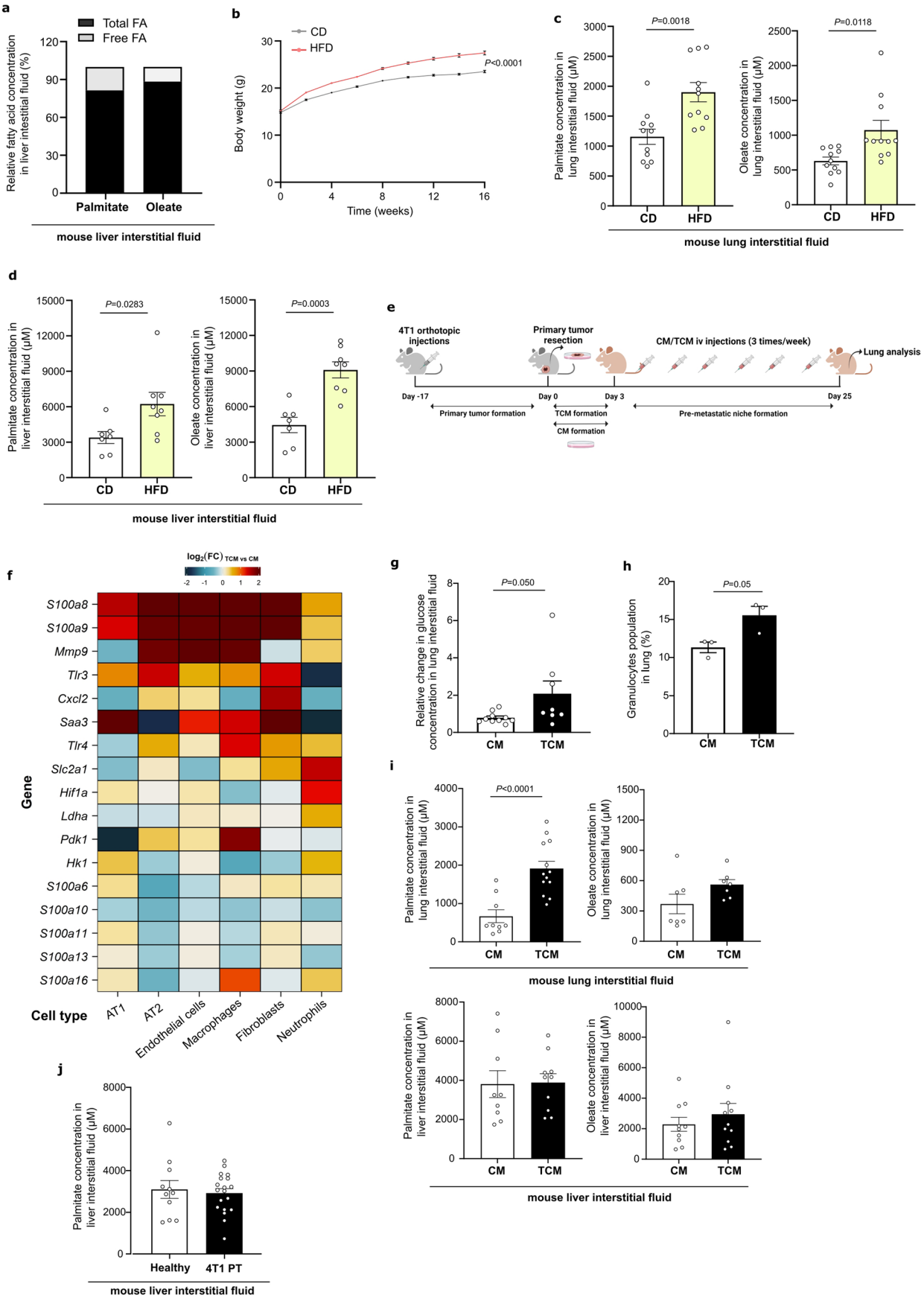

Extended Data Fig. 1 | See next page for caption.

https://doi.org/10.1038/s43018-023-00513-2

Extended Data Fig. 1 | High fat diet enhances several fatty acids, while during pre-metastatic niche formation only palmitate increases. a. Fraction of free fatty acids (gray) over total fatty acid content (black) of the liver interstitial fluid of healthy BALB/c mice ($n = 7$). **b**. Mouse weight gain upon high fat or control diet over the course of the experiment. Data are presented as mean ± SEM (n =60 mice). Mixed-effects analysis with Sidak's multiple comparisons. **c**. Palmitate and oleate abundance in the lung interstitial fluid of BALB/c mice after 16 weeks on control (CD) or high fat (HFD) diet ($n = 11$ mice). Data are presented as mean ± SEM of absolute concentration measured by mass spectrometry. Unpaired two-tailed *t*-tests with Welch correction. **d**. Palmitate and oleate abundance in the liver interstitial fluid of BALB/c mice after 16 weeks on CD or HFD diet ($n = 8$ mice). Data are presented as mean ± SEM of absolute concentration measured by mass spectrometry. Unpaired two-tailed *t*-tests with Welch correction. **e**. Schematic illustration for experimental pre-metastatic niche formation procedure. CM, control media; TCM, tumor conditioned media; i.v. intravenous. **f**. Changes in gene expression in lung populations upon TCM injection relative to CM injections, for genes whose upregulation has been previously linked to pre-metastatic niche formation, such as *S100a8*, *S100a9*, *Mmp9*[88,89] and *Tlr3* and *Cxcl2* in lung alveolar type II cells[88], *Tlr4* and *Saa3* in lung endothelial cells and macrophages[90]; *Slc2a1*, *Pdk1*, and *Ldha* in macrophages[91], and S100 genes in lung fibroblasts[92]. The color scale denotes log2 fold changes in TCM vs. CM. **g**. Relative glucose concentration in the lung interstitial fluid of healthy BALB/c mice exposed to control media ($n = 10$ mice) or tumor condition media ($n = 8$ mice). Data are presented as mean ± SEM. Unpaired two-tailed *t*-tests with Welch correction. **h**. Granulocytes population (which includes neutrophils) present in the lungs after induction of pre-metastatic niche formation using tumor conditioned media or control media. Data are presented as mean ± SEM ($n = 3$ mice). Unpaired two-tailed *t*-tests with Welch correction. **i**. Palmitate and oleate abundance in the lung ($n = 16$) and liver ($n \geq 7$) interstitial fluid of BALB/c mice injected with control media (CM) or 4T1 tumor conditioned media (TCM) (3 weeks, 3 times/week). Data are presented as mean ± SEM. Unpaired two-tailed *t*-tests with Welch correction. **j**. Palmitate concentration in the liver interstitial fluid of healthy ($n = 11$ mice) or 4T1 tumor-bearing (PT) ($n = 19$ mice) BALB/c mice. Data are presented as mean ± SEM.

https://doi.org/10.1038/s43018-023-00513-2

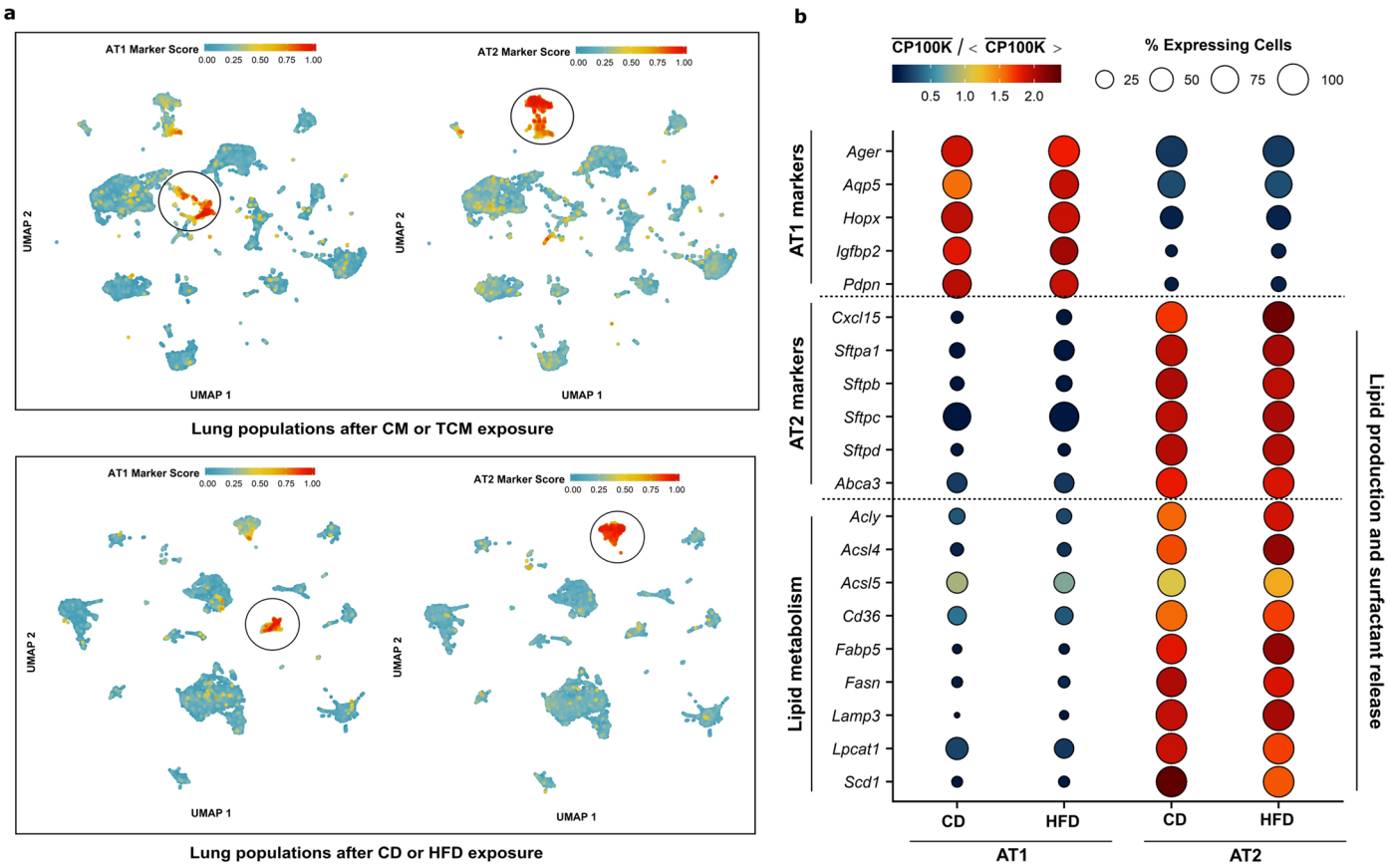

Extended Data Fig. 2 | High fat diet moderately impacts gene expression but increases the fraction of lung resident alveolar type II cells. a. UMAP plots for the scRNA-seq data corresponding to lungs preconditioned with control media (CM) and tumor conditioned media (TCM), or control diet (CD) and high fat diet (HFD). Color-coded based on GSVA-based marker scores for gene sets corresponding to alveolar type I (AT1) and II (AT2) marker genes. Identified clusters are indicated within black circles. Marker scores are scaled to the range 0–1 for each market set (see Methods). **b**. scRNA-seq-based gene expression vs. cell type and diet condition profiles for known marker for AT1 and AT2 cells and lipid-related genes indicated on the left-hand side. Scaled expression levels are indicated by the color scale, where $\overline{CP100k}$ denotes the average gene expression level (in counts per 100k reads) over all cells of a given type in each condition, and $\overline{\overline{CP100k}}$ the average of the latter over all cell types and condition media. The areas of the circles represent the percentage of cells with non-zero expression of each gene among all cells of each type and in each dietary condition. CD, control diet; HFD, high fat diet. **c**. Fractions of cells corresponding to AT2 cells, among all cells present in the lung of mice exposed to control (CD) or high fat (HFD) diet, as determined from scRNA-seq data.

https://doi.org/10.1038/s43018-023-00513-2

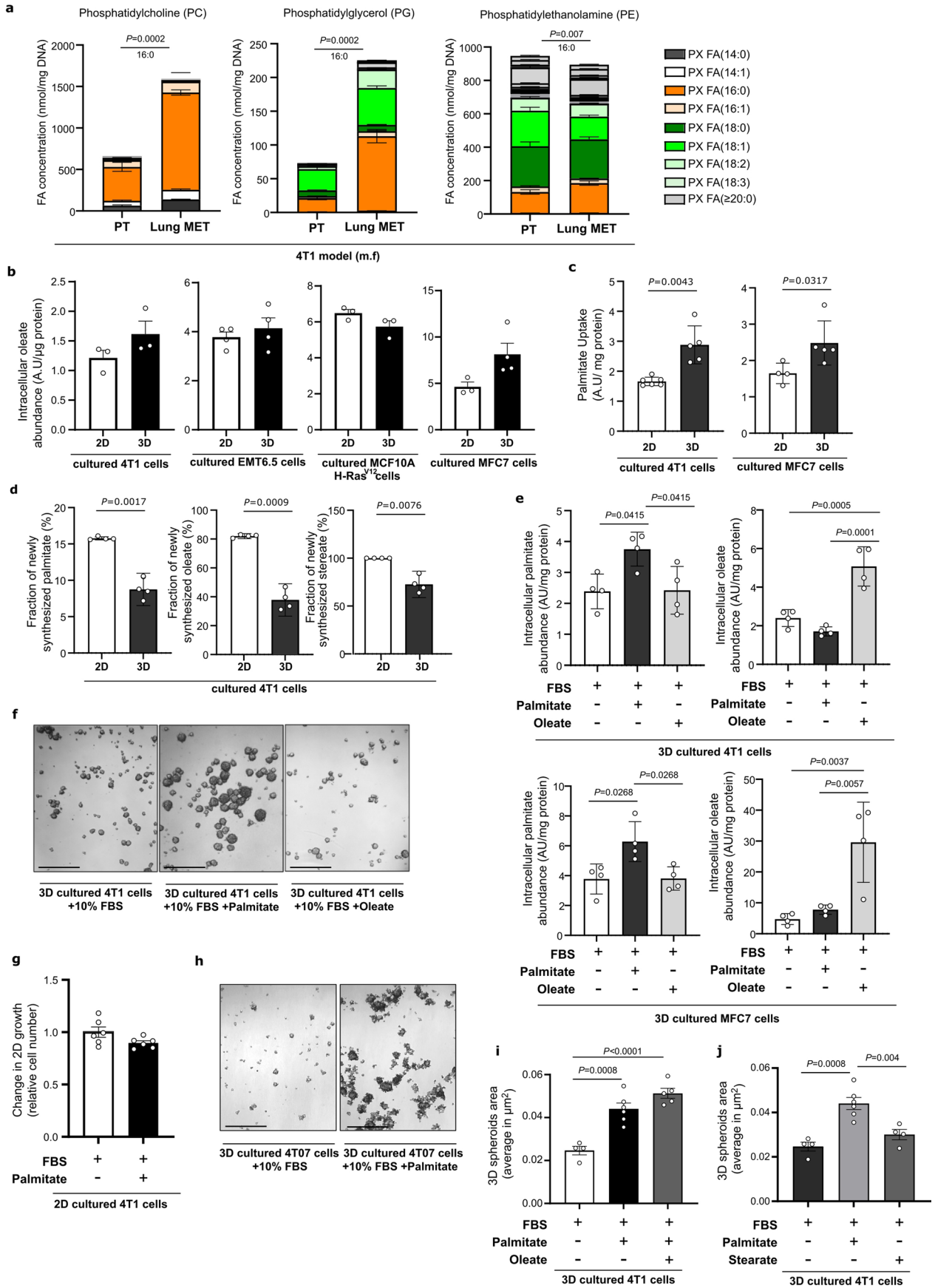

Extended Data Fig. 3 | See next page for caption.

https://doi.org/10.1038/s43018-023-00513-2

Extended Data Fig. 3 | Lung metastases show an increase in lipid species enriched in palmitoyl acyl chains typically found in the pulmonary surfactant. a. Fatty acid composition of the lipid classes phosphatidylcholine, phosphatidylglycerol and phosphatidylethanolamine in breast primary tumor and lung metastasis tissues from BALB/c mice orthotopically injected with 4T1 breast cancer cells. Data are presented as mean ± SEM ($n = 6$ mice). Unpaired nonparametric two-tailed Mann–Whitney *U*-tests. **b**. Intracellular oleate abundance from mouse (4T1, EMT6.5) and human (MCF10A H-Ras^{V12}, MCF7) breast cancer cells cultured on soft-agar (3D) or attached (2D) conditions. Data are presented as mean ± SEM ($n = 3$ and 4 biological replicates). **c**. Palmitate uptake measured by $^{13}C_{16}$-Palmitate intracellular incorporation in 3D spheroids ($n = 5$ biological replicates) and 2D ($n = 6$ and 4 biological replicates) cultured breast cancer cells after 5 d of incubation with BSA-conjugated $^{13}C_{16}$-Palmitic acid. Data are presented as mean ± SEM. Unpaired two-tailed *t*-tests with Welch correction. **d**. Fraction on newly synthesized fatty acids estimated by fatty acid isotopomer spectral analysis based on mass isotopomer distribution (MID) of $^{13}C_6$-glucose incorporation in 3D spheroids and 2D cultured breast cancer cells in the presence of extra palmitate (75µm) for 5 d. Data are presented as mean ± 95% confidence interval ($n = 4$ biological replicates). Unpaired two-tailed *t*-tests with Welch correction. **e**. Intracellular palmitate and oleate abundance from 3D spheroids mouse (4T1) and human (MCF7) breast cancer cells. Data are presented as mean ± SEM ($n = 4$ biological replicates). One-way ANOVA with Holm-Sidak's multiple comparison test. **f**. Representative pictures of 4T1 spheroids cultured in 10% FBS, or 10% FBS in the presence of palmitate (75 µm) or oleate (116 µm). Scale bar, 0.5 µm. A representative of $n = 3$ experiments is shown. **g**. Relative proliferation of 2D cultured 4T1 cells (with or without extra palmitate) normalized to condition without extra palmitate. Data are presented as mean ± SEM ($n = 6$ biological replicates). **h**. Representative pictures of 4T07 spheroids cultured in 10% FBS with or without extra palmitate (75 µm). Scale bar, 0.5 µm. A representative of $n = 3$ experiments is shown. **i-j**. 3D spheroids growth of 4T1 cells upon palmitate + oleate sup (**i**) and stearate (**j**) supplementation compared to control or palmitate supplementation, represented by the average spheroids area of >100 spheroids. Data are presented as mean ± SEM ($n = 4$ and 5 biological replicates). One-way ANOVA with Holm-Sidak's multiple comparison test.

https://doi.org/10.1038/s43018-023-00513-2

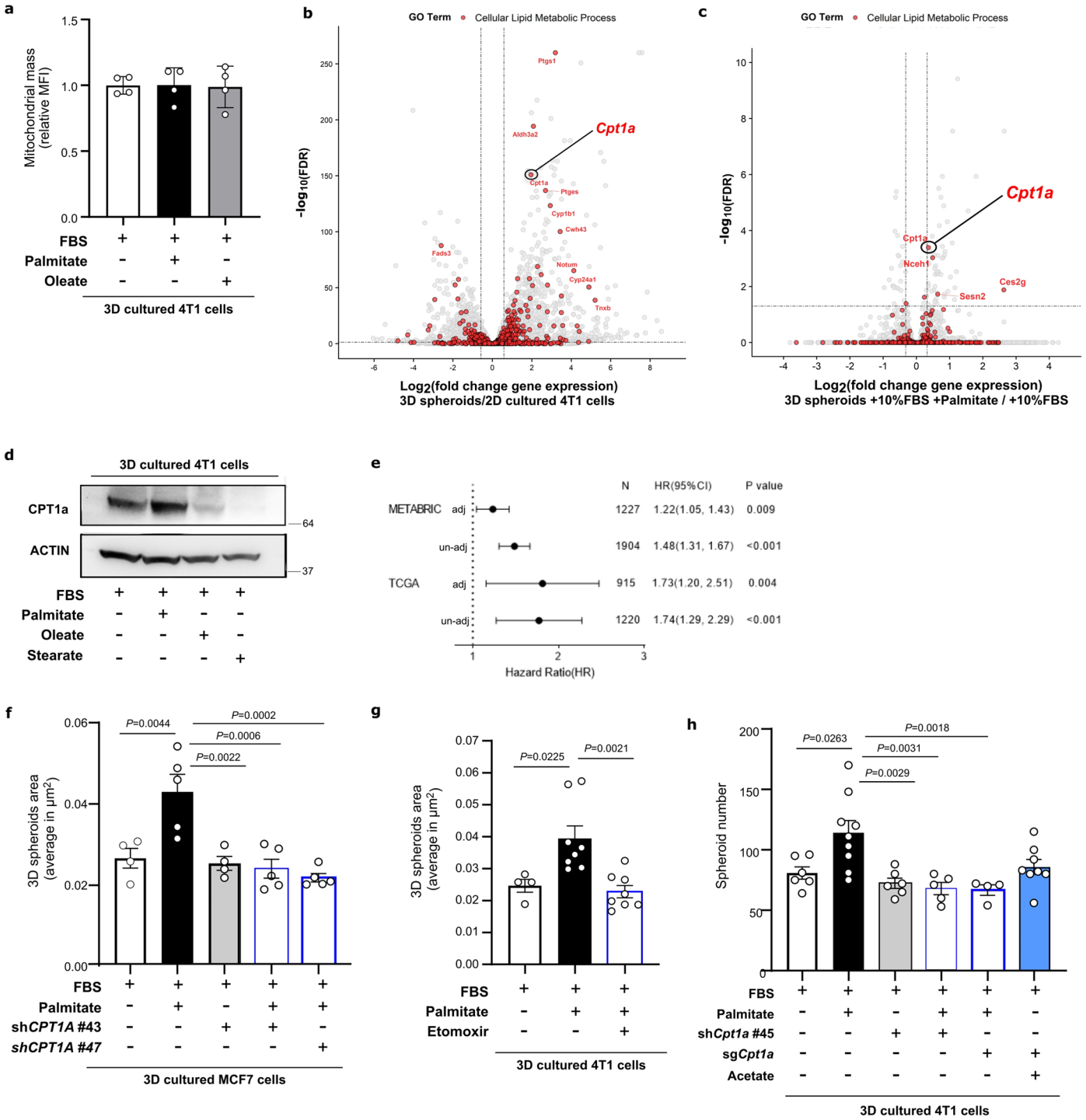

Extended Data Fig. 4 | See next page for caption.

https://doi.org/10.1038/s43018-023-00513-2

Extended Data Fig. 4 | CPT1a expression is upregulated in metastases and is associated with poor prognosis in breast cancer patients. a. Mitochondrial mass represented by mean relative fluorescence (MFI) of MitoTracker in 3D spheroids 4T1 cells growing in the absence or presence of palmitate or oleate for 5 d. MFI is shown relative to the level of MitoTracker fluorescence of 10% FBS condition. Data are presented as mean ± SD ($n = 4$ biological replicates). **b-c**. Differentially expressed genes in (b) 4T1 cells cultured in 3D spheroids or 2D monolayer in the presence of extra palmitate, or (c) in 3D spheroid 4T1 in the presence or absence of extra palmitate (10% FBS + palmitate or 10% FBS). Calculated differences in gene expression are presented by plotting the negative log10 of false discovery rate (Y-axis) against the log2 fold change of gene expression (X-axis). Each dot represents an individual gene. In red, genes belong to the GEO term lipid metabolic process (GO:0006629). The highest-ranking (top 10) overexpressed genes or genes above the established cutoff are annotated. **d**. CPT1a expression in 3D spheroid 4T1 cells growing for 5 d in the presence of additional palmitate, oleate and stearate. A representative image of $n = 3$ experiments is shown. **e**. Forest plot depicting the hazard ratio (HR) (x-axis) and corresponding 95% confidence intervals (denoted by error bars) for overall survival of patients with primary breast cancer according to *CPT1A* expression from two different cohorts: TCGA ($n = 1,221$ patients) and METABRIC ($n = 1,904$ patients). Cox proportional hazards models were applied, controlling for age, tumor stage (cTNM-staging system), and tumor subtype in both datasets. Panel complementary to Fig. 3i. **f**. 3D spheroids growth of MCF7 cells upon CPT1a knockdown compared to scrambled control upon palmitate supplementation (75 µm) represented by the average spheroids area of >100 spheroids. Data are presented as mean ± SEM ($n = 4$ and 5 biological replicates). One-way ANOVA with Tukey's multiple comparison test. **g**. 3D spheroids growth (5 d) of 4T1 cells upon CPT1a inhibition using etomoxir (50 µm) in the presence of extra palmitate (75 µm) represented by the average spheroids area of >100 spheroids. Data are presented as mean ± SEM ($n = 4$ and 8 biological replicates). One-way ANOVA with Tukey's multiple comparison test. **h**. 3D spheroids number per well of 4T1 cells upon palmitate supplementation (75 µm), CPT1a genetic inhibition performed by shRNA (sh*Cpt1a*) and CRISPR (sg*Cpt1a*), and upon metabolic rescue by acetate (5mM). Data are presented as mean ± SEM ($n = 6, 8, 6, 5, 4$, and 8 biological replicates respectively). One-way ANOVA with Tukey's multiple comparison test.

https://doi.org/10.1038/s43018-023-00513-2

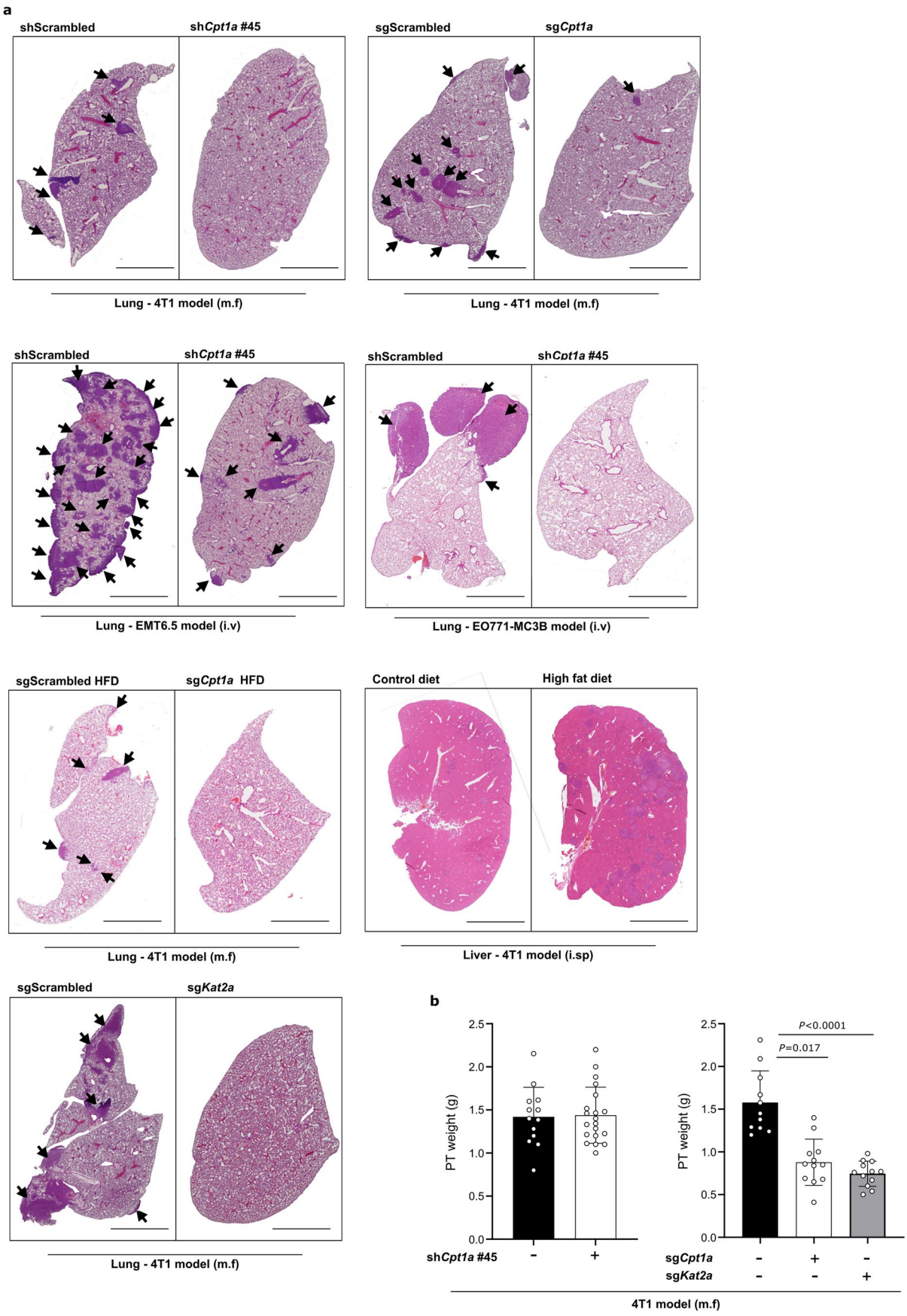

Extended Data Fig. 5 | See next page for caption.

https://doi.org/10.1038/s43018-023-00513-2

Extended Data Fig. 5 | Representative lung and liver H&E staining and primary tumor weight upon CPT1a and KAT2a loss. a. Representative pictures of tissue from the lung of mice injected with 4T1 (m.f.) and EMT6.5 (i.v.) upon genetic inhibition of CPT1a compared to non-targeting sg/shRNA as a control, based on H&E staining. Arrowheads indicate metastasis tissue. Arrows are not shown in the liver pictures. Scale bars, 2 mm. **b**. Final primary tumor weight (grams) from individual breast tumors upon genetic inhibition of CPT1A (n = 19 and 12 mice) and KAT2A (n = 11 mice) or control (n = 13 and 11 mice) in the 4T1 model (m.f.). Data are presented as mean ± SEM. One-way ANOVA with Dunnett's multiple comparison test.

https://doi.org/10.1038/s43018-023-00513-2

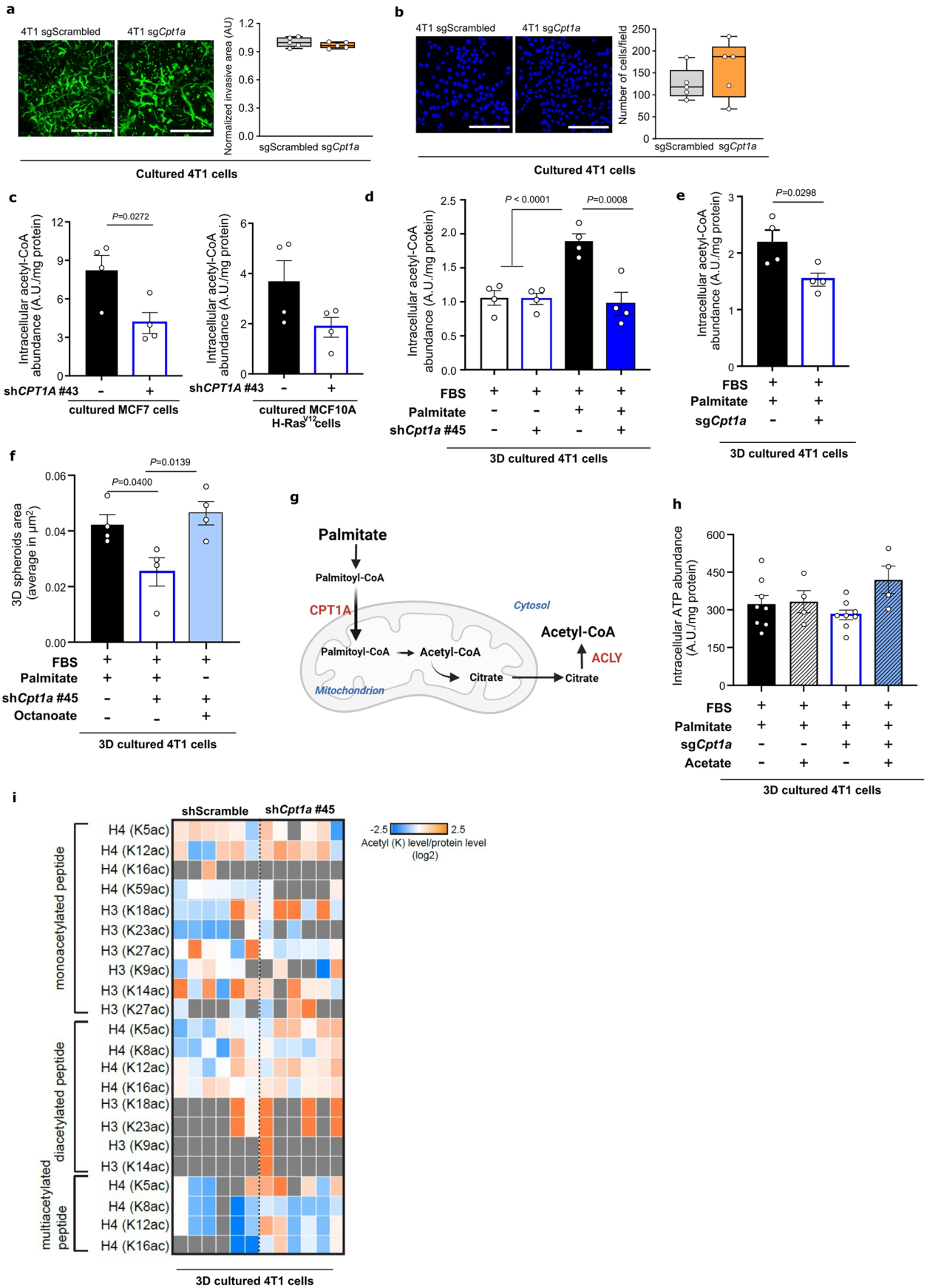

Extended Data Fig. 6 | See next page for caption.

https://doi.org/10.1038/s43018-023-00513-2

Extended Data Fig. 6 | Breast cancer spheroids in the presence of additional palmitate rely on CPT1a for acetyl-CoA production and for sustaining palmitate-induced 3D growth. a. Invasive ability in a 3D matrix of 4T1 cells upon CPT1a knockout (sg*Cpt1a*) compared to control (Scrambled) cells. Invasion was assessed by measuring the invasive area of cancer cells stained with calcein green. Representative images are depicted in the left panel (scale bar, 500 µm), and quantification in the right panel. Each dot represents a different, randomly selected microscopy field ($n = 5$ field). **b**. Migratory ability of 4T1 upon CPT1a knockout (sg*Cpt1a*) compared to control (Scrambled) cells. Migration was assessed by analyzing the total cells migrated through transwells coated with endothelial cells. Blue, DAPI nuclear staining. Representative images are depicted in the left panel (scale bar, 500 µm), and quantification in the right panel. Each dot represents a different, randomly selected microscopy field ($n = 5$ field). **c**. Relatives changes in acetyl-CoA abundance in human MCF10A H-Ras^{V12} and MCF7 breast cancer spheroids transduced with a lentiviral vector with shRNA against *CPT1A* (knockdown) compared to scrambled control sequences in the presence of extra palmitate. Data are presented as mean ± SEM ($n = 4$ biological replicates). Unpaired two-tailed *t*-tests with Welch correction. **d**-**e**. Relatives changes in acetyl-CoA abundance in mouse 4T1 breast cancer spheroids transduced with a lentiviral vector with RNA against *Cpt1a* (**c**, knockdown and **d**, knockout) compared to non-targeting sh/sgRNA control in the presence or absence of extra palmitate. Data are presented as mean ± SEM ($n = 4$ biological replicates). One-way ANOVA with Dunnett's multiple comparison test or two-tailed unpaired Student's *t*-test. **f**. 3D spheroids growth (5 d) of 4T1 cells upon palmitate supplementation (75 µm), CPT1a genetic inhibition (sh*Cpt1a*) and metabolic rescue with octanoate (130 µm) compared to non-targeting shRNA control, represented by the average of spheroids area of >100 spheroids. Data are presented as mean ± SEM ($n = 4$ biological replicates). One-way ANOVA with Dunnett's multiple comparison test. **g**. Schematic representation of the palmitate flux into the mitochondria via CPT1A and the ACLY-dependent export of the mitochondrial acetyl-CoA pool to the cytosol via citrate. **h**. Intracellular levels of ATP in CPT1a knockout and control 4T1 3D spheroids cultured for 5 d in medium containing extra palmitate (75 µm) or acetate as metabolic rescue (5 mM). Data are presented as mean ± SEM ($n = 8$ and 4 biological replicates). **i**. Heatmap display of the log2 transformed ratios obtained for the indicated histone acetylation for CPT1a knockdown and control 4T1 3D spheroids cultured for 5 d in medium containing extra palmitate (75 µm). Relative abundances ratios, light/SILAC heavy, were obtained with the SILAC (Stable Isotope Labeling with Amino acids in Cell culture) internal standard strategy[93].

https://doi.org/10.1038/s43018-023-00513-2

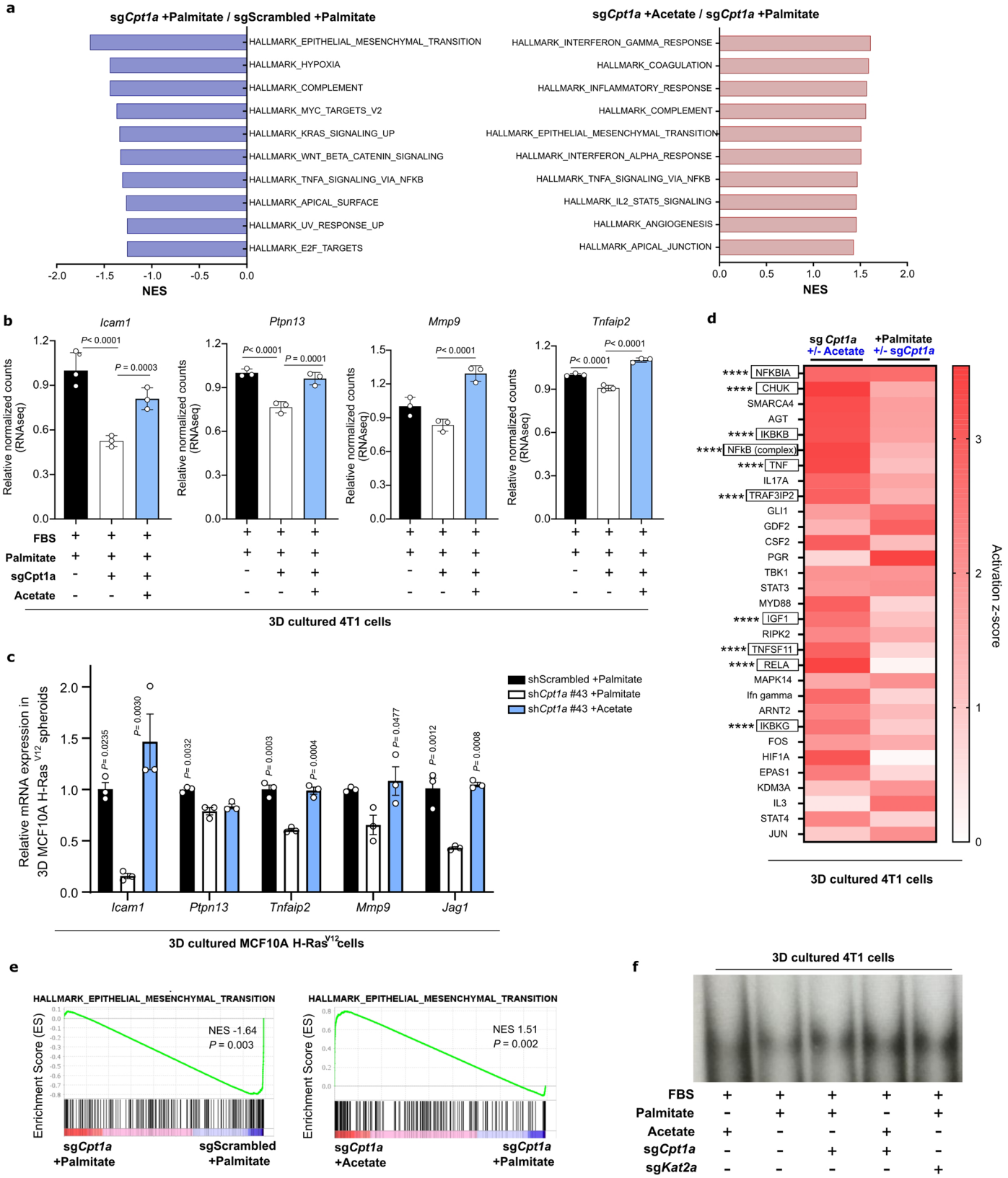

Extended Data Fig. 7 | See next page for caption.

https://doi.org/10.1038/s43018-023-00513-2

Extended Data Fig. 7 | CPT1a deletion reduces NF-κB signaling pathway but does not affect p65 DNA binding. a. Top 10 enriched pathways (p<0.05) obtained from gene set enrichment analysis (GSEA) of 4T1 spheroids upon CPT1a inhibition (sg*CPT1a*), in the presence of the extra palmitate (75 µm) or acetate as metabolic rescue (5 mM) using the Hallmark gene set from Molecular Signatures Database (MSigDB). NES, normalized enrichment score. **b**. Relative expression of genes implicated in invasion and metastasis, and that are known to be regulated via NF-κB activation in 4T1 spheroids. Fold change is calculated from normalized raw counts (RNA-sequencing) of CPT1a knockout and non-targeting sgRNA control 4T1 3D spheroids cultured for 5 d in medium containing extra palmitate (75 µm) or acetate (5 mM). Data are presented as mean ± SD ($n = 3$ biological replicates). Multiple testing correction with false discovery rate (FDR) estimation. **c**. Relative expression of genes implicated in invasion and metastasis, and that are known to be regulated via NF-κB activation in MCF10A H-Ras^{V12} spheroids. Fold changes are calculated for CPT1a knockdown and non-targeting sgRNA control MCF10A H-Ras^{V12} 3D spheroids cultured for 5 d in medium containing extra palmitate (75 µm) or acetate (5 mM) and are normalized to gene expression in control cells. Data are presented as mean ± SEM ($n = 3$ biological replicates). One-way ANOVA with Dunnett's multiple comparison test. **d**. Upstream regulator analysis performed using Ingenuity Pathway Analysis using the differential gene expression of CPT1A knockout (sg*Cpt1a*) 4T1 3D spheroids in the presence or absence of acetate (metabolic rescue, 5 mM) as input. Activation score of the top 30 upstream regulators (left column) was compared to those predicted for the differential gene expression of CPT1A knockout versus control conditions (in the presence of extra palmitate). Genes related to the activation of the NF-κB pathway are framed. Asterisks represent the overlap *P* value calculated using one-sided Fisher's Exact Test (****$P<0.0001$). **e**. GSEA enrichment plots comparing the gene expression profiles in 4T1 3D spheroids transduced with a lentiviral vector containing sg*Cpt1a* or sgScrambled as a control (left panel) and sg*Cpt1a* 4T1 3D spheroids cultured with or without acetate (right panel). NES, normalized enrichment score; the P value indicates the significance of the enrichment score (permutation test). **f**. Total p65 binding to DNA measured by electrophoretic mobility shift assay (EMSA). Arrow indicates the position of the NF-κB containing complex. A representative of $n = 3$ experiments is shown.

https://doi.org/10.1038/s43018-023-00513-2

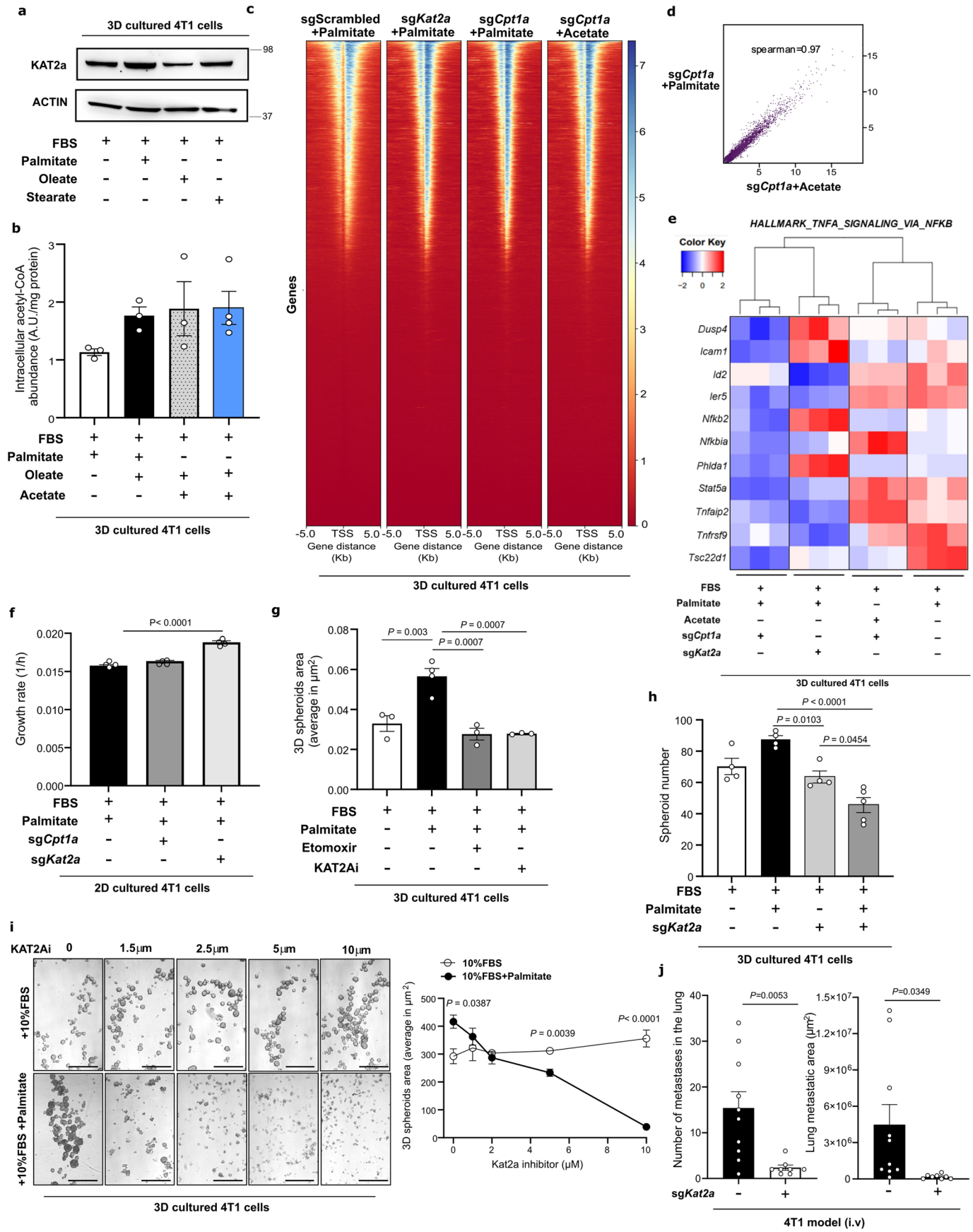

Extended Data Fig. 8 | See next page for caption.

https://doi.org/10.1038/s43018-023-00513-2

Extended Data Fig. 8 | Global histone acetylation and chromatin accessibility are not consistently changed upon CPT1a and/or KAT2a loss. a. KAT2a expression in 3D spheroid 4T1 cells growing for 5 d in the absence or presence of additional palmitate, oleate and stearate. A representative image of $n = 3$ experiments is shown. **b**. Intracellular levels of acetyl-CoA in 4T1 cells growing in 3D for 5 d in medium containing only 10% FBS, or supplemented with palmitate (75 mM), oleate (116 µm) or acetate (5 mM). Data are presented as mean ± SEM ($n = 4$ biological replicates). **c**. Heatmap of the signal intensity of H3K9ac-targeted gene loci in non-targeting RNA control, CPT1a and KAT2a knockout 4T1 3D spheroids cultured for 5 d in medium containing extra palmitate (75 µm) ($n = 3$ biological replicates). **d**. Correlation plot of H3K9 acetylation in 4T1 3D spheroids cultured in the presence of palmitate upon CPT1a inhibition with and without acetate (5 d). **e**. Heatmap and hierarchical clustering of top-scored downregulated genes of the NF-κB signaling pathway upon CPT1a deletion in 4T1 3D spheroids cultured in the presence of palmitate for 5 d, represented together with the expression status of the same genes upon acetate rescue and KAT2a deletion non-targeting sgRNA is used in control transfected samples ($n = 3$ biological replicates). **f**. Proliferation of 4T1 cells upon genetic inhibition of either *Cpt1a* or *Kat2a* in 2D culture measured using incucyte. Mean of growth rate ± SEM is shown ($n = 6$ biological replicates). One-way ANOVA with Dunnett's multiple comparison test. **g**. 3D spheroids in 4T1 cells upon pharmacologic inhibition of either KAT2a using the inhibitor CPTH2 (2 µm) or CPT1A using etomoxir (50 µm) cultured for 5 d in medium with or without extra palmitate supplementation. Size quantification is represented by the average spheroids area of >100 spheroids. Data are presented as mean ± SEM ($n = 3$ biological replicates). One-way ANOVA with Tukey's multiple comparison test. **h**. 3D spheroids number per well of 4T1 cells upon palmitate supplementation (75 µm), CPT1a or KAT2a genetic inhibition performed by CRISPR (sg*Cpt1a* and sg*Kat2a*) compared to non-targeting sgScrambled as a control, and upon metabolic rescue by acetate (5mM). Data are presented as mean ± SEM ($n = 4$ and 5 biological replicates). One-way ANOVA with Tukey's multiple comparison test. **i**. Dose-response of 3D spheroid growth to the pharmacologic inhibition of KAT2a using CPTH2 inhibitor with or without extra supplementation of palmitate. *Left panel*, representative pictures. *Right panel*, spheroid size quantification is represented by the average spheroids area of >100 spheroids ($n = 4$ biological replicates). Two-way ANOVA with Tukey's multiple comparison test. **j**. Total area and number of metastases in the lung of mice after 14 d of intravenous (i.v.) injections with 4T1 Kat2a knockout (sg*Kat2a*, $n = 8$ mice) or non-targeting sgScrambled control cells ($n = 10$ mice) analyzed by H&E staining. Unpaired two-tailed *t*-tests with Welch correction.

https://doi.org/10.1038/s43018-023-00513-2

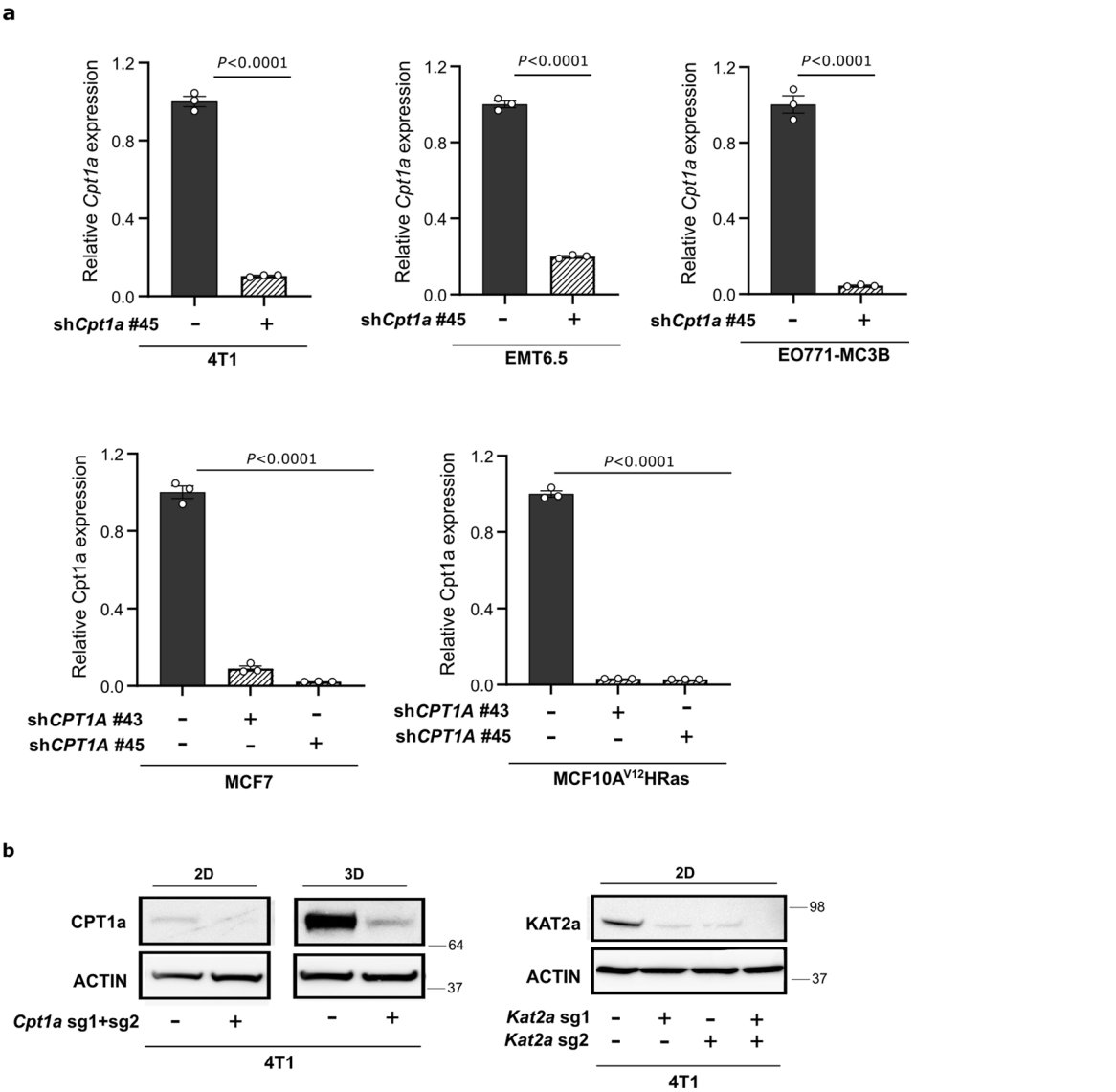

Extended Data Fig. 9 | Protein and RNA expression of genetically modified breast cancer cells. a. Relative gene expression analysis of *CPT1A* in human (MCF10A H-Ras^{V12} and MCF7), mouse (4T1, EO771-MCB3 and EMT6.5) breast cancer cells infected with either a control shRNA, or two different *CPT1A*, or *Cpt1a* shRNAs normalized to the control condition. Data are presented as mean ± SD ($n = 3$ biological replicates). Unpaired two-tailed *t*-tests. **b**. Protein expression in mouse 4T1 cancer cells infected with either a non-targeting sgScrambled as a control or two different sgRNA against *Cpt1a* and *Kat2a* gRNAs. A representative of $n = 3$ experiments is shown.

https://doi.org/10.1038/s43018-023-00513-2

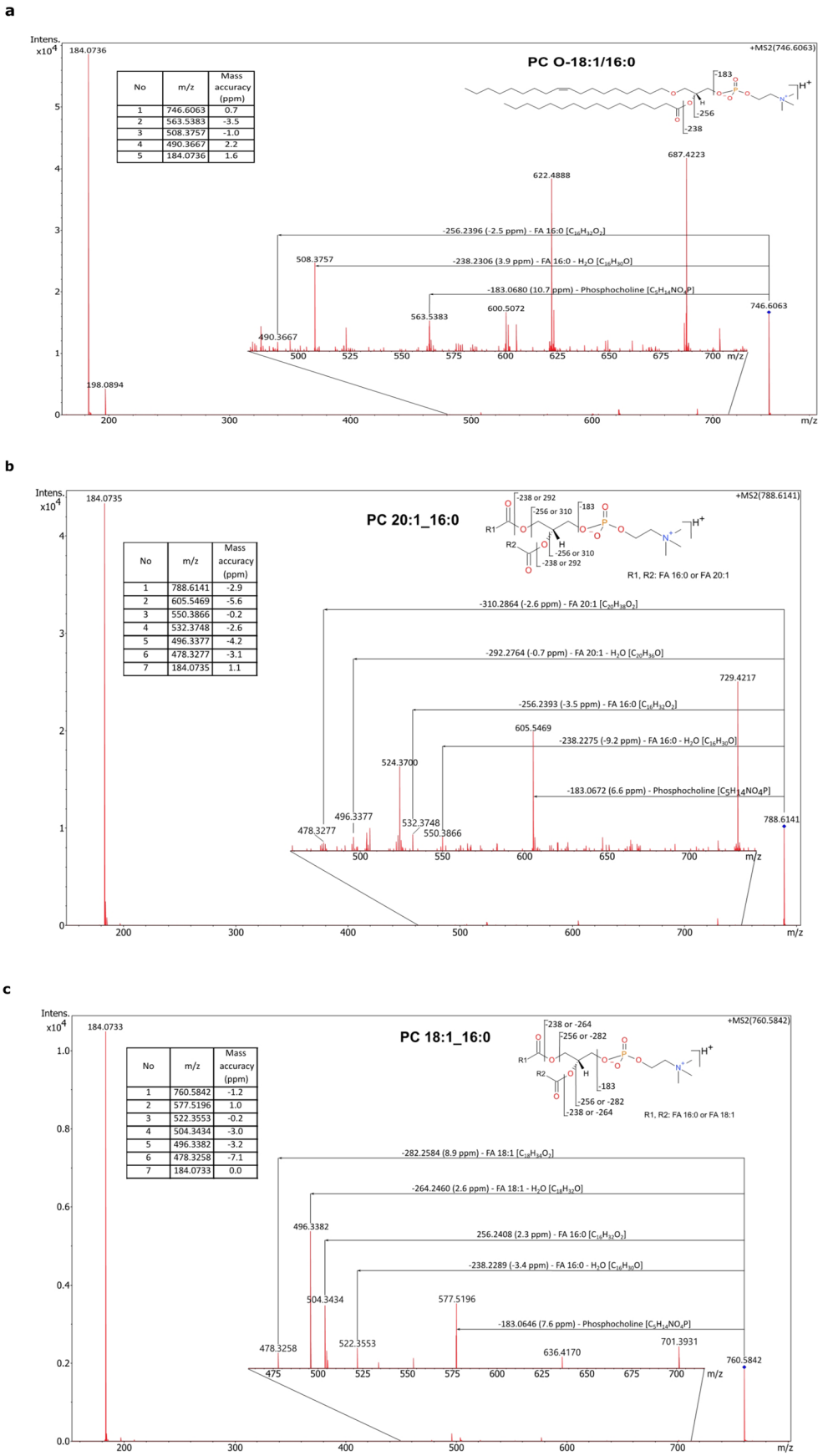

Extended Data Fig. 10 | See next page for caption.

https://doi.org/10.1038/s43018-023-00513-2

Extended Data Fig. 10 | MS/MS validation of lipids detected in metastases by MALDI-MSI molecular imaging. a. MS/MS spectrum of the ion at m/z 760.5842 detected from the metastatic areas within the lung tissue in positive ion mode using the timsTOF fleX. Ions supporting the assignment of PC O-18:1_16:0 are annotated with their corresponding mass accuracy. **b**. MS/MS spectrum of the ion at m/z 760.5842 detected from the metastatic areas within the lung tissue in positive ion mode using the timsTOF fleX. Ions supporting the assignment of PC 20:1_16:0 are annotated with their corresponding mass accuracy. **c**. MS/MS spectrum of the ion at m/z 760.5842 detected from the metastatic areas within the lung tissue in positive ion mode using the timsTOF fleX. Ions supporting the assignment of PC18:1_16:0 are annotated with their corresponding mass accuracy.

nature portfolio

Corresponding author(s): Sarah-Maria Fendt

Last updated by author(s): Dec 19, 2022

Reporting Summary

Nature Portfolio wishes to improve the reproducibility of the work that we publish. This form provides structure for consistency and transparency in reporting. For further information on Nature Portfolio policies, see our Editorial Policies and the Editorial Policy Checklist.

Statistics

For all statistical analyses, confirm that the following items are present in the figure legend, table legend, main text, or Methods section.

n/a	Confirmed
☐	☒ The exact sample size (*n*) for each experimental group/condition, given as a discrete number and unit of measurement
☐	☒ A statement on whether measurements were taken from distinct samples or whether the same sample was measured repeatedly
☐	☒ The statistical test(s) used AND whether they are one- or two-sided *Only common tests should be described solely by name; describe more complex techniques in the Methods section.*
☒	☐ A description of all covariates tested
☒	☐ A description of any assumptions or corrections, such as tests of normality and adjustment for multiple comparisons
☐	☒ A full description of the statistical parameters including central tendency (e.g. means) or other basic estimates (e.g. regression coefficient) AND variation (e.g. standard deviation) or associated estimates of uncertainty (e.g. confidence intervals)
☐	☒ For null hypothesis testing, the test statistic (e.g. *F*, *t*, *r*) with confidence intervals, effect sizes, degrees of freedom and *P* value noted *Give P values as exact values whenever suitable.*
☒	☐ For Bayesian analysis, information on the choice of priors and Markov chain Monte Carlo settings
☒	☐ For hierarchical and complex designs, identification of the appropriate level for tests and full reporting of outcomes
☐	☒ Estimates of effect sizes (e.g. Cohen's *d*, Pearson's *r*), indicating how they were calculated

Our web collection on statistics for biologists contains articles on many of the points above.

Software and code

Policy information about availability of computer code

Data collection	GC-MS data were collected using MSD Chemstation Data Analysis (vE.02.0.2.1431) or Agilent Mass Hunter (vB.0802 Build 8.2.8260.0). LC-MS data were collected using the Xcalibur software (Thermo Scientific). H&E stainings on tissue samples were acquired using ZEN 2 software (Zeiss). Western blot imaging adquisition was performed using ImageQuant LAS 4000 (GE Healthcare). Microscopy images were acquired using Motic Images Plus 2.0 software (Motic). Confocal microscopy imaging was performed on a Leica TCS SP8 X confocal microscope equipped with a White Light Laser and a HCX PL APO CS 10x/0.40 DRY objective. Sequencing data were adquired on Illumina Hiseq 4000 platform and NovaSeq 6000 Syste (Illumina).Flow cytometry data were acquired using BD FACSDiva™ Software (v7.0). Mass spectrometry Images were acquired using FlexImaging 7.0 software (Bruker Daltonics, Bremen, Germany).
Data analysis	Single-cell sequenced reads were then mapped to the mouse genome (mm10 build GRCm38.p6) using the Cell Ranger software (10x Genomics), and the resulting single-cell gene expression data were analyzed within the R/Bioconductor framework. Specifically, the raw UMI count matrices for each individual sample were first imported using Seurat, and then converted for further processing with Monocle. Low-quality cells were then filtered based on standard quality-control metrics, with sample-specific thresholds chosen based on evaluating quality-control histograms for each sample independently. In particular, cells were filtered based on their mitochondrial RNA content (allowing for a maximum of 10% in all cases), library size (removing cells with total UMI counts below 500 in both cases and number of detected genes (removing cells expressing less than 200 genes in both cases. Genes expressed in less than 5 cells were additionally ignored in all subsequent analyses. Size-factor and variance-stabilizing normalization (based on fitting to a negative binomial distribution) were then applied to the filtered data sets, and highly variable genes (HVGs) were identified for each of them based on their departure from the average normalized dispersion versus expression trend observed among all genes. Principal component analysis (PCA) was then performed on the size factor-normalized and variance-stabilized count matrix restricted to these genes only, followed by 2D UMAP dimensional reduction 92 based on the resulting top 50 principal components. After that, cells were clustered in the UMAP plane by applying the Louvain graph-based algorithm at high resolution. The resulting fine-grained clusters were then manually annotated to specific cell types, based on evaluating the cluster-averaged normalized expression profiles of several cell type-specific markers. For marker score analysis, cell-type marker scores were calculated using the GSVA (gene set variation analysis) package. RNA sequencing analysis of patient tumors was performed as follow: optical duplicates and adapator sequences were removed from the raw

sequencing reads before aligning to the transcriptome and the reference genome using TopHat 2.0 95 and Bowtie 2.0 96. Counts were assigned to genes using the HTSeq software package. Raw sequencing reads were mapped to the transcriptome: > 25000 different transcripts were identified that could be detected in at least 50% of the samples.
RNA sequencing analysis of cultured cells was performed as follow: reads were cleaned with the fastq-mcf software, after a quality control was performed with FastQC (v0.11.9). The high-quality reads were then mapped to the Mus Musculus reference genome (GRCm38/mm10) with HISAT2 (v2.1.0) and the abundance of reads per gene was determined with HTSeq-count. Differential gene expression analysis was performed with the R package DESeq2 (v1.22.0).
For ChIP seqeuncing analysis, raw sequencing reads were cleaned with fastq-mcf and a quality control was performed with FastQC (v0.11.3). These cleaned reads were then aligned to the mm10 genome using BWA and duplicates were removed with Picard (v1.130). deepTools (v1.6) was used to plot heatmaps of signals centered around TSS as well as to plot Spearman correlation
For mass spectrometry analyses, isotopologue distributions were extracted from the raw ion chromatograms using Matlab (R2016b.ink). For SILAC analysis, MS .raw files were processed with MaxQuant software (version 1.6.6.3) and searched with the Andromeda search engine with the following settings: minimal peptide length 6 amino acids, fixed modification Carbamidomethyl (C) and variable modifications Acetyl (K), Acetyl (Protein N-term) and Oxidation (M). Multiplicity was set to 2, where the light labels were Arg0 and Lys0 and the heavy labels were Arg10 and Lys8. The false discovery rates (FDRs) at the protein and peptide level were set to 1%. Perseus (version 1.6.2.2) was used for downstream analysis. The data were filtered to remove potential contaminants, reverse peptides which match a decoy database, and proteins only identified by site. Foir lipidomics analysis, peak integration was performed with the MultiQuantTM software version 3.0.3. Lipid species signals were corrected for isotopic contributions calculated using Python Molmass 2019.1.1.
H&E stainings and immunofluorescences on tissue slides were done using ZEN Blue software (Zeiss) and QuPath software package (Version 0.1.2).
Confocal images were analyzed using LAS X 3.3 software (Leica) to obtain maximum projection images. Quantification of invasive area and invasive distance was performed on using the FIJI 2.3.1 distribution of ImageJ2.3.0.
Flow cytometry data were analyzed using FlowJo software (v10.8.0).
Mass spectrometry Images were analyzed using SCiLS Lab 2023a software and MetaboScape 2021a (Bruker Daltonics, Bremen, Germany). For fragmentation spectra, Bruker Compass DataAnalysis (v6.0) was used.
R software (version 4.0.5 (R Project for Statistical Computing)) was used to perform KM survival analysis, univariate and multivariate Cox regressions . All rest statistical analyses were done in GraphPad Prism 8.

For manuscripts utilizing custom algorithms or software that are central to the research but not yet described in published literature, software must be made available to editors and reviewers. We strongly encourage code deposition in a community repository (e.g. GitHub). See the Nature Portfolio guidelines for submitting code & software for further information.

Data

Policy information about availability of data

All manuscripts must include a data availability statement. This statement should provide the following information, where applicable:

- Accession codes, unique identifiers, or web links for publicly available datasets
- A description of any restrictions on data availability
- For clinical datasets or third party data, please ensure that the statement adheres to our policy

Mouse scRNA-sequencing, RNA-sequencing, and ChIP-sequencing data have been deposited in the Gene Expression Omnibus (GEO) under accession code are available at the GEO under accession code GSE196993. Source data for in vivo data represented in Figs. 1–7 and Extended Data Figs. 1–10 have been provided as Source Data files. Gel source images are available in Supplementary Fig. 1. All other data supporting the findings of this study are available within the Article and the Supplementary Information, and from the corresponding author on reasonable request.

Field-specific reporting

Please select the one below that is the best fit for your research. If you are not sure, read the appropriate sections before making your selection.

☒ Life sciences ☐ Behavioural & social sciences ☐ Ecological, evolutionary & environmental sciences

For a reference copy of the document with all sections, see nature.com/documents/nr-reporting-summary-flat.pdf

Life sciences study design

All studies must disclose on these points even when the disclosure is negative.

Sample size	In vitro sample sizes were based on previous similar studies that have given statistically significant results (doi: 10.1016/j.molcel.2020.11.027, doi: 10.1038/s41586-019-0977-x, doi: 10.1038/s41586-022-04758-2). For in vivo experiments, sample size was determined using power calculations with B=0.8 and P<0.05, based on preliminary data and previous studies, and respects the limited use of animal models in line with the 3R recommendations: Replacement, Reduction, Refinement.
Data exclusions	Identifying and removing outliers was made using the ROUT method of regression (Prism) with coefficient Q = 1%.
Replication	All experiments were performed at least in triplicate. All attempts at replication were successful.
Randomization	Mice were randomized before diet feeding, tumor conditioned/control media injections, or injection with the different cell lines. For in vitro studies, samples were randomized, when possible, prior data acquisition.
Blinding	Mice were given a unique number prior to data collection and analysis. Data was collected and analyzed blindly, and subsequently grouped in

Blinding

the corresponding cohorts for statistical analysis. For in vitro experiments, investigators were blinded to group allocation during data collection and/or analysis by giving an unique identifier other than the sample name.

Reporting for specific materials, systems and methods

We require information from authors about some types of materials, experimental systems and methods used in many studies. Here, indicate whether each material, system or method listed is relevant to your study. If you are not sure if a list item applies to your research, read the appropriate section before selecting a response.

Materials & experimental systems

n/a	Involved in the study
☐	☒ Antibodies
☐	☒ Eukaryotic cell lines
☒	☐ Palaeontology and archaeology
☐	☒ Animals and other organisms
☐	☒ Human research participants
☒	☐ Clinical data
☒	☐ Dual use research of concern

Methods

n/a	Involved in the study
☐	☒ ChIP-seq
☐	☒ Flow cytometry
☒	☐ MRI-based neuroimaging

Antibodies

Antibodies used

For western blot experiments, the following antibodies were used: CPT1a (Abcam, ab234111, 1:1000), GCN5L2/KAT2A (C26A10) (Cell signaling, 3305T, 1:1000), NF-kB p65 (acetyl K310) (Abcam, ab19870, 1:1000), NF-κB p65 (D14E12) (Cell signaling, 8242S), 1:1000, β-actin (Sigma, A5441, 1:10,000), Histone H3 (Abcam, ab1791, 1:2000). Mouse (Cell Signaling Technology, 7076; 1:4000) or rabbit (Cell Signaling Technology, 7074; 1:4000) were used as a secondary antibodies.
For ChIP sequencing analysis H3K9ac antibody (Cell signaling, 9649S, 1:50 dilution) was used.
For Flow cytometry experiments, CD45 (1:200 dilution, BD Bioscience, 550994), PDPN (BioLegend, 127409 1:200 dilution), CD31 (BD Bioscience, 562939 1:200 dilution), CD49f (Thermo Scientific, 25-0495-82 1:100 dilution), EpCAM (Thermo Scientific, 17-5791-82 1:200 dilution), MHC-II (BioLeged, 107643 1:100 dilution), and Viability efluor780 (ThermoFisher, 65-0865-14 1:800 dilution), and CD90.1 (BioLegend, 202505 1:400 dilution) were used.

Validation

For western blot and flow cytometry, antibodies were used as recommended in the respective data sheets and validated using knockdown cell lines when possible. For ChIP sequencing, antibody was validated by performing ChIP qPCRs targeting genes that have been reported to be regulated by H3K9ac.

Eukaryotic cell lines

Policy information about cell lines

Cell line source(s)

Human HEK293T epithelial cells, MCF10A, MCF7 and 4T1 cell lines were purchased from ATCC. Murine EMT6.5 mammary gland cancer cells were provided by R. Anderson (Peter MacCallum Cancer Center). EO771-MCB3 clone was provided by Prof. Mazzone VIB Center for Cancer Biology) and 4T07 cell line by Prof. Gomes (H Lee Moffitt Cancer Center). Parental EMT6 and EO771 were originally purchased from ATCC.

Authentication

None of the cell lines used were authenticated

Mycoplasma contamination

All cell lines were confirmed to be mycoplasma-free by routine screening with Mycoalert datection kit (Lonza).

Commonly misidentified lines
(See ICLAC register)

No commonly misidentified cell lines were used.

Animals and other organisms

Policy information about studies involving animals; ARRIVE guidelines recommended for reporting animal research

Laboratory animals

6-8-week old female Balb/c or C57BL/6JAX mice were used for cancer cell or media injections. 4-week old female Balb/c mice were used for diet studies. 8-10 week old female Sftpc-CreERT2 mice were used for AT2 cell isolation. All mice were housed under a regimen of 12 h light/12 h dark cycles and under conventional conditions.

Wild animals

No wild animals were used.

Field-collected samples

No field-collected samples were used.

Ethics oversight

For experiments involving orthotopic and experimental metastatic mouse models and diet, housing and experimental animal procedures were approved by the Institutional Animal Care and Research Advisory Committee of KU Leuven, Belgium, under the ECD number P007/2020, ECD P048/2020 and ECD P025/2020. For experiments involving Sftpc-CreERT2 mouse model, breeding and all animal procedures were performed at the Francis Crick Institute in accordance with UK Home Office regulations under project license PPL80/2531.

All animal studies comply with ethical regulations. For all experiments, the maximum permitted tumor volume was 1.8 cm3 and this limit was not exceeded in any experiment. Humane endpoints were determined using a scoring sheet to determine the condition of the mouse as follows: tumor size of 1.8 cm3, loss of ability to ambulate, labored respiration, surgical infection, or weight loss over 10% of initial body weight. Mice were monitored and upon detection of one of the previously mentioned symptoms, the animal was euthanized.

Note that full information on the approval of the study protocol must also be provided in the manuscript.

Human research participants

Policy information about studies involving human research participants

Population characteristics	CHEMOREL:newly diagnosed primary Luminal B-type breast cancer patients with grade 2/3, ER+, PR+/-, HER2- tumors was selected including (i) patients who remained disease-free for at least 6 to 10 years after the initial therapy (n=43), (ii) patients developing distant metastasis within 5 years after initial therapy (n=44), and (iii) primary metastasized patients (n=14). UPTIDER: Metastatic breast cancer, or hereditary cancer syndrome with a moderate to high lifetime risk of breast cancer, for which the patient is treated/followed in UZ Leuven. Age ≥ 18 years. Healthy lung tissue human participants: Human 'normal' lung tissue was collected from patients who underwent lung surgery for emphysematous lung volume reduction or tumorectomy. In the latter case, lung tissue from the resection specimen was taken as far away as possible from the tumor front.
Recruitment	CHEMOREL: patients with breast cancer, who were diagnosed and treated at the UZ Leuven Multidisciplinary Breast Center, are documented (i.e. patient and tumor characteristics, therapy, and follow-up information including relapse and survival). UPTIDER: female patients (≥ 18 years) with metastatic breast cancer that consent to participate undergo a rapid research autopsy in the first 12 hours after death. Healthy lung tissue human participants: patients who underwent lung surgery for emphysematous lung volume reduction or tumorectomy and consented to donate resected tissue. For interstital fluid measurements in pre-metastatic niche, only patients who underwent lung surgery for emphysematous were considered as "healthy" lung tissue.
Ethics oversight	Approval by UZ/KU Leuven, protocol S57123. NCT04531696, S64410. A written informed consent was obtained from all participants included in this study.

Note that full information on the approval of the study protocol must also be provided in the manuscript.

ChIP-seq

Data deposition

☒ Confirm that both raw and final processed data have been deposited in a public database such as GEO.

☐ Confirm that you have deposited or provided access to graph files (e.g. BED files) for the called peaks.

Data access links *May remain private before publication.*	https://www.ncbi.nlm.nih.gov/geo/query/acc.cgi?acc=GSE196991
Files in database submission	GSM5906339 H3K9ac_CPT1a_KO-1 GSM5906340 H3K9ac_CPT1a_KO-2 GSM5906341 H3K9ac_CPT1a_KO-3 GSM5906342 H3K9ac_CPT1a_KO+Ac-1 GSM5906343 H3K9ac_CPT1a_KO+Ac-2 GSM5906344 H3K9ac_CPT1a_KO+Ac-3 GSM5906345 H3K9ac_KAT2a_KO_-1 GSM5906346 H3K9ac_KAT2a_KO_-2 GSM5906347 H3K9ac_KAT2a_KO_-3 GSM5906348 H3K9ac_SCR-1 GSM5906349 H3K9ac_SCR-2 GSM5906350 H3K9ac_SCR-3 GSM5906351 Input_CPT1a_KO-1 GSM5906352 Input_CPT1a_KO-2 GSM5906353 Input_CPT1a_KO-3 GSM5906354 Input_CPT1a_KO+Ac-1 GSM5906355 Input_CPT1a_KO+Ac-2 GSM5906356 Input_CPT1a_KO+Ac-3 GSM5906357 Input_KAT2a_KO_-1 GSM5906358 Input_KAT2a_KO_-2 GSM5906359 Input_KAT2a_KO_-3 GSM5906360 Input_SCR-1 GSM5906361 Input_SCR-2 GSM5906362 Input_SCR-3
Genome browser session (e.g. UCSC)	no longer applicaple

Methodology

Replicates	Experimental conditions were analyzed in triplicates
Sequencing depth	Single-end data with a read length of 51 bp
Antibodies	H3K9ac (Cell signaling, 9649S, 1:50 dilution)
Peak calling parameters	genome="../resources/Mus_musculus/UCSC/mm10/Sequence/Bowtie2Index/genome" bowtie2 -x "$genome" -U 01_clean/"$sample".fastq.gz -S 02_mapped/"$sample".sam samtools view -bhS -o 02_mapped/"$sample".bam 02_mapped/"$sample".sam samtools flagstat 02_mapped/"$sample".bam > 02_mapped/"$sample".out samtools sort -o 02_mapped/"$sample".sorted.bam 02_mapped/"$sample".bam samtools index 02_mapped/"$sample".sorted.bam macs2 callpeak -g mm --nomodel -n 03_peaks/"$sample" -q 0.01 -t 02_mapped/"$sample".sorted.bam -c "$input".sorted.bam &>> 03_peaks/"$sample".log
Data quality	The raw sequencing reads were cleaned with the fastq-mcf software, and a quality control was performed with FastQC. We kept the peaks with an FDR of 1% and an above 5-fold enrichment. NHumber of peaks will be collected in a table and provided as a supplementary information.
Software	To further analyse the ChIP-seq data we made use of the deepTools software package. The peaks signals were normalized with a spike-in signal (dm6) of with normalization factors were calculated. The deepTools command bamCoverage was then used to normalize the signals. Furthermore, the commands computeMatrix and plotHeatmap were utilized to visualize this ChIP-seq data. To get more info about the peaks, they were annotated using the HOMER software package (annotatePeaks.pl). To compare the ChIP-seq signals with one another, we composed a list of all regions in the genome with a peak in one of the signals. This list was further processed with the bedtools software, and converted to a gff-file. Subsequently, the number of reads per region was counted with HTSeq-count. The data was then further processed with the DESeq2 package, similar to differential gene expression analysis.

Flow Cytometry

Plots

Confirm that:

☒ The axis labels state the marker and fluorochrome used (e.g. CD4-FITC).

☒ The axis scales are clearly visible. Include numbers along axes only for bottom left plot of group (a 'group' is an analysis of identical markers).

☒ All plots are contour plots with outliers or pseudocolor plots.

☒ A numerical value for number of cells or percentage (with statistics) is provided.

Methodology

Sample preparation	Lungs were extracted and the tissue was washed in blood bank saline, dry and minced for >2min using blades. Tissues were incubated with Liberase (Roche) (0.3 mg/mL) and DNAse1 (1 µg/mL) during 45 min at 37°C with occasional vortex. The reaction was quenched with 3% FBS:PBS + 2mM EDTA and filtered through a 70µm cell strainer. Cell pellet was washed, incubated with Red Blood Lysis buffer (Merck) and transferred through a 40 µm cell strainer. Single-cells suspension was counted and 30x106 cells/mL were stained for flow cytometry analysis.
Instrument	BD FACSCanto II
Software	BD FACSDiva and FlowJo
Cell population abundance	All cells (>90%). All cells/Single Cells (>99%). All cells/Single Cells /Alive (>95%). All cells/Single Cells/Alive/CD45- (40-60%).
Gating strategy	For CD90.1 labeled cancer cells from single cell lung suspensions, gating on positive for viability marker for live cells, CD45 negative, Podoplanin and CD90.1 positive. For alveolar type II cells from single cell lung suspensions, gating on positive for viability marker for live cells, CD45 negative EpCAM positive, CD31 negative, MCH-II and CD49f positive (according to PMID: 32527928)

☒ Tick this box to confirm that a figure exemplifying the gating strategy is provided in the Supplementary Information.